

Quantum-coherent transport in low-dimensional mesoscopic structures and thin films

Yuantao Xie

Dissertation submitted to the Faculty of the
Virginia Polytechnic Institute and State University
in partial fulfillment of the requirements for the degree of

Doctor of Philosophy
in
Physics

Jean J. Heremans, Chair
Camillo Mariani
Victoria G. Soghomonian
Chenggang Tao

December 15, 2017
Blacksburg, Virginia

Keywords: Mesoscopic, quantum interference, environmental coupling decoherence,
Nyquist scattering
Copyright 2017, Yuantao Xie

Quantum-coherent transport in low-dimensional mesoscopic structures and thin films

Yuantao Xie

ABSTRACT (academic)

This thesis experimentally studies quantum interference phenomena and quantum coherence in mesoscopic systems, and quantum transport as well as magnetotransport in various materials system. One overarching aim is exploring the different mechanisms that give rise to quantum phase decoherence in lithographically patterned mesoscopic structures, of importance in the field of quantum technologies and spintronics. Various mesoscopic structures, namely quantum stadia, quantum wires, and side-gated rings, were fabricated to function as quantum interference devices and platforms to study quantum coherence on two-dimensional electron systems in InGaAs/InAlAs heterostructures. The mesoscopic structures were fabricated by photolithography and electron-beam lithography. The dependence of quantum coherence on geometry or temperature is investigated for each of the quantum interference devices.

In the case of quantum stadia, phase coherence lengths were extracted by universal conductance fluctuations, and the extracted phase coherence lengths show a dependence on both temperature and geometry. Phase coherence lengths decreased with increasing temperature, as expected. Moreover, phase coherence lengths also varied with the width-to-length ratio and length of the side wires connected to the stadia, where competition between Nyquist decoherence and environmental coupling decoherence mechanisms coexists. For the quantum wires studied, the phase coherence lengths were extracted from antilocalization signals. Antilocalization measurements provide a sensitive mean of probing the quantum mechanical correction to electronic transport. The phase coherence lengths increased as the wire length increased, due to reduction of the environmental coupling that induces decoherence at the ends of a wire; longer wires tend to have longer phase coherence lengths. In related work, the thesis shows that the spin coherence length, as limited by spin-orbit interaction, increases as the wire width decreases. Decoherence in side-gated rings was measured from the amplitudes of the quantum-mechanical Aharonov-Bohm oscillations. The side gates allow for an in-plane controllable electric field. Asymmetrically biased side-gate voltages allow for the breaking of the two-dimensional parity symmetry of the ring device, effectively resulting in reduced amplitude of the Aharonov-Bohm oscillations. The mechanism that contributes to decoherence in the ring appears to be related to the breaking of the spatial symmetry.

Measurements of antilocalization and weak-localization as well as magnetotransport were used to probe interesting or unique quantum mechanical phenomena in the following two, quite different, materials system: bismuth iridate thin films, and Ge/AlAs heterostructures on GaAs or Si substrates. Both materials are of interest for future quantum technologies and devices. Measurements in bismuth iridate thin films reveal interesting transport

characteristics such as logarithmic temperature dependence of the resistivity, multiple charge carriers, and antilocalization due to spin-orbit interaction in the system. Weak localization measurements in the Ge/AlAs heterostructure on GaAs or Si substrates show that single carrier transport is essentially located in the Ge layer only. Further, the weak localization results indicate the near-absence of spin-orbit interaction for carriers in the electronically active Ge layer, suggesting the potential use of this materials system as a promising candidate for future electronic device applications.

In short, quantum transport and interference measurements probe the quantum-mechanical behavior of materials system for future quantum, spin and electronic technologies. Mesoscopic patterned geometries in InGaAs/InAlAs heterostructures offer a wide range of interesting and unique platforms to study quantum-mechanical phenomena, specifically quantum decoherence, in the solid state. The decoherence phenomena observed and the investigations to the underlying mechanisms studied and modeled in this thesis may be transferred to similar materials system, enriching the knowledge in the field of quantum technologies. Magnetotransport and quantum transport were also applied to Ge/AlAs heterostructures and bismuth iridate thin films, to study the properties of their carrier systems.

ABSTRACT (public)

The work present experimental results on electron quantum coherence and quantum interference phenomena in solid-state systems of small sizes, and on electronic charge transport under magnetic fields in various solid-state materials. More particularly, structures such as quantum stadia, quantum wires, and quantum rings were fabricated on InGaAs/InAlAs semiconductor heterostructures by photolithography and electron-beam lithography, and were characterized by electronic transport at low temperatures to investigate quantum phenomena. Also, electronic transport over variable temperatures and under high magnetic fields was used to characterize the electronic properties of bismuth iridate thin films and Ge/AlAs semiconductor heterostructures. In quantum stadia and in quantum wires, it was found that the electrons quantum coherence lengths decrease with increasing temperature, due to an increase in electron-electron scattering of the Nyquist type as temperature increases. In quantum stadia, the experiments show that quantum coherence lengths vary with the width-to-length ratio and with the lengths of side wires connected to the stadia, explained by a competition between decoherence due to the above-mentioned electron-electron scattering and decoherence due to coupling of the stadia to the external classical environment. In quantum wires, the quantum coherence length was observed to increase as the wire length increases, due to decreased decoherence from coupling of the wires to the external classical environment for longer wires. The dependence of quantum coherence on quantum system geometry described for quantum stadia and wires has a fundamental importance for future quantum device designs. In quantum rings, quantum coherence was investigated by the amplitude of Aharonov-Bohm oscillations. Asymmetric electric fields were applied to break the spatial symmetry of the ring, resulting in reduced amplitude of Aharonov-Bohm oscillations. The result is explained by an effectively reduced quantum coherence due to breaking of the spatial symmetry. Bismuth iridate thin films revealed interesting electronic transport properties, including a logarithmic temperature dependence of the resistivity, multiple charge carriers, and antilocalization due to spin-orbit interaction in the system. Ge/AlAs heterostructures showed single-carrier electronic transport, and weak-localization signals indicating the near-absence of spin-orbit interaction, and a carrier presence restricted to the Ge layer. The promising properties of these two solid-state materials imply potential applications in future electronic and quantum devices.

Dedication

To the flourishing world.

Acknowledgments

The work in this thesis was performed over the past five years. In this period of time, I received a lot of help from various individuals in Department of Physics at Virginia Tech. Firstly, I wish to thank the Department of Physics at Virginia Tech, as it gave me a chance to pursue a PhD degree. Then thanks to Dr. Heremans who is my PhD advisor. Dr. Heremans is a great mentor, he taught me very patiently in the past five years. During my PhD life, I encountered many difficulties, it is Dr. Heremans who helped me to push through all of these difficulties. I still remember that he taught me how to use the scanning electron microscope over and over again until I can do it all by myself. Dr. Soghomonian is really kind. She has helped me from the time I joined this group in 2013. Any time I have needed some favor from her, she has helped me immediately. For example, when I talked to her about graduating and scheduling my final defense, she helped me make a workable plan. This kind of favor is priceless. Finally, I wish to thank all of my group members, William Rieger, Zijian Jiang, Adbhut Gupta, Clément Le Priol, I had a really good time working and learning with you.

Attributions

Chapter 3: Geometrical dependence of quantum decoherence in circular arenas with side-wires. In this chapter, lithography and measurements were undertaken by Clément Le Priol and me; all other aspects of the work was performed by me. This paper was previously published as: Yuantao Xie, C. Le Priol and J. J. Heremans, “Geometrical dependence of quantum decoherence in circular arenas with side-wires”, *Journal of Physics: Condensed Matter* **28**, 495003 (2016). Reproduced with permission.

Chapter 4: Effect of wire length on mesoscopic quantum coherence in InGaAs wires. In this chapter, lithography were undertaken by Clément Le Priol and me; all other aspects of the work was performed by me. To be submitted to *Nano Letters* or *Physical Review B*.

Chapter 5: Effect of two-dimensional parity symmetry breaking in Aharonov-Bohm interference phenomena. In this chapter, the InGaAs heterostructure was grown by M. B. Santos; all other aspects of the work was performed by me. This paper was previously published as: Yuantao Xie, J. J. Heremans and M. B. Santos, “Effect of two dimensional parity symmetry breaking in Aharonov-Bohm interference phenomena”, *Integrated Ferroelectrics* **174**, 8 (2016). Reproduced with permission.

Chapter 6: Mapping electromagnetic dualities via quantum decoherence measurements in 2D materials. In this chapter, lithography of quantum stadia and quantum wires was performed by Clément Le Priol and me, while the data analysis related to quantum stadia and quantum wire was performed by me. This paper was previously published as: J. J. Heremans, Yuantao Xie, S. L. Ren, C. Le Priol and M. B. Santos, “Mapping electromagnetic dualities via quantum decoherence measurements in 2D materials”, *Proceedings of SPIE* **9932**, 993207-1 (2016). Reproduced with permission.

Chapter 7: Epitaxial thin films of pyrochlore iridate $\text{Bi}_{2+x}\text{Ir}_{2-y}\text{O}_{7-\delta}$: structure, defects and transport properties. In this paper, the section: Transport measurements and discussion, was completed all on my own. This paper was previously published as: W. C. Yang, Yuantao Xie, W. K. Zhu, K. Park, A. P. Chen, Y. Losovyj, Z. Li, H. M. Liu, M. Starr, J. A.

Acosta, C. G. Tao, N. Li, Q. X. Jia, J. J. Heremans and S. X. Zhang, “Epitaxial thin films of pyrochlore iridate $\text{Bi}_{2+x}\text{Ir}_{2-y}\text{O}_{7-\delta}$: structure, defects and transport properties”, *Scientific Reports* **7**, 7740 (2017). Reproduced with permission.

Chapter 8: Magnetotransport properties of epitaxial Ge/AlAs heterostructures integrated on GaAs and Silicon. In this paper, the section: Magnetotransport measurement of epitaxial Ge on Si using AlAs/GaAs buffer, was completed all on my own. This paper was previously published as: M. K. Hudait, M. Clavel, P. S. Goley, Yuantao Xie and J. J. Heremans, “Magnetotransport properties of epitaxial Ge/AlAs heterostructures integrated on GaAs and silicon”, *ACS Applied Materials & Interfaces* **7**, 22315 (2015). Reproduced with permission.

Contents

1	Introduction	1
1.1	Universal conductance fluctuations	5
1.2	Weak localization and weak antilocalization	6
1.3	Aharonov-Bohm effect and Altshuler-Aronov-Spivak effect	6
	Bibliography	8
2	Sample fabrication and low temperature magnetotransport	12
2.1	Photolithography and electron-beam lithography	15
2.2	Low temperature magnetotransport	18
	Bibliography	19
3	Geometrical dependence of quantum decoherence in circular arenas with side-wires	21
4	Effect of wire length on mesoscopic quantum coherence in InGaAs wires	28
5	Effect of two-dimensional parity symmetry breaking in Aharonov-Bohm interference phenomena	36
6	Mapping electromagnetic dualities via quantum decoherence measurements in 2D materials	44
7	Epitaxial thin films of pyrochlore iridate $\text{Bi}_{2+x}\text{Ir}_{2-y}\text{O}_{7-\delta}$: structure, defects and transport properties	56

8	Magnetotransport properties of epitaxial Ge/AlAs heterostructures integrated on GaAs and silicon	68
9	Conclusions	77

Chapter 1

Introduction

Length scales engender new and specific phenomena, and in this thesis, we are interested in studying electron decoherence and its potential influence on future quantum technologies via quantum transport in fabricated mesoscale geometries and in thin films. In mesoscale or mesoscopic physics, length scale varies up to several micrometers depending on the phase coherence length of the carriers of interest, here electrons. The smaller length scales of mesoscopic objects and geometries impart them with different characteristics from macroscopic objects, which are governed by the laws of classical mechanics and electromagnetics. The behavior of mesoscopic objects is dominated by quantum effects, quantum confinement and quantum interference. To probe electron decoherence mechanisms, we fabricate mesoscale geometries on specially grown materials systems, which we describe below.

Crystal growth technologies, such as molecular beam epitaxy (MBE) [1], atomic layer deposition (ALD) [2], metal-organic chemical vapor deposition (MOCVD) [3], etc, make it possible to grow semiconductor heterostructures with atomic precision. Heterostructures may contain many chemically diverse layers with various thickness, all governed by the controlled growth processes. The InGaAs/InAlAs heterostructures used all host an electrically conducting two-dimensional electron system, or 2DES [4], in InGaAs layer, with vertical thickness about 10 nm, and sandwiched between two insulating layers. The 2DES is thus formed in a quantum well (QW) of width about 10 nm. The properties of the layers are a function of specific chemical composition, and vertical thickness which provides confinement in 1 dimension. In Chapter 2 we discuss quantum confinement in heterostructures and the emergence of 2DES layers.

Mesoscale geometries are fabricated on the heterostructures using lithographic techniques, photolithography and electron-beam lithography, where we obtain structures of lower dimensions such as quantum wires, quantum dots, quantum rings, quantum stadia, etc. The size of the structure is determined by the phase coherence length of the electron in the system; namely, the size should be smaller than or equal to the phase coherence length such that transport is dominated by the geometry and not by materials defects. Defects, even in sin-

gle crystalline materials, occur due to e.g. impurities, interstitials, substitutions, vacancies, etc [5]. In a solid, electron waves are scattered by defects, and impact electronic transport. Additionally, quantum transport is modified by the presence of defects, and as these modifications are quantifiable, we can experimentally probe them. Quantum interference measurements thus probe the quantum interference phenomena such as universal conductance fluctuations (UCFs) [6, 7], weak localization (WL) [8, 9] and weak antilocalization (WAL) [10–12], the Aharonov-Bohm (AB) [13–16] effect, and the Altshuler-Aronov-Spivak (AAS) [17, 18] effect. In this thesis, we study quantum transport properties in mesoscopic structures by these quantum interference phenomena. We introduce quantum interference and how we use it as a probe.

Quantum mechanically, an electron wavefunction can be expressed as $A \exp(i\varphi)$, with amplitude A , and phase φ which is dependent on time and space. When two electron waves encounter each other and interfere with each other, the probability of finding an electron at the interference position is expressed by [15]: $|A_1 \exp(i\varphi_1) + A_2 \exp(i\varphi_2)|^2 = A_1^2 + A_2^2 + 2A_1A_2 \cos(\varphi_1 - \varphi_2)$. The first two terms are the classical probabilities, whereas the last term is the probability due to quantum interference. The interference can be constructive or destructive based on the sign of the last term; positive indicates constructive whereas negative indicates destructive interference, respectively. In a solid, electron waves may scatter from defects in the material, and the phase of the electron wavefunction is randomized due to the inelastic scattering events. This is observed from the temperature dependence of the measurement, where the phase coherence decreases as temperature goes above 1 K. Interference due to geometry is manifested by the various quantum interference phenomena mentioned above. The space and time scale over which electron waves maintain their phase are the so called phase coherence length L_ϕ and phase coherence time τ_ϕ , respectively. Within this space scale and time scale, electron waves and interference effects are coherent. L_ϕ and τ_ϕ are fundamental quantities in mesoscopic systems, and have been investigated in metal and semiconductor mesoscopic structures with different effective dimensionalities extensively [19–22]. In mesoscopic structures, the relative dimensionalities are defined by the relationship between the geometric dimension(s) and L_ϕ . For example, in a one dimensional wire, we have $L_x \gg L_\phi \gg L_y, L_z$, where L_x is the transport direction, the direction along the length of the wire [19].

For interference, coherent transport is required. Coherent transport is limited by length scale L_ϕ , which is related to scattering mechanisms, such as scattering from defects [23], geometry [9, 24], electron-electron scattering [25, 26], electron-phonon scattering [26], etc. Coulombic scattering from ionized impurities and scattering from device boundaries are typically elastic (energy-conserving) events and do not change the electron phase. Such scattering does not contribute to phase decoherence. Inelastic scattering and so-called quasi-elastic scattering on the other hand contribute to quantum phase decoherence. In inelastic scattering the electron exchanges a substantial fraction of its energy with an elementary excitation (typically another electron or a phonon, but not restricted solely to those), which randomizes the electron phase. Quasi-elastic scattering is accompanied by a small energy exchange and

is typified by the specific mechanism of Nyquist electron-electron scattering (about which more below). The measurements in this thesis were mostly performed at low temperature, T , $T < 1$ K, where inelastic scattering mechanisms are frozen out and thus rare. That leaves the low-energy exchange quasi-elastic Nyquist electron-electron scattering as the dominant phase-breaking mechanism, as experimentally borne out by our measurements. After a phase-breaking scattering process, the electron propagates phase-coherently through the material, maintaining its new phase that is independent from its initial phase [27]. Relative decoherence between individual electrons phases stems from their relative phase differences $\varphi_1 - \varphi_2$, which are random and statistical. Thus summation of these independent interference terms leads to a reduction in the relative amplitude of coherent quantum interference measured. The extent of the influence of the incoherent transport is related to the physical size of the sample, and the phase coherence length L_ϕ . Systems with large size can be decomposed into small subsystems, with length scale of L_ϕ ; the number of subsystems is about $N = (L/L_\phi)^d$ [28]. These subsystems are statistically independent, and the sum of independent quantum interferences over independent subsystems will average out any interference effect, the so called self-averaging process. Thus, due to self-averaging, quantum interference is small in large (macroscopic) systems in most cases, while quantum interference manifests itself in mesoscopic systems, of length scales comparable with phase coherence length L_ϕ . As mentioned, phase coherence length is limited by different decoherence mechanisms, electron-phonon scattering [29], electron-electron scattering with large energy transferring [26], electron-electron scattering with smaller-energy transferring (quasi-elastic Nyquist mechanism) [25, 30, 31], or scattering magnetic impurities [14, 32, 33]. These decoherence mechanisms are defined by specific length scales, which may be expressed by specific decoherence time scales or rates. For example, the phase decoherence time, τ_ϕ is related to L_ϕ by $L_\phi = \sqrt{D\tau_\phi}$ [31].

In a given experiment, several decoherence mechanisms may coexist, and where the total decoherence rate is equal to the sum of different decoherence [26, 30, 31]:

$$\frac{1}{\tau_\phi} = \frac{1}{\tau_{\phi 0}} + \frac{1}{\tau_{e-ph}} + \frac{1}{\tau_{e-e}} + \frac{1}{\tau_N} + \dots \quad (1.1)$$

The first term $\tau_{\phi 0}$ is the external decoherence rate due to mechanisms, such as electromagnetic fluctuations due to the experimental environment. The terms τ_{e-ph} , τ_{e-e} and τ_N denote decoherence rate due to electron-phonon scattering, electron-electron scattering with large energy transfer, and Nyquist scattering, respectively. Phonons are collective vibrations of crystal lattice, the energy of which is dependent on the number, energy and types of phonons. A crystal lattice consists of an array of ions, and the electromagnetic field in this lattice varies with lattice vibrations. Electrons moving in the lattice interact with lattice ions and absorb or emit phonons [29], and this energy exchange process is defined as electron-phonon scattering. Electron-phonon scattering is inelastic scattering, and thus reduces the electron wave packet quasiparticle lifetime τ_i by energy relaxation. In 3-dimensional or bulk weakly-disordered conductors, electron-phonon scattering is the dominant inelastic dephasing process at high temperature. Phase coherence time τ_ϕ is limited by inelastic quasiparticle lifetime τ_i , result-

ing in a decoherence rate of $\tau_\phi^{-1} \sim \tau_i^{-1} \sim \tau_{e-ph}^{-1} \propto T^{-p}$, where typically $p \approx 2 - 4$ depending on system specifics and dimensionality [26]. The coincidence of $\tau_\phi^{-1} \sim \tau_i^{-1}$ here is not necessary, as τ_ϕ is defined as the change in phase, $\Delta\varphi$, given by $\Delta\varphi \sim \Delta\epsilon\tau_\phi \sim 1$, while τ_i is defined as the time scale over which the change in the energy of the electron, ϵ , is constrained by $\Delta\epsilon \sim \epsilon$ [26, 34].

At low T , the number of phonons is small, and the electron-phonon interaction is suppressed. In low dimensional semiconductor systems such as quantum wires and quantum dots, the dominant source of dephasing is found to be Nyquist scattering [30]. Whereas at high temperatures, inelastic large-energy-transfer scattering dominates. At low temperatures, Nyquist scattering has little effect on τ_i but limits τ_ϕ due to small energy transfer during scattering events. In this case $\tau_i \gg \tau_\phi$ Nyquist scattering is due to the interaction of an electron with the fluctuating electromagnetic fields within the sample generated by all other electrons [26]. This random, time and space thermal electromagnetic field fluctuation is called Nyquist noise. Due to the random nature of the Nyquist noise, electrons lose their coherence. In low dimensions, potential fluctuations are affected by sample geometries, and thus Nyquist decoherence rate is also dependent on sample geometries. In the case of 2DES, Nyquist decoherence rate follows $\tau_N^{-1} \propto T$. For 1 dimensional wires with length L , in the diffusive regime where $L \gg L_\phi \gg W$, $\tau_N^{-1} \propto T^{2/3}$, the Nyquist length is defined by $L_N = \sqrt{D\tau_N}$, where D is the diffusion constant. To correlate the Nyquist length to the width, W , of the wires, we use the following expression [25, 35, 36]:

$$L_N = \sqrt{2} \left(\frac{m^* W D^2}{\pi k_B T} \right)^{1/3} \quad (1.2)$$

where k_B is the Boltzmann constant, and m^* is effective mass of electron. As the wire becomes narrower, magnetic flux cancellation [9] needs to be taken into account, and as a result W is included in L_N , with $L_N \sim W^{1/3}$. In the diffusive regime, $L \gg L_\phi$, and the wire length has no effect on L_N , and L_N only relates to the wire width W . In the case of short wires, L_ϕ is comparable with the wire length, and the diffusive condition $L \gg L_\phi$ is not satisfied. In this situation, called the ergodic regime, we observe coherent electron transport over the whole wire length. In the ergodic regime, a new time scale is introduced, the Thouless time [37] $\tau_T = \frac{L^2}{D} < \tau_\phi$, and the Nyquist length L_N expression is modified to [35, 36, 38] $L_{N-s} = \sqrt{D\tau_{N-s}} = \sqrt{L_N^3/L} = 2^{3/4} D \sqrt{m^* W / \pi k_B T L}$. In the short wire limit, $L_{N-s} \sim (W/L)^{1/2}$, and the wire length affects the Nyquist decoherence length, contrary to what we observe in the case of long wires.

While scattering gives rise to decoherence effects, not all decoherence mechanisms are due to scattering. For example, a mesoscopic sample will interact with its classical environment, leading to environmental coupling decoherence [21, 39–41]. In this situation, the electrons are not just confined to the quantum system, but couple with the environment, where the coupling may be expressed by an escape rate, τ_d^{-1} , and a correlated dwell time τ_d [42]. Decoherence due to environmental coupling is dependent on the sample size and geometry. Other decoherence effects may be introduced by varying the temperature of the system. At finite

temperatures, energy levels are broadened and have widths of $k_B T$. When the energy level width is larger than the Thouless energy $E_T = \hbar D/L^2$, multiple independent conduction channels become available, in all mesoscopic systems. The number of independent conduction channels is given by $k_B T/E_T$. Averaging over all the independent channels lead to a suppression of quantum interference phenomena [13]. In addition to thermal broadening, energy level widths can also be broaden by driving voltages and currents [13]. At low temperatures, inelastic or quasi-elastic scattering mechanisms are suppressed [39], and much longer quantum phase coherence lengths L_ϕ are obtained. At liquid helium temperatures, L_ϕ is on the order of a micrometer, a length scale very easily attained by lithography. Thus experimentally investigating quantum transport is feasible. In the remainder of this chapter, we will discuss the following quantum interference effects: UCFs, WL and WAL, AB oscillations, AAS oscillations, etc. Low and variable temperature measurements described in Chapter 2, allow for investigating quantum transport. Moreover, they allow us to measure carrier densities, mobilities, carrier types, effective masses of carriers, and spin-orbit interaction.

1.1 Universal conductance fluctuations

At low temperatures, magnetoresistance of mesoscopic structures exhibits highly reproducible and aperiodic patterns, known as UCFs [43–45]. The specific patterns of UCFs are dependent on certain impurity configuration that is frozen during a given cooldown cycle [6]. At low temperatures, the configurations of impurities and defects are static, thus making UCFs reproducible during one cooldown cycle. To change the UCF patterns, one needs to heat the sample to higher temperature with larger $k_B T$, and then cool down the sample again. Also UCF patterns are sample dependent as impurity configurations are sample dependent. At $T \rightarrow 0$, the amplitude of UCFs in a single conduction channel is e^2/h . In an actual measurement, the amplitude of UCFs is mitigated by self-averaging, which happens as long as there are independent quantum interferences. Firstly, when the sample size is larger than the phase coherence length L_ϕ , we may consider the mesoscopic structure to be divided into subsystems, with length scale of L_ϕ . Quantum interferences in these subsystems are statistical independent, which implies that UCFs are also independent in the subsystems. Thus the measured UCFs are the sum in all the different subsystems, experience self-averaging and are mitigated. Secondly, all measurements are conducted at finite but low temperatures, and uncorrelated energy regimes are involved as long as $k_B T$ is larger than the Thouless energy $E_T = \hbar D/L^2$. As mentioned earlier, high temperatures will induce multiple conduction channels and leads to self-averaging. Moreover, impurities and defect configuration in a sample have a spatial dependency, which means that UCFs patterns vary in real space, and fabricating many identical structures in series or in parallel also lead to self-averaging of the amplitude of the UCFs as a function of $1/\sqrt{N}$, where N is the number of identical structures [28]. Thus, and according to the explanation above, larger amplitude of UCFs can be achieved by fabricating a smaller single structure and measuring it at lower

temperatures, as discussed in detail in Chapter 3.

1.2 Weak localization and weak antilocalization

In disordered systems, electrons are randomly scattered. In the two extreme cases, highly disordered or exceedingly weakly disordered, we do not observe quantum interference phenomena. This is due to non-itinerant electrons in the first situation and to the exceedingly long coherence lengths in the second situation that yield no interference effects. In the regime of weakly or very weakly disordered systems, the electrons are itinerant and now we can define an exact time reversed path for interacting electrons. The quantum interference phenomena here are described by WL [8, 46, 47] and WAL [48–51]. Electron waves in pair of time-reversal paths are able to interference with each other. As the quantum phase accumulations in time-reversal paths are the same, the phase differences of the quantum interference are zero, and such interferences are able to survive under averaging; zero phase differences imply constructive interference. Thus conductance corrections due to quantum interference are negative. Applying an external magnetic field will induce time-reversal symmetry breaking, the interferences in time-reversal paths will be weakened, and thus the conductance will increase. This phenomenon is known as WL [8, 9, 34]. In systems with spin-orbit interactions, electron spin and momentum are coupled with each other, and the spin of electrons in a pair of time-reversal paths will rotate in opposite directions because their momenta are in opposite directions. Under this condition, interference is destructive at zero magnetic field and the conductance correction is positive. Applying an external magnetic field will again induce time-reversal symmetry breaking, weakening the quantum interference effect, causing a decrease in the conductance, leading to the phenomena of WAL [12, 24, 52, 53]. Since conductance correction of WL and WAL are sensitive to the phase coherence length, they are used to extracted electron phase coherence information in our systems. In Chapter 4, we discuss the experiments and the methods used for extracting phase coherence information for an array of parallel quantum wires fabricated on an InGaAs/InAlAs heterostructure.

1.3 Aharonov-Bohm effect and Altshuler-Aronov-Spivak effect

Above we discussed UCFs, and WL and WAL. Another quantum interference phenomenon that we use is the AB effect [54–57]. In order to observe this effect, a ring interferometer, has to be fabricated. The AB effect is observed in the presence of an external applied magnetic field, where the interference manifests itself in the oscillations in the magnetoresistance over the ring. These oscillations are due to the varying magnetic flux, Φ , through the ring, and are periodic in h/e . The magnetic flux is expressed by $\Phi = \int \mathbf{B} \cdot d\mathbf{s}$. We first consider the case of a single ring interferometer. Electrons entering the ring travel in the two separated left and

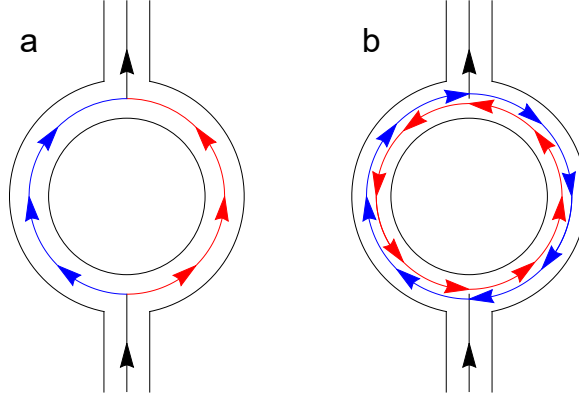


Figure 1.1: Schematic diagram depicting AB and AAS effects. (a) The AB effect where electrons injected from one end of a ring travel in two separated left and right paths before interfering at the other end of the ring. (b) The AAS effect where partial waves travel on time-reversed paths and then interfere. (Figure modified from reference [58]) .

right- paths as showed in Fig. 1.1.a. The partial wave functions taking the separate paths combine at the exit of ring. The interference between these two spatially different electron waves can be expressed as $A \cos(\varphi)$. φ is the phase difference between these two electron partial waves in the separated paths, and is expressed as [18]: $\varphi = e/\hbar \int \mathbf{A} \cdot d\mathbf{l} = e/\hbar \int \mathbf{B} \cdot d\mathbf{s}$. As the left and right paths are not equivalent, typically due to lithographic and materials defects, an extra phase difference φ_0 is introduced, such that $\varphi = e/\hbar \int \mathbf{B} \cdot d\mathbf{s} + \varphi_0$. The extra phase, φ_0 , depends on the path, and thus depends on the local properties of the sample. In our experiments, we additionally use an applied electric field to enhance the breaking of the spatial symmetry of the electron paths in a ring system. The electric field causes a decrease in the amplitude of the AB oscillations.

While AB oscillations are periodic in h/e , oscillations that are periodic in $h/2e$ are denoted as AAS oscillations [59, 60]. Whereas AB oscillations arise from quantum interference of partial waves on spatially separate paths, and are therefore sensitive to spatial symmetry, AAS oscillations arise from quantum interference of partial waves on time-reversed paths as showed in Fig. 1.1.b, and are therefore sensitive to time-reversal symmetry [61]. Thus AAS oscillations, unlike AB oscillations, are not sensitive to an applied transverse electric field. Moreover, the extra phase present in AB oscillations is now either 0 or π , implying that φ_0 does not influence AAS oscillations. In ring systems, the two effects, AB and AAS, coexist, and are often both observed. The relative amplitudes of the AAS and AB oscillations in a given system are structure dependent. In a single ring system where the circumference of the ring is given as L , the amplitude, A , of the AB interference is dependent on the path length exponentially, expressed as $A \propto e^{\frac{-L}{L\phi}}$ [14]. In the case of AAS oscillations, the amplitude is given by $A \propto e^{\frac{-2L}{L\phi}}$, resulting in the smaller AAS oscillation amplitude. Moreover, AAS

oscillations will decay as the external magnetic field in the interferometer arms increases, due to time-reversal symmetry breaking. Concerning AB oscillations in ring array systems, the extra phase, φ_0 , of each ring depends on the variations, however small, of the local sample properties and geometry. The influence of φ_0 on the sum of AB oscillations in different rings tends to weaken the AB oscillation amplitude, but not that of the AAS oscillation amplitude as AAS oscillations are not influenced by φ_0 and are thus always in phase for all the rings in the array. Thus in experiments, we usually use a single ring to measure AB oscillations, and use a ring array to measure AAS oscillations, as AB oscillations are suppressed in ring arrays. Previous work observed AB oscillations in both diffusive and ballistic regimes, while AAS oscillations were only observed in the diffusive regime. Nakamura *et.al* [18, 59, 60, 62] predicted the existence of AAS oscillations in the ballistic regime. To date, in the literature, no experimental work has yet observed AAS oscillations in the ballistic regime. Unpublished results in Prof. Heremans' group in a self-focusing array of ellipses hint at AAS oscillations in the ballistic regime.

Bibliography

- [1] Johnson, R. W., Hultqvist, A., and Bent, S. F. *Mater. Today* **17**, 236 (2014).
- [2] Arthur, J. R. *Surf. Sci.* **500**, 189 (2002).
- [3] Coleman, J. J. *Proc. IEEE* **85**, 1715 (1997).
- [4] Haug, H. and Koch, S. W. *Quantum theory of the optical and electronic properties of semiconductors*. World Scientific Publishing, Bangalore, (2009).
- [5] Seebauer, E. G. and Noh, K. W. *Mater. Sci. Eng. R Rep.* **70**, 151 (2010).
- [6] Yang, P.-Y., Wang, L. Y., Hsu, Y.-W., and Lin, J.-J. *Phys. Rev. B* **85**, 085423 (2012).
- [7] Jalabert, R. A., Baranger, H. U., and Stone, A. D. *Phys. Rev. Lett.* **65**, 2442 (1990).
- [8] Liang, D., Du, J., and Gao, X. P. A. *Phys. Rev. B.* **81**, 153304 (2010).
- [9] Beenakker, C. W. J. and van Houten, H. *Phys. Rev. B* **38**, 3232 (1988).
- [10] Iordanskii, S. V., Lyanda-Geller, Y. B., and Pikus, G. E. *Pis'ma Zh. Eksp. Teor. Fiz* **60**, 199 (1994) (*JETP Lett.* 60, 206(1994)).
- [11] Bergmann, G. *Phys. Rep.* **107**, 1 (1984).
- [12] Licini, J. C., Dolan, G. J., and Bishop, D. J. *Phys. Rev. Lett.* **54**, 1585 (1985).
- [13] Ren, S. L., Heremans, J. J., Gaspe, C. K., Vijayaragunathan, S., Mishima, T. D., and Santos, M. B. *J. Phys.: Condens. Matter* **25**, 435301 (2013).

- [14] Pierre, F. and Birge, N. O. *Phys. Rev. Lett.* **89**, 206804 (2002).
- [15] Aharonov, Y. and Bohm, D. *Phys. Rev.* **115**, 485 (1959).
- [16] Yamauchi, Y., Hashisaka, M., Nakamura, S., Chida, K., Kasai, S., Ono, T., Leturcq, R., Ensslin, K., Driscoll, D. C., Gossard, A. C., and Kobayashi, K. *Phys. Rev. B* **79**, 161306 (2009).
- [17] Altshuler, B. L., Aronov, A. G., and Spivak, B. *Pis'ma Zh. Eksp. Teor. Fiz* **33**, 94 (1981) (*JETP Lett.* **33**, 94(1981)).
- [18] Nakamura, K. and Harayama, T. *Quantum chaos and quantum dots*. Oxford University Press, Oxford, (2005).
- [19] Niimi, Y., Baines, Y., Capron, T., Maily, D., Lo, F.-Y., Wieck, A. D., Meunier, T., Saminadayar, L., and Buerle, C. *Phys. Rev. B* **81**, 245306 (2010).
- [20] Roulleau, P., Choi, T., Riedi, S., Heinzl, T., Shorubalko, I., Ihn, T., and Ensslin, K. *Phys. Rev. B* **81**, 155449 (2010).
- [21] Ferry, D. K., Burke, A. M., Akis, R., Brunner, R., Day, T. E., Meisels, R., Kuchar, F., Bird, J. P., and Bennett, B. R. *Semicond. Sci. Technol.* **26**, 043001 (2011).
- [22] Bird, J. P., Ishibashi, K., Ferry, D. K., Ochiai, Y., Aoyagi, Y., and Sugano, T. *Phys. Rev. B* **51**, 18037 (1995).
- [23] Gerlach, E. *J. Phys. C. : Solid State Phys.* **19**, 4585 (1986).
- [24] Kettemann, S. *Phys. Rev. Lett.* **98**, 176808 (2007).
- [25] Ferrier, M., Angers, L., Rowe, A. C. H., Guéron, S., Bouchiat, H., Texier, C., Montambaux, G., and Maily, D. *Phys. Rev. Lett.* **93**, 246804 (2004).
- [26] Lin, J. J. and Bird, J. P. *J. Phys.: Condens. Matter* **14**, R501 (2002).
- [27] Datta, S. *Electronic transport in mesoscopic systems*. Cambridge University Press, Cambridge, (1995).
- [28] Akkermans, E. and Montambaux, G. *Mesoscopic physics of electrons and photons*. Cambridge University Press, Cambridge, (2007).
- [29] Fujita, S., Ito, K., and Godoy, S. *Quantum theory of conduction matter superconductivity*. Springer, New York, (2009).
- [30] Hackens, B., Delfosse, F., Faniel, S., Gustin, C., Boutry, H., Wallart, X., Bollaert, S., Cappy, A., and Bayot, V. *Phys. Rev. B* **66**, 241305(R) (2002).

- [31] Huibers, A. G., Switkes, M., Marcus, C. M., Campman, K., and Gossard, A. C. *Phys. Rev. Lett.* **81**, 200 (1998).
- [32] Eriksson, E. *Phys. Rev. B* **87**, 235414 (2013).
- [33] Mohanty, P. and Webb, R. A. *Phys. Rev. Lett.* **91**, 066604 (2003).
- [34] Choi, K. K., Tsui, D. C., and Alavi, K. *Phys. Rev. B* **36**, 7751 (1987).
- [35] Ferrier, M., Rowe, A. C. H., Guéron, S., Bouchiat, H., Texier, C., and Montambaux, G. *Phys. Rev. Lett.* **100**, 146802 (2008).
- [36] Texier, C., Delplace, P., and Montambaux, G. *Phys. Rev. B* **80**, 205413 (2009).
- [37] Capron, T., Texier, C., Montambaux, G., Mailly, D., Wieck, A. D., and Saminadayar, L. *Phys. Rev. B* **87**, 041307(R) (2013).
- [38] Texier, C. and Montambaux, G. *Phys. Rev. B* **72**, 115327 (2005).
- [39] Bird, J. P., Micolich, A. P., Linke, H., Ferry, D. K., Akis, R., Ochiai, Y., Aoyagi, Y., and Sugano, T. *J. Phys.: Condens. Matter* **10**, L55 (1988).
- [40] Elhassan, M., Bird, J. P., Akis, R., Ferry, D. K., Ida, T., and Ishibashi, K. *J. Phys.: Condens. Matter* **17**, L351 (2005).
- [41] Bird, J. P., Micolich, A. P., Ferry, D. K., Akis, R., Ochiai, Y., Aoyagi, Y., and Sugano, T. *Solid-State Electron.* **42**, 1281 (1998).
- [42] Hackens, B., Faniel, S., Gustin, C., Wallart, X., Bollaert, S., Cappy, A., and Bayot, V. *Phys. Rev. Lett.* **94**, 146802 (2005).
- [43] Wang, L.-X., Wang, S., Li, J.-G., Li, C.-Z., Yu, D., and Liao, Z.-M. *Phys. Rev. B* **94**, 161402(R) (2016).
- [44] Shamim, S., Mahapatra, S., Scappucci, G., Klesse, W. M., Simmons, M. Y., and Ghosh, A. *Sci. Rep.* **7**, 46670 (2017).
- [45] Xie, Y., Le Priol, C., and Heremans, J. J. *J. Phys.: Condens. Matter* **28**, 495003 (2016).
- [46] Stornaiuolo, D., Gariglio, S., Fte, A., Gabay, M., Li, D., Massarotti, D., and Triscone, J. M. *Phys. Rev. B* **90**, 235426 (2014).
- [47] Yang, Q. I., Dolev, M., Zhang, L., Zhao, J., Fried, A. D., Schemm, E., Liu, M., Palevski, A., Marshall, A. F., Risbud, S. H., and Kapitulnik, A. *Phys. Rev. B* **88** (2013).
- [48] Kallaher, R. L., Heremans, J. J., Goel, N., Chung, S. J., and Santos, M. B. *Phys. Rev. B* **81**, 035335 (2010).

- [49] Kallaher, R. L., Heremans, J. J., Van Roy, W., and Borghs, G. *Phys. Rev. B* **88**, 205407 (2013).
- [50] Heremans, J. J., Kallaher, R. L., Rudolph, M., Santos, M., Van Roy, W., and Borghs, G. *Proc. of SPIE* **9167**, 91670D (2014).
- [51] Heremans, J. J., Xie, Y., Ren, S. L., Le Priol, C., and Santos, M. B. *Proc. of SPIE* **9932**, 993207 (2016).
- [52] Dolan, G. J., Licini, J. C., and Bishop, D. J. *Phys. Rev. Lett.* **56**, 1493 (1986).
- [53] Zduniak, A., Dyakonov, M. I., and Knap, W. *Phys. Rev. B* **56**, 1996 (1997).
- [54] Casse, M., Kvon, Z. D., Gusev, G. M., Olshanetskii, E. B., Litvin, L. V., Plotnikov, A. V., Maude, D. K., and Portal, J. C. *Phys. Rev. B* **62**, 2624 (2000).
- [55] Mankiewich, P. M., Behringer, R. E., Howard, R. E., Chang, A. M., Chang, T. Y., Chelluri, B., Cunningham, J., and Timp, G. *J. Vac. Sci. Technol. B* **6**, 131 (1988).
- [56] Hansen, A. E., Kristensen, A., Pedersen, S., Sørensen, C. B., and Lindelof, P. E. *Phys. Rev. B* **64**, 045327 (2001).
- [57] Xie, Y., Heremans, J. J., and Santos, M. B. *Integr. Ferroelectr.* **174**, 8 (2016).
- [58] Ren, S. L., Heremans, J. J., Vijayaragunathan, S., Mishima, T. D., and Santos, M. B. *J. Phys.: Condens. Matter* **27**, 185801 (2015).
- [59] Kawabata, S. and Nakamura, K. *Phys. Rev. B* **57**, 6282 (1998).
- [60] Kawabata, S. and Nakamura, K. *Chaos.: Solitons & Fractals* **8**, 1085 (1997).
- [61] Russo, S., Oostinga, J. B., Wehenkel, D., Heersche, H. B., Sobhani, S. S., Vandersypen, L. M. K., and Morpurgo, A. F. *Phys. Rev. B* **77**, 085413 (2008).
- [62] Kawabata, S. and Nakamura, K. *J. Phys. Soc. Jpn.* **65**, 3708 (1996).

Chapter 2

Sample fabrication and low temperature magnetotransport

In this thesis, III-V semiconductor InGaAs/InAlAs heterostructures, Ge/AlAs heterostructures on GaAs or Si substrates, as well as bismuth iridate thin film materials system are studied. There are commonalities in sample fabrication and measurement, and are discussed in this chapter. Indium containing heterostructures, e.g. InGaAs/InAlAs, were chosen, over the more commonly available heterostructures, such as GaAs/AlGaAs, because of the characteristics of the QW in the In-containing systems, a schematic diagram for which is depicted on Fig. 2.1. Firstly, the effective electron mass in InGaAs is lighter than that in GaAs at the Γ -point band edge, and thus higher electron mobility is expected in InGaAs QWs. Secondly, in the lowest conduction band of InGaAs, the separation between the lower Γ valley and higher L valley is 0.7 eV. This separation is much larger than that in GaAs [1], indicating that electrons only appear in the Γ valley, and that intervalley scattering, which complicates transport measurements, may be ignored in the InGaAs heterostructures. Lastly, In-containing III-V semiconductors have strong Rashba spin-orbit interaction [2], which is of use for investigating spin-related quantum interference phenomena. Thus, InGaAs/InAlAs heterostructures are preferred, and are used for fabricating the quantum wires and arenas with side wires discussed in Chapters 3 and 4.

The InGaAs/InAlAs heterostructures used here are grown by MBE, a technique used to grow high quality single-crystal thin films [3]. The schematic growth sequences of two heterostructures used in this thesis are shown in Fig. 2.2, where both were grown on semi insulating InP substrates. A thick InAlAs buffer was first grown on the substrate, followed by all the layers of the heterostructure lattice matched to the substrate. The narrow gap semiconductor InGaAs layer was sandwiched between two thick layers of the wide gap semiconductors InAlAs. The conduction channel, which is the QW, is confined in the InGaAs layer (red layers in Fig. 2.2). Si-doping in the InAlAs spacer layers is used to provide electrons to the InGaAs QW [4]. An undoped InAlAs spacer is used to provide separation between the ion-

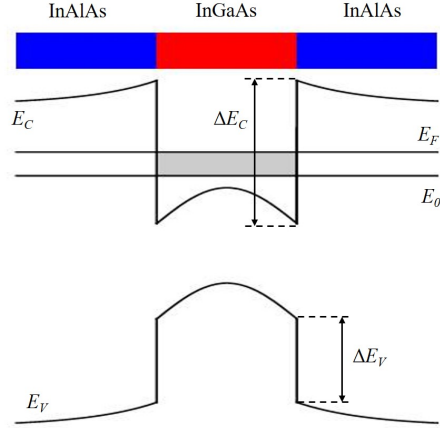


Figure 2.1: Schematic diagram for an InGaAs QW. The InGaAs layer, which hosts the 2DES QW, is sandwiched between InAlAs layers that act as potential walls in the InAlAs/InGaAs/InAlAs heterostructure. The conduction band offset, indicated in the figure as ΔE_C , between InAlAs and InGaAs is large (the valence band offset, ΔE_V , is also indicated). The grey shaded area in the figure indicates filled electron kinetic energy levels in the QW, with E_0 as the ground state, and E_F as the Fermi energy level.

ized Si dopants in the InAlAs layers and the 2DES in the InGaAs QW, to reduce Coulombic scattering between the electrons in the 2DES and the ionized Si dopants.

The two different InGaAs heterostructures are shown in Fig. 2.2. The heterostructure on the right has a bulk Si doped layer, whereas the structure on the left has Si- δ doped layers. Moreover, the structure on the right is bottom doped, causing the band structure to tilt more, enhancing the Rashba spin-orbit interaction. Thus for the experiments that utilized Rashba spin-orbit coupling effects, such as the measurements of the wires and the arenas, we used the bottom doped heterostructures, see Chapters 3 and 4. For the studies of the AB effect, we used the top doped heterostructures, as discussed in Chapters 5. The properties of the QWs in both heterostructures were measured at 0.38 K, and are listed in Table 2.1. Firstly, van der Pauw geometries were measured to obtain sheet resistances R_{\square} . Secondly, Shubnikov-de Haas oscillations and Hall resistances were measured to extract carrier densities n_s . The results from the Shubnikov-de Haas and Hall measurements were consistent with each other. All the other QW parameters listed in Table 2.1 were extracted from the above mentioned measurements, using the Γ -point effective mass value of $0.0353 m_e$ [5] (where m_e is the free electron mass), and low temperature band gap value of 813 meV for InGaAs.

In the next section, we describe the processes we use to fabricate mesoscopic structures on the 2DES described above, as well as for other heterostructures and thin film samples.

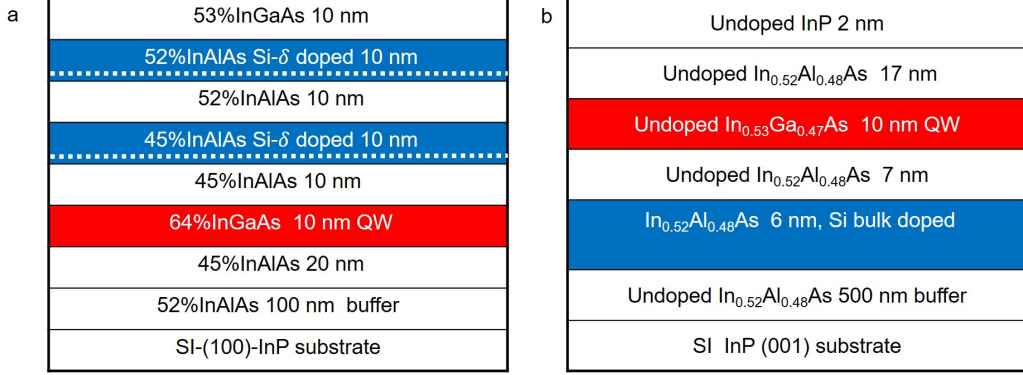


Figure 2.2: The two heterostructures used in our experiments. A layer of the narrow band gap semiconductor InGaAs is sandwiched between two wide gap semiconductors InAlAs layers, with the 2DES confined in the QW InGaAs layer. The growth sequence is different for each heterostructure. (a) Top-doped InGaAs QW growth sequence; 100 nm InAlAs buffer on an InP substrate, 20 nm InAlAs spacer, 10 nm InGaAs QW layer which is the conduction channel, 10 nm InAlAs spacer, 10 nm InAlAs with Si- δ doping at the interface, 10 nm InAlAs spacer, 10 nm InAlAs with Si- δ doping at interface, 10 nm InGaAs. (b) Bottom-doped InGaAs QW sequence; 500 nm InAlAs buffer on an InP substrate, 6 nm InAlAs, which is Si bulk doped, 7 nm undoped InAlAs spacer, 10 nm InGaAs QW layer which is the conduction layer, 17 nm InAlAs layer, 2 nm InP cap to prevent oxidation.

Table 2.1: Transport properties of the InGaAs QWs in the InGaAs/InAlAs heterostructures measured at 0.38 K

		top-doped InGaAs QW	bottom-doped InGaAs QW
Sheet resistance (Ω/\square)	$R_{\square} = n_s e^2 \tau_e / m^*$	54	207
Electron density (10^{16} m^{-2})	$n_s = B / e R_{XY}$	1.48	2.02
Mobility (m^2/Vs)	$\mu = \frac{e \tau_e}{m^*}$	7.80	1.49
Fermi velocity (m/s)	$v_F = \frac{\hbar k_F}{m^*} = \frac{\hbar \sqrt{2\pi n_s}}{m^*}$	703989	788002
Electron mean free path (μm)	$l_e = v_F \tau_e$	3.20	0.77
Fermi wavelength (nm)	$\lambda_F = \sqrt{2\pi / n_s}$	20.6	17.6
Diffusion coefficient (m^2/s)	$D = \frac{1}{2} v_F l_e$	1.11	0.30

2.1 Photolithography and electron-beam lithography

To fabricate mesoscopic structures such as wires or arenas or rings, we etch trenches in the conduction channel within the heterostructure. The depth of the trench should be deeper than the layer just above the conducting InGaAs layer to ensure that there are no conduction electrons under these trenches due to depletion. The trenches act as insulating barriers. Photolithography and electron-beam lithography are used to delineate patterns. In the case of photolithography, photomasks with the desired pattern are used. In the case of electron-beam lithography, the desired pattern is written point by point using the electron beam of a scanning electron microscope (SEM) coupled with lithography capabilities. The overall procedures are similar, and are delineated in Fig. 2.3. Mesoscopic structures are usually small, on the order of 1 μm , and often several lithographic steps at different scales are required to obtain structures that may be contacted for measurements. Usually, we first define a macroscopic Hall bar of size about 1 mm. We then fabricate our smaller mesoscale geometry and contact it to the Hall bar via lithographies. We then contact the macroscale Hall bar for our measurements. Before any lithographic step, the sample or wafer has to be cleaned. Firstly, the wafer is immersed in trichloroethylene (TCE), acetone, and isopropanol (IPA) solvents in sequence. By this cleaning sequence, most organic and environmental contaminants are removed. After cleaning, the sample is glued on a 18×18 mm² glass slide. Next, a layer of positive photoresist, Micro Resist Technology GmbH ma-P 1210, is spin coated on the sample. The sample is spun for 30 seconds at a spinning speed of 3000 rpm. After coating, the sample is placed in a 100 °C oven and baked for 30 minutes, to cure the photoresist. The photomask is then placed on top of the sample, and both are placed in the Karl Suss MJB-3 mask aligner, where the photomask pattern is aligned to the sample optically. After alignment, the photoresist coated sample is exposure to uniform ultraviolet (UV) light for about 12 seconds. After exposure, parts of the photoresist not covered by the pattern are washed away, or developed, by immersing the sample in the Clariant AZ 351 developer. The developing time is dependent on the concentration of developer, and is usually about 1 minute for undiluted developer. At the end of this step, we have transferred the pattern from the photomask to the sample, under a protective photoresist layer. Portions of the sample not covered with photoresist are now etched to a depth of 200 nm by placing the sample in a solution of $\text{H}_3\text{PO}_4:\text{H}_2\text{O}_2:\text{H}_2\text{O}=1:1:38$ volume ratio for 120 seconds. This etching step transfer the pattern on the photomask to the 2DES. The depth of the etch step is governed by the location of the 2DES from the surface of the heterostructure. After etching, the protective photoresist pattern needs to be washed away from the sample. The sample is now placed in Nano Remover PG for about 10 minutes to remove most of the photoresist, and then in boiling Nano Remover PG for 1 hour to remove any residual photoresist. To remove the Nano Remover PG, the sample is placed in IPA for 10 minutes, then washed with deionized water (DIW), and finally dried in a steam of N_2 gas. The sample is now ready for contacting. Before soldering the contacts onto the macroscopic Hall bar pattern, the sample is placed in a 100 °C oven for 10 minutes to remove surface water. The contact material is an alloy of In and Sn, in the ratio of 52:48. The alloy is soldered on the sample with a

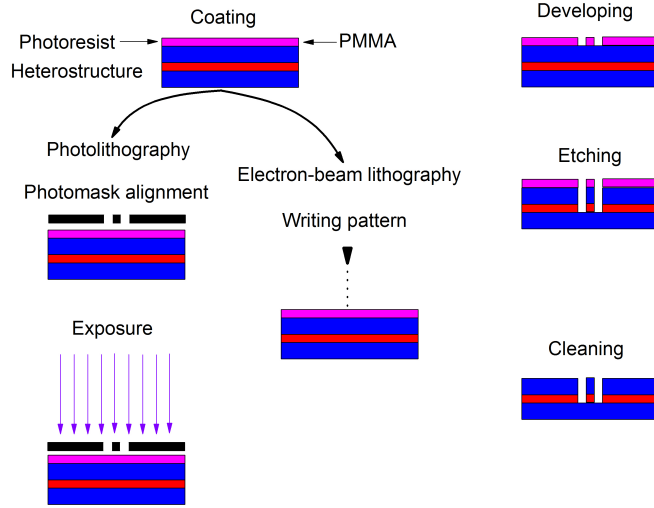


Figure 2.3: Schematic diagram of the of photolithography and electron-beam lithography processes. For photolithography, sample is coated with photoresist, cured, then aligned to pattern on photomask in the mask aligner. Photoresist covered sample is exposed to UV light, and then soaked in developer, acid etch, and photoresist remover to delineate sample. Electron-beam lithography is performed to delineate finer structures than attainable by photolithography. For the electron-beam lithography process, the sample is coated by a polymer sensitive to electron beams, e.g. PMMA. The PMMA is then cured, and the desired pattern written onto the sample by the electron beam of a scanning electron microscope. The sample is then developed in IPA: MIBK=3:1 volume ratio solution, and etched by wet etching or RIE methods, and then soaked in acetone to remove the PMMA.

soldering tip held at 240 °C. After contacting, the sample is annealed at 320 °C in a stream of N_2/H_2 gas for 5 minutes. The stream of N_2/H_2 gas prevents sample oxidation during annealing. The high temperature during the annealing step will melt the In:Sn alloy and create spikes underneath the contacts that pierce through the insulator layers and connect the 2DES with the contacts. Sometimes, contacts are not Ohmic due to contamination in the processes described above. The contamination of the sample surface can induce a depletion layer under the contacts, or cause the contacts not to stick appropriately to the sample surface. In these cases, we obtain insulating, and thus unusable, contacts. It is very important to carefully clean the sample after the photolithography step. After successful contacting, the sample is ready for the next step, which involves delineating the mesoscopic structures by electron-beam lithography.

The electron-beam lithography process is similar to photolithography, and is schematically shown in Fig. 2.3. After photolithography and placing of contacts, the sample is glued on a gold coated glass slide by colloidal graphite, dried at room temperature for 10 minutes, and

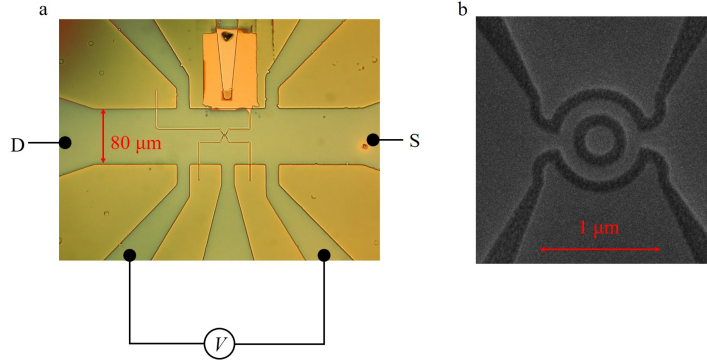


Figure 2.4: Typical geometry for a magnetoresistance measurement. (a) A mesoscopic device (here a side-gated interferometric ring) is fabricated on a Hall bar. The interferometric ring is visible at the approximate center of this Hall bar image. Current is drawn between the ‘S’ and ‘D’ contacts, and the voltage drop over the mesoscopic device is measured using the voltage contacts indicated (connected to voltmeter “V”). (b) Magnified image (SEM micrograph) of the side-gated interferometric ring, fabricated on the Hall bar shown in panel a.

baked at 160 °C for 30 minutes. After baking, the sample is spin coated with polymethyl methacrylate (PMMA) layer. The sample is spun for 40 seconds with a spinning speed 7700 rpm. The sample is then baked at 160 °C for 4 to 7 hours; usually we bake our samples for 5.5 hours. After baking, the sample is marked to allow us to align our initial photolithography pattern in the SEM. An electron-beam pattern writing capability software package, Nability Nano-Pattern Generating Software, is used in conjunction with the Leo EVO 40 SEM. The desired pattern is first drawn in the Nability software. The pattern is then drawn onto the PMMA layer by controlling the finely focused electron beam of the SEM. The use of a gold coated slide and colloidal graphite to affix the sample is to minimize charging by the electron beam. The polymer chains of the PMMA exposed to the electron beam undergo degradation, and are more easily dissolved, or developed, in a solution of IPA and MIBK (methyl isobutyl ketone), in the volume ratio of 3:1, yielding the desired pattern on the sample surface. Throughout the lithographic processes, we often need to etch surfaces for a variety of reasons. There are several different etching processes, wet or dry, that we use depending on the sample and desired end results. Wet etching, depending on the chemical used and specific sample surface, may be isotropic or anisotropic, each with its own drawbacks. Moreover, it is hard to control a wet etch process, and this method is not often used to generate fine structures. On the other hand, dry etch techniques such as reactive ion etching (RIE) etch in the direction perpendicular to the sample surface, with higher etching accuracy [6]. Thus RIE is often used as an etch step in the fabrication of fine structures. As with any process, RIE does have a drawback that often the PMMA layer is burned in the etch process and is then very hard to remove. To circumvent the issue of any residual PMMA layer on our samples, we contact the sample before the electron-beam lithography

step, as described above. After all the fabrication steps, the sample contacts are wired to the pins of a standard 14 dual-inline package (DIP) form and mounted on a probe that is then inserted into a low temperature and variable magnetic field system. The geometry of a typical example sample for a magnetoresistance measurement is depicted on Fig. 2.4. A current is drawn between the ‘S’ and ‘D’ contacts, and the resulting voltage drop over the mesoscopic device is measured using the voltage contacts indicated. Current contacts ‘S’ and ‘D’ and the voltage contacts are Ohmic contacts fabricated on the Hall mesa structure, and these contacts are located at macroscopic distances (tens of μm) away from the central device to be measured (in the example of Fig. 2.4.a the central device is an interferometric ring, shown magnified in Fig. 2.4.b). Two different magnetotransport systems can be used to measure mesoscopic devices, and they are described in the next section.

2.2 Low temperature magnetotransport

Quantum interferences phenomena in mesoscopic systems usually disappear at temperatures above 10 K due to thermal broadening. Thus, to investigate the quantum phenomena in our samples, we need low temperatures ranging from 0.38 K to 10 K. Two magnetotransport systems are used. The first consists of a superconducting magnet capable of reaching 9 T and temperatures as low as 0.38 K using a ^3He insert, while the second set-up uses an electromagnet capable of reaching 1.4 T and temperatures as low as 4.0 K using a closed cycle system. The commercial Janis 9TM-SVM-17V superconducting magnet system reaches 1.2 K with liquid ^4He . A home-built ^3He insert is used to lower the temperature to 0.38 K. The schematic of the set-up is depicted in Fig. 2.5. The sample temperature is varied either by a pair of pumps (indicated in Fig. 2.5), or via a heater where we have more control of the sample’s temperature as it is monitored by a Lake Shore 370 AC resistance bridge. A bipolar superconducting magnet power supply, Cryomagnetics CS-4, is used to drive the superconducting magnet, with minimum sweeping step of about 1 Gauss. During a measurement, the circuit with the mesoscopic device with resistance R , and a variable resistor R_v in series, is driven by an alternating voltage source generated by the SR124 analog lock-in amplifier, which is also used to measure the voltage drop over the mesoscopic device. The measurement -- instruments, temperature, magnetic sweep, etc. -- is controlled via a LabVIEW program specifically written for the experiment in mind. The quantum correction value to a sample’s classical electrical conductance is very small, and thus very sensitive instrumentation is required to extract these signals, even at very low temperatures. In our experiments, we extract the conductance via the voltage drop resulting from a constant current passing through the sample. The voltage drop is measured by lock-in amplifiers accurate to a nanovolt. The lock-in amplifiers are used both as voltmeters and as drive sources. A sine wavefunction is generated by the lock-in amplifier driving the sample through a variable resistor. The resistance of the variable resistor, R_v is much larger than the sample’s resistance, R . During a measurement, choices are made such that R_v is much larger than R , ensuring that the current in the sample is kept constant. Magnetotransport data includes

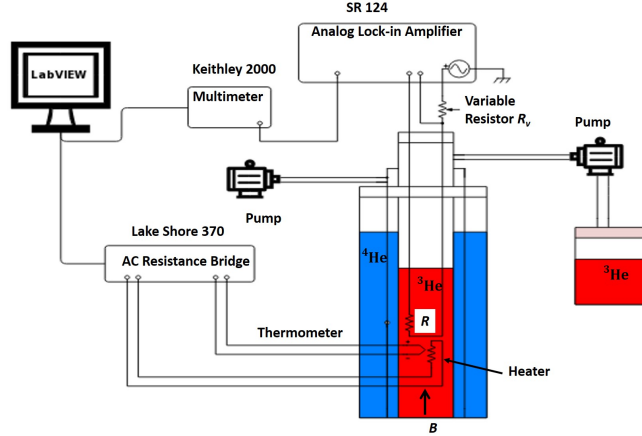


Figure 2.5: Schematic diagram of the ^3He insert low temperature measurement set-up. A sample with resistance R is placed into the cryostat, where the sample can be cooled down to as low as 0.38 K. The temperature can be controlled by the two pumps, or can be tuned by the heater which is controlled by an AC resistance bridge. The signal is monitored by an analog lock-in amplifier, model SR 124, and the measured signal is scaled and outputted to a Keithley multimeter. The computer reads the data from the multimeter, and the whole measurement is controlled by a LabVIEW program.

temperature T , magnetic field B , voltage over samples R , and gate voltage V_g .

Similar data is obtained in the closed-cycle Cryomech CP950COPSW-4 system, where the lowest temperature obtained is now only 4.0 K. The refrigerator makes use of a two-stage Gifford-McMahon cycle [7], with high purified helium gas as working fluid. For samples and materials system that do not require either very high magnetic fields or very low temperatures, e.g. the Ge/AlAs heterostructures on GaAs or Si substrates, the Cryomech system was used for magnetotransport measurements. For more delicate measurements such as those regarding AB effect, the ^3He set-up was used. Both set-ups use the same instrumentation, and in both cases we are measuring the same physical parameters as mentioned above.

Bibliography

- [1] Masselink, W. T. *Appl. Phys. Lett.* **67**, 801 (1995).
- [2] Nitta, J., Akazaki, T., Takayanagi, H., and Enoki, T. *Phys. Rev. Lett.* **78**, 1335 (1997).
- [3] Johnson, R. W., Hultqvist, A., and Bent, S. F. *Mater. Today* **17**, 236 (2014).

- [4] Matsuoka, T., Kobayashi, E., Taniguchi, K., Hamaguchi, C., and Sasa, S. *Jpn. J. Appl. Phys.* **29**, 2017 (1990).
- [5] Ren, S. L., Heremans, J. J., Vijayaragunathan, S., Mishima, T. D., and Santos, M. B. *J. Phys.: Condens. Matter* **27**, 185801 (2015).
- [6] Geng, H. *Semiconductor manufacturing handbook*. McGraw-Hill, New York, (2005).
- [7] Thirumaleshwar, M. and Pandey, R. M. *Cryogenics* **30**, 100 (1989).

Chapter 3

Geometrical dependence of quantum decoherence in circular arenas with side-wires

This paper was previously published as: Yuantao Xie, C. Le Priol and J. J. Heremans, “Geometrical dependence of quantum decoherence in circular arenas with side-wires”, *Journal of Physics: Condensed Matter* **28**, 495003 (2016). Reproduced with permission.

Geometrical dependence of quantum decoherence in circular arenas with side-wires

Yuantao Xie¹, Clément Le Priol² and Jean J Heremans¹

¹ Department of Physics, Virginia Tech, VA, USA

² Department of Physics, Ecole Polytechnique, 91128 Palaiseau, France

E-mail: heremans@vt.edu

Abstract

Low-temperature quantum phase coherence lengths were experimentally measured in mesoscopic circular arenas fabricated on InGaAs quantum wells. The arenas are connected to wide sample regions by short side-wires, to investigate the effects of geometry in comparison to intrinsic materials properties on quantum decoherence. Universal conductance fluctuations were used to quantify the phase coherence lengths as a function of temperature and geometry. The experimental data show a dependence of phase coherence lengths on side-wire length and width-to-length ratio, which is accounted for by the competing effects of decoherence by coupling to the classical environment and Nyquist decoherence in ergodic wires. The observed decay of phase coherence lengths with the increasing temperature is consistent with expectations. The work demonstrates that geometrical effects influence the measured mesoscopic quantum decoherence.

Keywords: quantum coherence, mesoscopic physics, quantum wires, quantum transport, universal conductance fluctuations

1. Introduction

Quantum interference phenomena and quantum decoherence in mesoscopic systems have attracted considerable attention. In mesoscopic systems, the quantum phases of carrier states can be randomized by inelastic or quasi-elastic scattering mechanisms such as electron–phonon and electron–electron scattering, and quantum decoherence results [1–4]. Also, the measurement of a quantum system necessitates coupling to the external environment, considered a classical system [5, 6], leading to environmental coupling decoherence [5–8]. At low temperature T , the inelastic or quasi-elastic scattering mechanisms are mitigated [5], and sufficiently long quantum phase coherence lengths L_ϕ are obtained to study electronic transport phenomena relying on quantum interference [9, 10]. Quantum decoherence has been studied in quantum dots [11–13], quantum wires [14–18], and quantum rings or ring networks [3, 9, 10, 19], among other geometries.

In this work, mesoscopic circular arenas connected to short side-wires were fabricated on an n-type InGaAs quantum well (QW) in an InGaAs/InAlAs heterostructure, and the quantum decoherence was measured and analyzed in these composite device structures. In the arena-wire samples used here, the dependence of the measured L_ϕ on the geometry of the wires shows that the device geometry plays a role in measured decoherence, by modulating both the importance of the environmental coupling decoherence and of decoherence by quasi-elastic electron–electron Nyquist scattering in low-dimensional systems [19–23]. Previous investigations focusing on quantum decoherence in composite or networked device structures include studies on coupled quantum dots or dot arrays [7, 24–26], as well as experimental and theoretical studies on quantum rings or ring arrays [19–21, 27–29]. The present work demonstrates the general importance of geometry in studying and using quantum-coherence phenomena. Knowledge of the effective quantum coherence lengths is

2 nm undoped InP
17 nm undoped $\text{In}_{0.52}\text{Al}_{0.48}\text{As}$
10 nm undoped $\text{In}_{0.53}\text{Ga}_{0.47}\text{As}$ (QW)
7 nm undoped $\text{In}_{0.52}\text{Al}_{0.48}\text{As}$
6 nm $\text{In}_{0.52}\text{Al}_{0.48}\text{As}$, Si doped $4 \times 10^{18} \text{ cm}^{-3}$
500 nm undoped $\text{In}_{0.52}\text{Al}_{0.48}\text{As}$ buffer
SI InP (001) substrate

Figure 1. Layer sequence of the bottom-doped InGaAs/InAlAs heterostructure, with the $\text{In}_{0.53}\text{Ga}_{0.47}\text{As}$ quantum well (red) located 19 nm below the surface.

important, among other areas, in the characterization of new quantum states of matter, particularly when the quantum states are realized in mesoscopic systems or if the states are expected to exhibit characteristic quantum-coherent transport phenomena only over length scales comparable to their effective quantum coherence lengths.

The length L_ϕ is used as a measure of quantum coherence and is, in this work, measured as function of sample geometry and T , by universal conductance fluctuations (UCFs), reproducible and aperiodic conductance variations originating in quantum interference in mesoscopic systems [1, 4, 22, 30, 31]. Quantum coherence effects are discernible in the correlation function characterizing UCFs, providing a precise way of extracting values for L_ϕ . Weak-antilocalization (WAL) is also present in the samples [17, 18, 32–34], yet is masked by a strong UCF signal, and UCFs are hence preferred in the present work for obtaining L_ϕ .

2. Experiments and analysis

The mesoscopic geometries are fabricated on the InGaAs/InAlAs heterostructure by electron-beam lithography and wet etching. The heterostructure schematically depicted in figure 1 was grown by molecular-beam epitaxy on semi-insulating InP (001) substrate and consists of, from bottom to top, a 500 nm $\text{In}_{0.52}\text{Al}_{0.48}\text{As}$ buffer, a 6 nm $\text{In}_{0.52}\text{Al}_{0.48}\text{As}$ n-doping layer, a 7 nm $\text{In}_{0.52}\text{Al}_{0.48}\text{As}$ spacer, the 10 nm wide $\text{In}_{0.53}\text{Ga}_{0.47}\text{As}$ electron QW, a 17 nm $\text{In}_{0.52}\text{Al}_{0.48}\text{As}$ spacer, and a 2 nm undoped InP cap layer. In this lattice-matched structure, the $\text{In}_{0.52}\text{Al}_{0.48}\text{As}$ doping layer is thus situated below the $\text{In}_{0.53}\text{Ga}_{0.47}\text{As}$ QW, which leads to an asymmetric QW confinement potential for the two-dimensional electron system (2DES) and hence a substantial spin-orbit interaction, but depresses the electron mobility μ in the 2DES, compared with other $\text{In}_{0.53}\text{Ga}_{0.47}\text{As}/\text{In}_{0.52}\text{Al}_{0.48}\text{As}$ heterostructures [35, 36]. The 2DES areal carrier density $N_s = 2.02 \times 10^{16} \text{ m}^{-2}$ and $\mu = 1.49 \text{ m}^2 (\text{Vs})^{-1}$, evaluated from van der Pauw measurements at $T = 0.40 \text{ K}$. Hall effect and Shubnikov-de Haas oscillations yield consistent results for N_s , and transport parameters do not vary significantly in the range of T of our measurement, from 0.40 K to 5.0 K. Calculated transport parameters, such as the elastic scattering time $\tau_e = 0.97 \text{ ps}$, the mean-free path $\lambda_e = 0.77 \text{ } \mu\text{m}$ ($T = 0.40 \text{ K}$) and the electron diffusion

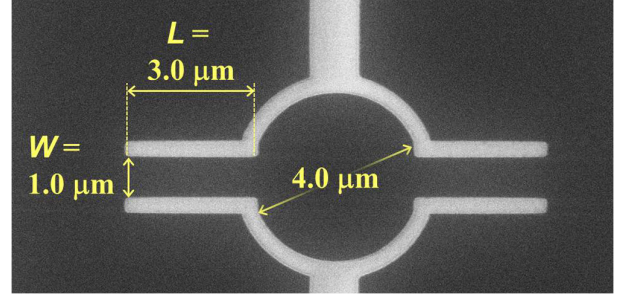


Figure 2. Scanning electron micrograph of a typical circular arena with side-wires. The lighter areas depict wet-etched trenches forming insulating barriers for the quantum well electrons, and delineating the devices. The central circular arenas in all samples have diameter $4.0 \text{ } \mu\text{m}$, while the width W and length L of the connecting side-wires vary (here $W = 1.0 \text{ } \mu\text{m}$, $L = 3.0 \text{ } \mu\text{m}$).

Table 1. Widths W and lengths L of the connecting side-wires of the mesoscopic geometries A, B, C, D, referring to figure 2.

Sample (μm)	A	B	C	D
W	1.4	1.0	1.0	0.6
L	1.0	1.0	3.0	1.0
L_ϕ	2.17	2.06	1.92	1.82

Note: The measured quantum phase coherence lengths L_ϕ ($T = 0.40 \text{ K}$) are obtained by the method illustrated in figure 5 (*cf.* text).

coefficient $D = 0.30 \text{ m}^2 \text{ s}^{-1}$, are evaluated accounting for nonparabolicity in the InGaAs conduction band, with a ratio of Γ -point effective mass m to free-electron mass of 0.0353 and a low T band gap of 813 meV. The calculated Fermi wavelength $\lambda_F = 17.6 \text{ nm}$, much smaller than the mesoscopic dimensions of the samples. Figure 2 contains a micrograph of a typical arena-wire geometry used in this work, with the characteristic dimensions indicated. The diameter of arenas is fixed at $4.0 \text{ } \mu\text{m}$, while the widths W and lengths L of the connecting side-wires vary as enumerated in table 1, where labels A to D denote the measured samples. Measurements occurred in a ^3He cryostat by standard four-contact lock-in techniques under a constant low-frequency ac current $I = 20 \text{ nA}$, sufficiently low to avoid affecting the electron T .

As example, figure 3 shows data for conductance G versus magnetic field B (magnetoconductance) obtained on arena D, parametrized in T . UCFs are clearly visible, diminishing in amplitude with increasing T , as expected. Around $B \sim 0$ a negative magnetoconductance due to WAL is also present [17, 18, 32–34], but is not used for analysis in the present work. We extracted L_ϕ by fitting a correlation function to the UCF data, with the correlation function defined as [11, 37]

$$\overline{\delta G(B)\delta G(B + \Delta B)} = \langle [G(B) - \langle G(B) \rangle][G(B + \Delta B) - \langle G(B) \rangle] \rangle \quad (1)$$

in which the angled brackets denote an average over a range of B . We obtain [38],

$$\overline{\delta G(B)\delta G(B + \Delta B)} = f\left(\frac{\Delta B}{2B_\phi}\right) \quad (2)$$

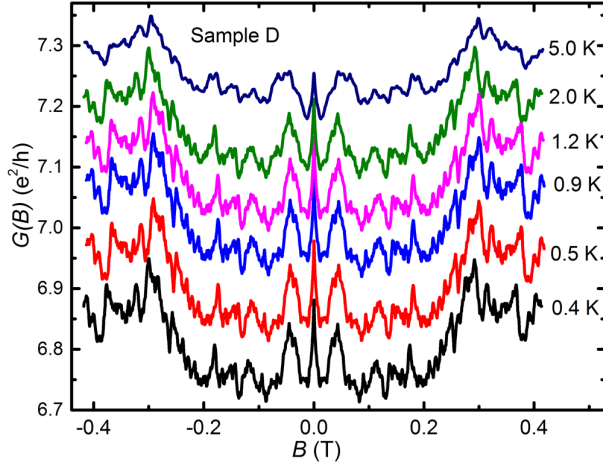


Figure 3. Magnetoconductance of sample D measured at different T , from 0.40 K to 5.0 K (data offset for clarity). Clear UCFs ride on a magnetoconductance background. At $T < 1.0$ K, the amplitude of the UCFs depends weakly on T , consistent with a saturation of L_ϕ , while for $T > 1.0$ K the amplitude decreases notably with increasing T . Around $B \sim 0$, a WAL negative magnetoconductance signal is present with amplitude comparable to the UCFs.

under the condition $B \gg B_\phi$, where the characteristic field B_ϕ is in the diffusive approximation defined as [39]

$$B_\phi = \hbar/(4eD\tau_\phi) \quad (3)$$

where τ_ϕ denotes the quantum phase coherence time, and $L_\phi = \sqrt{D\tau_\phi}$. B_ϕ characterizes the field under which one flux quantum h/e threads the area $8\pi L_\phi^2$. In equation (2), $f(x)$ is defined as

$$f(x) = \overline{\delta G^2(B)} \frac{1}{x} \Psi\left(\frac{1}{2} + \frac{1}{x}\right) \quad (4)$$

where $\Psi(x)$ is the digamma function. Here $\delta G^2(B)$ denotes $\overline{\delta G(B)\delta G(B+\Delta B)}$ evaluated at $\Delta B = 0$ (equation (2)) [38], and is calculated as a B -independent average over B .

Figure 4 depicts a correlation function calculated according to equation (1) for arena D, at $T = 0.40$ K. A high-pass filter was first applied to the magnetoconductance data (example in figure 3) to remove a slowly varying background due to classical magnetoconductance. The correlation function was calculated by averaging over B for $0.04 \text{ T} \leq B \leq \sim 0.36 \text{ T}$ thereby avoiding the WAL signal at low B . Further, estimating preliminarily $L_\phi \approx 1 \mu\text{m}$, we find $B_\phi \approx 0.16 \text{ mT} \ll 0.04 \text{ T}$ such that $B \gg B_\phi$ is also satisfied. Equation (2) was then used to fit the correlation function, as depicted in figure 4. The decay of the correlation function with increasing ΔB is expected at low ΔB , reflecting the increasingly uncorrelated UCFs as ΔB increases, and figure 4 indeed shows that equation (2) provides a good fit at low ΔB . At higher ΔB the fit does not include the quasi-periodic oscillation visible in figure 4, also frequently observed in other work [30, 37, 40]. The quasi-periodic oscillation originates in a fluctuation in the density of states [31, 40] related to pointer states [6, 31]. Under varying B the Fermi energy migrates through the energy levels of pointer states, which leads to oscillations in magnetoconductance, visible in

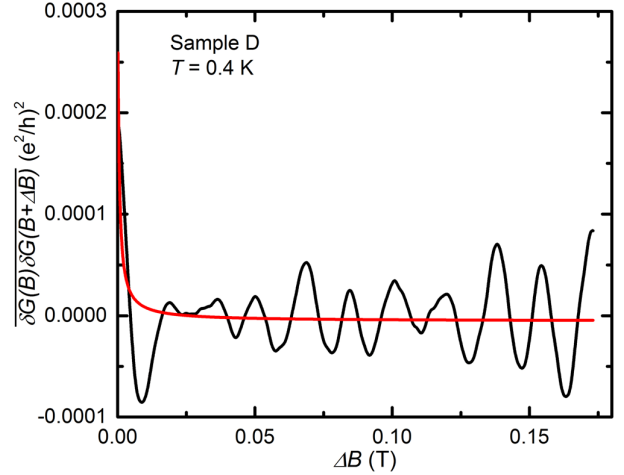


Figure 4. Correlation function for sample D, based on experimental data at $T = 0.40$ K. The black curve represents the correlation function calculated from experimental data using equation (1). The red curve represents the correlation function fitted according to equation (2), with $L_\phi = \sqrt{D\tau_\phi}$ as fitting parameter.

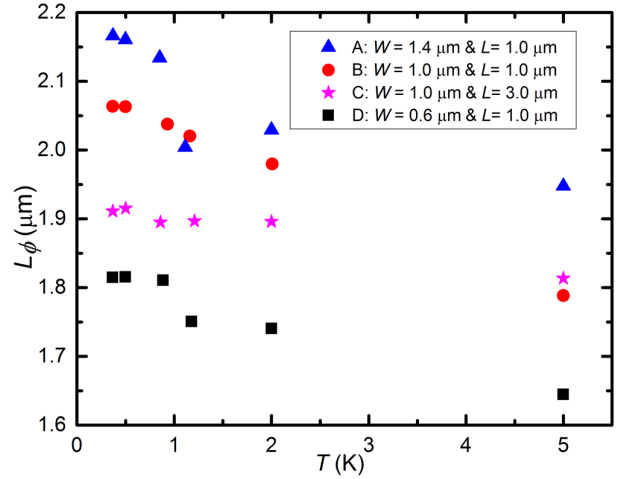


Figure 5. L_ϕ versus T extracted from the UCF data for samples A, B, C, D by fitting equation (2). As expected, for $T < 1.0$ K, L_ϕ shows saturation in T , while for $T > 1.0$ K, L_ϕ decreases with increasing T . Concerning geometrical dependence, L_ϕ decreases according to the sample series $A \rightarrow B \rightarrow C \rightarrow D$.

the correlation function in figure 4. For our samples, the correlation functions result from a superposition of a decaying contribution from UCFs and a quasi-periodic contribution from pointer states. Due to the obvious difference between the two contributions, extraction of B_ϕ by fitting with equation (2) is possible.

Fitting equation (2) with B_ϕ as fitting parameter for samples A to D and for all discrete measurement T , yields the values of L_ϕ depicted in figure 5. It is apparent that L_ϕ decreases according to the series of samples $A \rightarrow B \rightarrow C \rightarrow D$. To validate the results and conclusions, another approach was used as well to obtain B_ϕ , based on the half-width at half-maximum of the correlation function [11, 38]:

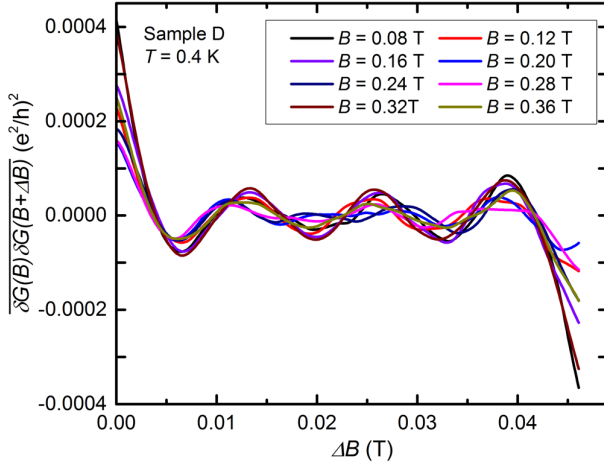


Figure 6. Correlation functions for sample D, based on experimental data at $T = 0.40$ K and calculated using equation (1). The data was sectioned into spans of B of range 0.08 T, and the correlation function calculated over this range around the center B as indicated. A bandpass filter was applied to mitigate oscillations as discussed in the text.

$$\overline{\delta G(B)\delta G(B + 12.4B_\phi)} = \overline{\delta G^2(B)}/2 \quad (5)$$

Under this definition, B_ϕ is the half-width of correlation function. The analysis using equation (5) also allows us to ascertain the corrections due to ballistic transport over the scale of the cyclotron radius, $\sim 1.3 \mu\text{m}$ in the range of B used for the analysis, can be neglected [1, 41]. The ballistic corrections may influence results if the device size ($\sim 4 \mu\text{m}$), the cyclotron radius, and $\lambda_e = 0.77 \mu\text{m}$ are comparable. The data was divided into equal sections of B of length 0.08 T, and the correlation function was calculated over this range of 0.08 T around a center B . To mitigate the oscillations discussed above, a bandpass filter was applied to the calculated correlation functions. In figure 6, the filtered correlation functions for the different sections of B are shown, labeled by their center B . From the calculated correlation functions as function of center B and of T , the B_ϕ (equation (5)) and L_ϕ were deduced. The dependence on center B indicated that the corrections due to ballistic transport can indeed be neglected. Values for L_ϕ for samples A–D were obtained as averages over center B and over T to provide a comparison with the values in figure 5. The analysis using equation (5) and subsequent averaging yields for sample A, $L_\phi = 1.26 \mu\text{m}$; for sample B, $L_\phi = 1.15 \mu\text{m}$; for sample C, $L_\phi = 1.14 \mu\text{m}$; for sample D, $L_\phi = 1.09 \mu\text{m}$. The values reproduce the observation that L_ϕ decreases according to the series of samples $A \rightarrow B \rightarrow C \rightarrow D$. The relative values of L_ϕ are also approximately maintained, as the values according to equation (5) are a fixed factor ~ 1.6 lower than the averages over T of the values found in figure 5. A more accurate correspondence should not be expected, since the sectioning in ranges of B , the bandpass filtering, and the averaging over B and T amount to data treatments that will affect absolute values of L_ϕ . While the analysis using equation (5) is hence not preferred for the most accurate values, it does extract from the UCF data the same observation as figure 5 about the decrease in L_ϕ according to the series $A \rightarrow B \rightarrow C \rightarrow D$.

3. Discussion of results

The values of L_ϕ contained in figure 5, with the values at $T = 0.40$ K repeated in table 1, show that L_ϕ is similar or only somewhat below the relevant geometrical length scales of the arena diameter, L and W . Therefore quantum coherence phenomena and in particular UCFs will not average out and will be prominent, as observed and as typical for mesoscopic systems. Decoherence effects impacting quantum coherence in the system composed of arena and side-wires, are indeed visible and can be analyzed as described below. It is to be noted that the system is not in the fully diffusive regime ($L_\phi \ll$ system size), but closer to the ergodic regime [19–21, 28, 38].

From figure 5 the dependence on T of L_ϕ is apparent. In agreement with theoretical and experimental work [1, 2, 16, 17, 19–22], L_ϕ decreases with increasing T , and at the lower $T < 1$ K, L_ϕ tends to saturate (the saturation has been extensively discussed in the literature [2, 13, 17, 22, 23, 42]). The saturated values of L_ϕ obey the same sample dependence as observed over $0.40 \text{ K} < T < 5.0 \text{ K}$ (namely L_ϕ decreasing from $A \rightarrow B \rightarrow C \rightarrow D$), and are listed in table 1. For $T > 1$ K, the data in figure 5 yields $L_\phi \sim T^{-p/2}$ with $p/2 \approx 0.06 \dots 0.08$, leading to a decoherence rate $\tau_\phi^{-1} \sim T^p$ with $p \approx 0.12 \dots 0.16$. At low T , the dependence on T of τ_ϕ^{-1} can originate in electron–electron scattering with large energy transfer [1, 2, 4, 16, 20, 22] with decoherence rate $\tau_{ee}^{-1} \sim T^2$ in both 1D (wires) and 2D (arenas), or can originate in electron–phonon scattering with $\tau_{ep}^{-1} \sim T^q$ with q experimentally determined as $2 \dots 4$ [2, 22], or can originate in thermal broadening of energy levels beyond the Thouless energy, leading to averaging over incoherent independent channels, with decoherence rate $\tau_T^{-1} \sim T^{1/2}$ [10]. Yet often limiting τ_ϕ at low T is quasi-elastic electron–electron Nyquist scattering [19, 21–23, 27], with a decoherence rate $\tau_N^{-1} \sim T^n$, where n depends on the geometry. Nyquist scattering results from dephasing of the state of a given electron by the fluctuating electromagnetic environment created by the other electrons. The geometry and how the geometry is sampled by the electron trajectories influence the effects of the potential fluctuations, resulting in a dependence on geometry of Nyquist scattering and of its dependence on T in mesoscopic devices [19, 21, 27]. In a long wire of width W in the diffusive regime ($L \gg L_\phi$), the Nyquist length $L_N = \sqrt{D\tau_N}$ is expressed as [3, 19, 21] $L_N = \sqrt{2(mWD^2/(\pi k_B T))}^{1/3}$, where k_B denotes the Boltzmann constant. Hence in this diffusive 1D regime $\tau_N^{-1} \sim T^{2/3}$ (while $\tau_N^{-1} \sim T$ in 2D). Yet, in a shorter 1D wire, diffusive trajectories are limited to the wire length L , and the trajectories can explore the whole length of the wire. In this ergodic regime, the Thouless time $\tau_D = L^2/D < \tau_\phi$, and the relevant modified Nyquist decoherence length L_C is given by [19–21, 28] $L_C = \sqrt{D\tau_C} = \sqrt{L_N^3/L} = 2^{3/4} D \sqrt{mW/(\pi k_B TL)}$. The dependence of L_C on geometry via $\sqrt{W/L}$ is explicit, as is the dependence $\tau_C^{-1} \sim T$. The dependence on T of τ_ϕ^{-1} can be approximated as resulting from the sum of the above decoherence rates, thus leading to the expectation $\frac{1}{2} \leq p \leq 4$. The

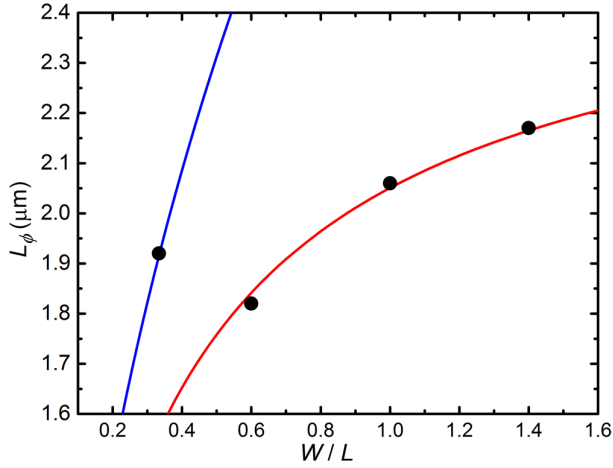


Figure 7. L_ϕ versus side-wire W/L , extracted from the UCF data for samples A, B, C, D at $T = 0.40$ K, represented as black solid circles. The red and blue solid lines represent the fit to equation (6), plotted for $L = 1.0 \mu\text{m}$ and $L = 3.0 \mu\text{m}$, *resp.*

observed p denotes a substantially weaker dependence on T , indicating that τ_ϕ is in the regime of T of the experiments subject to limits imposed by decoherence mechanisms insensitive to T . Such a mechanism can be found in quantum decoherence due to environmental coupling.

In figure 7, L_ϕ (at $T = 0.40$ K, in the saturation regime) is plotted versus W/L of the connecting side-wires. The datapoint at $W/L = 0.33$ corresponds to $L = 3.0 \mu\text{m}$ and $W = 1.0 \mu\text{m}$, while the datapoints with $W/L \geq 0.60$ all correspond to fixed $L = 1.0 \mu\text{m}$ and variable $W = 0.6 \mu\text{m}$, $1.0 \mu\text{m}$ and $1.4 \mu\text{m}$. Two geometrical parameters appear to influence L_ϕ , namely W/L and L . Table 1 and figure 7 show that L_ϕ increases with increasing W/L for $L = 1.0 \mu\text{m}$, yet also increases at longer $L = 3.0 \mu\text{m}$ ($W/L = 0.33$). The effect of increasing L can be captured by the influence of environmental coupling decoherence, expressing the total decoherence rate as $\tau_\phi^{-1} = \tau_{\phi 0}^{-1} + \tau_d^{-1}$. Here the second term denotes an escape rate with τ_d a dwell time, and is identified with quantum decoherence due to environmental coupling [5, 8]. The first term then equals the decoherence rate for an isolated system, with $\tau_d \rightarrow \infty$. A longer τ_d corresponds to weaker environmental coupling, longer τ_ϕ and longer L_ϕ . For a diffusive wire with $L > \lambda_e$, as is the case for $L = 3.0 \mu\text{m}$, we can estimate the probability for an electron emerging from the arena into the wire to be reflected back into the arena as $P = 1 - \lambda_e/L$. Then $\tau_d \propto P/(1 - P) = (L/\lambda_e) - 1$, expressing that a longer side-wire will lead to reduced escape rate and longer τ_ϕ . We attribute the rise in L_ϕ at longer $L = 3.0 \mu\text{m}$ ($W/L = 0.33$) to this dependence on L of the environmental coupling decoherence rate τ_d^{-1} . Figure 7 shows that L_ϕ increases with W at constant L . This trend is initially surprising given the expectation that in lateral quantum dots [5, 8], the wider the aperture connecting the quantum dots to the environment the shorter L_ϕ , since a wider aperture corresponds to shorter τ_d . Yet for a

short wire, $L_C \propto \sqrt{W/L}$ as found above. We surmise that the approximate dependence $L_\phi \propto \sqrt{W/L}$ observed in figure 7 for $W/L \geq 0.60$ arises from L_C limiting L_ϕ in the side-wires, since we measure the effective L_ϕ averaged over all decoherence phenomena occurring over the composite device. In this view, we surmise that τ_N^{-1} has a determining role in $\tau_{\phi 0}^{-1}$. We note that ascribing the observed dependence of L_ϕ on geometry to environmental coupling decoherence and Nyquist decoherence is a phenomenological description fitting this particular device configuration. The fact that the relevant length scales L_ϕ , λ_e , the arena diameter, L and W are similar and hence do not lie at limits assumed by theoretical arguments, introduces uncertainties in a decisive quantitative model for the decoherence phenomena in this compound system. Within the phenomenological description, converting from decoherence rates to lengths, we express the low T values of L_ϕ with

$$\frac{1}{L_\phi^2} = \frac{1}{L_\alpha^2((L/\lambda_e) - 1)} + \frac{1}{L_\beta^2(W/L)} \quad (6)$$

where L_α and L_β are fitting parameters.

A fit of equation (6) to the data in table 1 is depicted alongside the data in figure 7, for fitting values $L_\alpha = 4.69 \mu\text{m}$ and $L_\beta = 3.42 \mu\text{m}$ (fitting curves are parametrized in L). The phenomenological expression equation (6) captures the measured L_ϕ well and in particular reproduces the observed $\sqrt{W/L}$ dependence. Experimentally in the present work it is hence found that L_ϕ in the given arena-wire geometries can be understood from an interplay between environmental coupling decoherence and Nyquist decoherence in the ergodic short wires.

4. Conclusions

In conclusion, quantum decoherence was investigated in mesoscopic geometries composed of circular arenas coupled to short side-wires, by universal conductance fluctuations in quantum transport at low T . The mesoscopic geometries were fabricated on InGaAs quantum wells. A dependence of the quantum phase coherence length on side-wire length and side-wire width-to-length ratio was experimentally observed. Phenomenologically, an expression accounting for environmental coupling decoherence and Nyquist decoherence in the side-wires accounts for the observations. The present work underlines the importance of device geometry in using and quantifying quantum-coherence phenomena, a realization of foundational interest as well as of increasing relevance for quantum technologies.

Acknowledgments

The work was supported by the U.S. Department of Energy, Office of Basic Energy Sciences, Division of Materials Sciences and Engineering under award DOE DE-FG02-08ER46532.

References

- [1] Hackens B, Delfosse F, Faniel S, Gustin C, Boutry H, Wallart X, Bollaert S, Cappy A and Bayot V 2002 *Phys. Rev. B* **66** 241305
- [2] Lin J J and Bird J P 2002 *J. Phys.: Condens. Matter* **14** R501
- [3] Ferrier M, Angers L, Rowe A C H, Guéron S, Bouchiat H, Texier C, Montambaux G and Mailly D 2004 *Phys. Rev. Lett.* **93** 246804
- [4] Huibers A G, Switkes M, Marcus C M, Campman K and Gossard A C 1998 *Phys. Rev. Lett.* **81** 200
- [5] Bird J P, Micolich A P, Linke H, Ferry D K, Akis R, Ochiai Y, Aoyagi Y and Sugano T 1988 *J. Phys.: Condens. Matter* **10** L55
- [6] Ferry D K, Burke A M, Akis R, Brunner R, Day T E, Meisels R, Kuchar F, Bird J P and Bennett B R 2011 *Semicond. Sci. Technol.* **26** 043001
- [7] Elhassan M, Bird J P, Akis R, Ferry D K, Ida T and Ishibashi K 2005 *J. Phys.: Condens. Matter* **17** L351
- [8] Bird J P, Micolich A P, Ferry D K, Akis R, Ochiai Y, Aoyagi Y and Sugano T 1998 *Solid-State Electron.* **42** 1281
- [9] Ren S L, Heremans J J, Vijayaragunathan S, Mishima T D and Santos M B 2015 *J. Phys.: Condens. Matter* **27** 185801
- [10] Ren S L, Heremans J J, Gaspé C K, Vijayaragunathan S, Mishima T D and Santos M B 2013 *J. Phys.: Condens. Matter* **25** 435301
- [11] Bird J P, Ishibashi K, Ferry D K, Ochiai Y, Aoyagi Y and Sugano T 1995 *Phys. Rev. B* **51** 18037
- [12] Marcus C M, Westervelt R M, Hopkins P F and Gossard A C 1993 *Phys. Rev. B* **48** 2460
- [13] Pivin D P, Andresen A, Bird J P and Ferry D K 1999 *Phys. Rev. Lett.* **82** 4687
- [14] Doucot B and Rammal R 1986 *J. Phys.* **47** 973
- [15] Chandrasekhar V, Santhanam P and Prober D E 1991 *Phys. Rev. B* **44** 11203
- [16] Niimi Y, Baines Y, Capron T, Mailly D, Lo F Y, Wieck A D, Meunier T, Saminadayar L and Bäuerle C 2010 *Phys. Rev. B* **81** 245306
- [17] Kallaher R L, Heremans J J, Goel N, Chung S J and Santos M B 2010 *Phys. Rev. B* **81** 035335
- [18] Kallaher R L, Heremans J J, Roy W V and Borghs G 2013 *Phys. Rev. B* **88** 205407
- [19] Ferrier M, Rowe A C H, Guéron S, Bouchiat H, Texier C and Montambaux G 2008 *Phys. Rev. Lett.* **100** 146802
- [20] Capron T, Texier C, Montambaux G, Mailly D, Wieck A D and Saminadayar L 2013 *Phys. Rev. B* **87** 041307
- [21] Texier C, Delplace P and Montambaux G 2009 *Phys. Rev. B* **80** 205413
- [22] Rudolph M and Heremans J J 2011 *Phys. Rev. B* **83** 205410
- [23] Natelson D, Willett R L, West K W and Pfeiffer L N 2001 *Phys. Rev. Lett.* **86** 1821
- [24] Elhassan M *et al* 2001 *Phys. Rev. B* **64** 085325
- [25] Aoki N, Oonishi D, Iwase Y, Ochiai Y, Ishibashi K, Aoyagi Y and Bird J P 2002 *Appl. Phys. Lett.* **80** 2970
- [26] Fairbanks M S, Martin T P, Scannell B C, Marlow C A, Linke H and Taylor R P 2010 *Physica E* **42** 1205
- [27] Texier C 2007 *Phys. Rev. B* **76** 153312
- [28] Texier C and Montambaux G 2005 *Phys. Rev. B* **72** 115327
- [29] Ludwig T and Mirlin A D 2004 *Phys. Rev. B* **69** 193306
- [30] Jalabert R A, Baranger H U and Stone A D 1990 *Phys. Rev. Lett.* **65** 2442
- [31] Ferry D K, Akis R A, Pivin D P, Bird J P, Holmberg N, Badrieh F and Vasileska D 1998 *Physica E* **3** 137
- [32] Bergmann G 2010 *Int. J. Mod. Phys. B* **24** 215
- [33] McPhail S, Yasin C E, Hamilton A R, Simmons M Y, Linfield E H, Pepper M and Ritchie D A 2004 *Phys. Rev. B* **70** 245311
- [34] Deo V, Zhang Y, Soghomonian V and Heremans J J 2015 *Sci. Rep.* **5** 9487
- [35] Matsuoka T, Kobayashi E, Taniguchi K, Hamaguchi C and Sasa S 1990 *Japan. J. Appl. Phys.* **29** 2017
- [36] Diez E, Chen Y P, Avesque S, Hilke M, Peled E, Shahar D, Cerveró J M, Sivco D L and Cho A Y 2006 *Appl. Phys. Lett.* **88** 052107
- [37] Akis R, Ferry D K and Bird J P 1996 *Phys. Rev. B* **54** 17705
- [38] Akkermans E and Montambaux G 2007 *Mesoscopic Physics of Electrons and Photons* (Cambridge: Cambridge University Press)
- [39] Marcus C M, Clarke R M, Chan I H, Duruöz C I and Harris J S 1994 *Semicond. Sci. Technol.* **9** 1897
- [40] Ferry D K, Akis R and Bird J P 2005 *J. Phys.: Condens. Matter* **17** S1017
- [41] Bird J P, Ferry D K, Akis R, Ochiai Y, Ishibashi K, Aoyagi Y and Sugano T 1996 *Europhys. Lett.* **35** 529
- [42] Mohanty P, Jariwala E M Q and Webb R A 1997 *Phys. Rev. Lett.* **78** 3366

This paper was previously published as:
Yuanta Xie, C. Le Priol and J. J. Heremans,
"Geometrical dependence of quantum
decoherence in circular arenas with side-wires",
Journal of Physics: Condensed Matter **28**,
495003 (2016).

Chapter 4

Effect of wire length on mesoscopic quantum coherence in InGaAs wires

To be submitted to Nano Letters or Physical Review B.

Effect of wire length on mesoscopic quantum coherence in InGaAs wires

Yuantao Xie and J. J. Heremans*

Department of Physics, Virginia Tech, Blacksburg, VA 24060, USA

Clément Le Priol

Physics Department, Ecole Polytechnique, 91128 Palaiseau, France

(Dated: December 14, 2017)

Quantum phase coherence lengths were experimentally measured in mesoscopic nanolithographic wires to investigate the effects of wire length on quantum decoherence, via mechanisms such as coupling to an external classical environment. The low-temperature measurements of the quantum phase coherence lengths use antilocalization on wires fabricated from an InGaAs/InAlAs heterostructure. It is observed that longer wire lengths result in longer quantum phase coherence lengths, in the long-wire limit reaching the intrinsic coherence length in the material. The results are quantitatively understood from the observation that longer wires average out the quantum decoherence introduced at the end sections by coupling to the external environment. The experimental results are compatible with a model expressing reduced backscattered amplitude due to quantum interference at the wire ends. The work demonstrates that device geometry and coupling to the environment have to be taken into account in quantum coherence, of relevance in quantum technologies.

PACS numbers: 73.63.Nm, 73.23.-b, 73.20.Fz, 03.65.Yz

I. INTRODUCTION

The study of quantum coherence of charge carriers in the solid-state has attracted consistent attention for the insights it provides into the fundamental properties of quantum systems, and for the importance it carries for the field of quantum information processing. Mesoscopic solid-state systems, larger than the atomic scale but still of a length scale preserving quantum phenomena, constitute a ready platform to study mechanisms limiting quantum coherence of electrons. In particular, the spatial extent along which quantum coherence is maintained in nanoscale wire geometries is of relevance today due to the interest in hybrid semiconductor-superconductor nanowires for the study of solid-state Majorana quasiparticles, where the Majorana states are localized at the ends of wires along the length of which quantum coherence of the Majorana states must be preserved^{1,2}. The carrier quantum phase coherence length L_ϕ is defined as an average length scale over which quantum coherence is maintained, and thus beyond which the relative quantum phases of the carrier states are randomized. In mesoscopic systems several decoherence mechanisms limit L_ϕ . Among these are inelastic or quasi-elastic scattering mechanisms such as electron-phonon and electron-electron scattering³⁻⁵, and effectively by spin decoherence effects. Decoherence can also result from energy level broadening beyond the Thouless energy, thermally or due to excitation voltages or currents, causing averaging over independent and incoherent channels⁶. At low temperature T , many decoherence mechanisms dependent on energy exchange are suppressed^{5,7}, and L_ϕ reaches values sufficiently long to study electronic transport phenomena relying on quantum interference in mesoscopic devices^{6,8}. Yet geometrical effects also play a role⁹, e.g. via environmental

coupling decoherence^{4,7,10-13} originating from the fact that measurement of a quantum system necessitates coupling to the external environment, taken as a classical system^{7,10,14,15}. The present work demonstrates the general importance of device geometry -particularly wire length- and of environmental coupling decoherence in studying and using quantum-coherence phenomena, among others in the characterization of new quantum states of matter realized in mesoscopic systems where quantum-coherent phenomena occur only over length scales comparable to the effective L_ϕ . Previous studies relating to the dependence of quantum decoherence on mesoscopic geometry and device size have been performed in quantum wires¹⁶⁻²⁴, quantum rings²⁵⁻²⁷, quantum ring arrays or cylinders^{3,28-30}, and quantum dots^{9,12,31-33}.

In this work parallel arrays of wires of various lengths were fabricated on an InGaAs/InAlAs heterostructure. The heterostructure is essentially free of any magnetic impurities, and is thus a good host for studying intrinsic decoherence mechanisms^{12,33}. Each wire array consists of 20 parallel quasi-one-dimensional (Q1D) wires of given wire length L . Q1D denotes that the conducting wire width W is shorter than the mobility mean-free-path and than L_ϕ , but substantially larger than the Fermi wavelength λ_F such that lateral quantization and subband transport physics can be neglected. L_ϕ as a measure of quantum coherence is in this work extracted as function of L and T by the quantum interference effect of weak antilocalization (WAL)^{19,21,34-37}. As a quantum interference effect, WAL is a sensitive probe of quantum coherence and originates in quantum coherence corrections to the conductance, caused by interference between backscattered time-reversed electron trajectories. The interference leads to a conductance with a characteristic

dependence on the magnetic field B applied normally to the surface, as modified (in the case of WAL) by strong spin-orbit interaction (SOI)³⁸. Due to the existence of SOI in the InGaAs/InAlAs heterostructure, analysis of the characteristic magnetoresistance due to WAL affords a path to extract values for L_ϕ . The WAL correction depends on the random quantum phase accumulated over the time-reversed trajectories, leading to a sensitivity of the magnetoresistance to L_ϕ . In mesoscopic geometries communicating with the wider environment, the WAL correction also depends on the return probability of those time-reversed pairs that originate in the geometry and partially sample the environment^{18,39,40}. Given the relatively higher importance of such trajectories in shorter wires, the smaller average return probability at the end of shorter wires tends to reduce L_ϕ in shorter wires when compared to longer wires. The lower return probability equates to decoherence due to coupling to the environment. Coupling to the environment can equivalently be expressed in terms of a dwell time τ_d in the mesoscopic structure, with shorter τ_d equivalent to stronger coupling and associated with shorter quantum phase coherence time τ_ϕ . Previous work^{12,33} has noted that a larger lateral quantum dot size leads to a shorter τ_ϕ , explained by invoking τ_d proportional to system size, limiting τ_ϕ at low T . A longer $L_\phi = \sqrt{D\tau_\phi}$ (where D denotes the carrier diffusion coefficient) is then expected in systems of larger size such as in longer Q1D wires. In the present experiments, L_ϕ indeed has a positive correlation with L over a range of T , consistent with environmental coupling decoherence quantifiable using WAL. The dependence of L_ϕ on T in the present experiments is consistent with Nyquist scattering due to quasi-elastic electron-electron interactions^{5,28,29,41}, a main decoherence source at low T . In Nyquist scattering a random phase is accumulated by the fluctuations of the electromagnetic field generated by the other electrons.

II. MATERIAL AND SAMPLE PROPERTIES

Hall bar mesas were defined on the InGaAs/InAlAs heterostructure by photolithography and wet etching, and subsequently arrays of 20 parallel Q1D wires were defined on the mesas by electron-beam lithography and wet etching (Fig. 1. a). Wire lengths were $L=4.0\ \mu\text{m}$, $6.0\ \mu\text{m}$ and $11.0\ \mu\text{m}$, with lithographic width $W_{lith} = 0.70\ \mu\text{m}$ (Table. I). As quantified below from the measured wire resistance, the effective conducting width W is narrower than W_{lith} due to side etching and existence of a depletion layer. A typical set of Q1D wires is depicted in the micrograph of Fig. 1. a. Measuring a large number of wires in parallel (here $N=20$) suppresses universal conductance fluctuations, the amplitude of which scales as $1/\sqrt{NLW}$ ⁴². The suppression is beneficial, since strong universal conductance fluctuations can impede the WAL analysis. The longitudinal magnetotransport coefficient

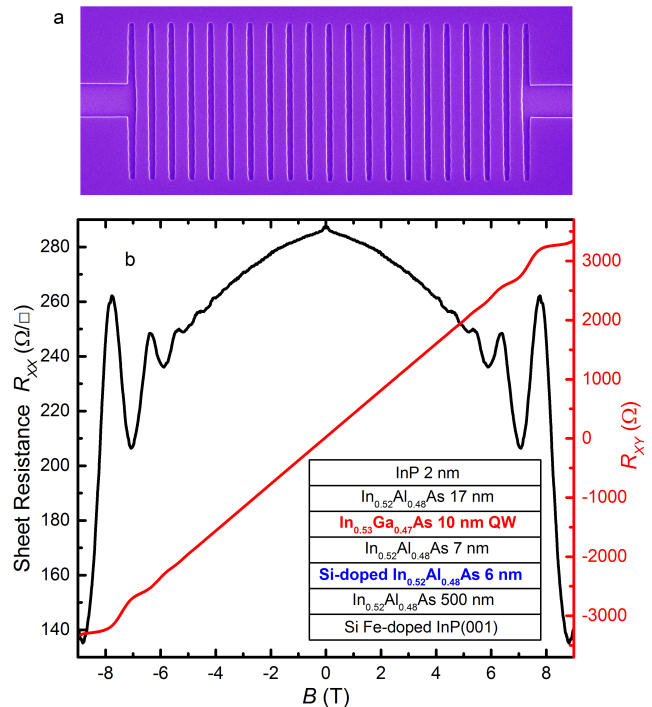


FIG. 1: Panel a: Scanning electron micrograph of a typical Q1D wire array, here with $L = 11.0\ \mu\text{m}$. Etched trenches form insulating barriers for the 2DES, thus delineating the conducting wires. The lithographic wire width is $0.70\ \mu\text{m}$ for all wires. Panel b: R_{XX} (black) and R_{XY} (red) at 0.38 K on a Hall bar fabricated on the InGaAs/InAlAs heterostructure, with the heterostructure layer sequence depicted in the inset.

R_{XX} and the Hall coefficient R_{XY} as measured on a macroscopic Hall bar at $T = 0.38$ K are depicted *vs* B in Fig. 1. b, showing Shubnikov-de Haas oscillations and an incipient integer quantum Hall effect at higher B . The inset of Fig. 1. b contains the heterostructure layer sequence, which was grown by molecular-beam epitaxy on semi-insulating InP (001) substrate. From bottom to top the lattice-matched layer sequence consists of a 500 nm In_{0.52}Al_{0.48}As buffer, a 6 nm Si-doped In_{0.52}Al_{0.48}As layer, a 7 nm In_{0.52}Al_{0.48}As spacer, the 10 nm wide In_{0.53}Ga_{0.47}As electron quantum well (QW), a 17 nm In_{0.52}Al_{0.48}As spacer, and a 2 nm undoped InP cap layer. Electrons are provided to the QW by 6 nm Si-doped In_{0.52}Al_{0.48}As, and the two-dimensional electron system (2DES) is hosted in QW with areal carrier density $N_s = 1.58 \times 10^{16}\ \text{m}^{-2}$ as determined on the Hall bar at $T = 0.38$ K from both R_{XY} and Shubnikov-de Haas oscillations (Fig. 1. b). The unpatterned 2DES' sheet resistance is obtained as $R_{\square 2D} = \frac{1}{N_s e \mu_{2D}} = 287\ \Omega/\square$, with mobility $\mu_{2D} = 1.38\ \text{m}^2/(\text{Vs})$. In the range $0.38\ \text{K} \leq T \leq 10.0\ \text{K}$ of the measurements both μ_{2D} and N_s do not vary significantly. Other parameters depending on μ_{2D} and N_s are evaluated accounting for nonparabolicity in

TABLE I: Lengths and lithographic widths of the wires, quantum phase coherence lengths at $T = 0.38$ K, and exponent p of the T -dependence of the quantum decoherence rate for T varying from 1.0 K to 10.0 K.

Wires	$L=11.0 \mu\text{m}$ $W_{lith}=0.70 \mu\text{m}$	$L=6.0 \mu\text{m}$ $W_{lith}=0.70 \mu\text{m}$	$L=4.0 \mu\text{m}$ $W_{lith}=0.70 \mu\text{m}$
L_ϕ (μm)	1.42	1.27	1.04
$\tau_\phi^{-1} \sim T^p$	$p = 0.690 \pm 0.030$	$p = 0.679 \pm 0.056$	$p = 0.716 \pm 0.052$

the InGaAs conduction band, with a Γ -point ratio of effective mass to free-electron mass of 0.0353 and a low T band gap of 813 meV. In the unpatterned 2DES we have the elastic scattering time $\tau_{e2D} = 0.81$ ps, the mean-free-path $\ell_{e2D} = 0.59 \mu\text{m}$, and $\lambda_F = 19.9$ nm ($\ll W$), and the diffusion constant $D_{2D} = 0.11$ m²/s. Situating the In_{0.52}Al_{0.48}As doping layer below the In_{0.53}Ga_{0.47}As QW results in asymmetry in the QW confinement potential for the 2DES and in a substantial SOI, yet also depresses μ_{2D} compared with other In_{0.53}Ga_{0.47}As/In_{0.52}Al_{0.48}As heterostructures^{43,44}. Measurements occurred in a ³He cryostat using four-contact low-frequency lock-in techniques under constant current $I = 20$ nA, sufficiently low to avoid heating the 2DES. For each array of 20 parallel wires, the measured magnetoresistance $R_m(B)$ includes a magnetoresistance $R(B)$ of each of the identical wires in the arrays and a series magnetoresistance of the unpatterned 2DES regions. Hence $R_m(B) = \frac{R(B)}{20} + \frac{L_{2D}}{W_{2D}} R_{\square 2D}(B)$, where L_{2D} and W_{2D} are the dimensions of the unpatterned regions known from pattern design, and the unpatterned sheet magnetoresistance $R_{\square 2D}(B)$ is measured on the Hall bar. $R(B)$ is then obtained as $R(B) = 20(R_m(B) - \frac{L_{2D}}{W_{2D}} R_{\square 2D}(B))$, and $R(B)$ yields the wire magnetoconductance $G(B) = 1/R(B)$ required for WAL analysis. As an example, Fig. 2 shows $\Delta G(B) = G(B) - G(B = 0)$ for the 6.0 μm wires at T from 0.38 K to 10.0 K. The sharp negative magnetoconductance for $B \lesssim 12$ mT followed by a positive magnetoconductance is characteristic of WAL.

III. 2D & Q1D APPROACH TO WEAK-ANTILOCALIZATION

The following discussion introduce the WAL analysis appropriate for Q1D wires. The quantum correction to the 2D conductivity $\sigma_{2D} = (L/W)G$ is proportional the length over which a wave packet retains coherence. In the absence of SOI for a system of width W at $B = 0$ the quantum correction per spin channel $\delta\sigma_{2D}$ is expressed as^{42,45}:

$$\delta\sigma_{2D} = -\frac{1}{2} \frac{e^2}{\pi\hbar} \frac{L_\phi}{W} \quad (1)$$

Under applied B , the Aharonov-Bohm phases for time-reversed paths differ in sign, and hence time-reversal symmetry breaking due to the accumulation of

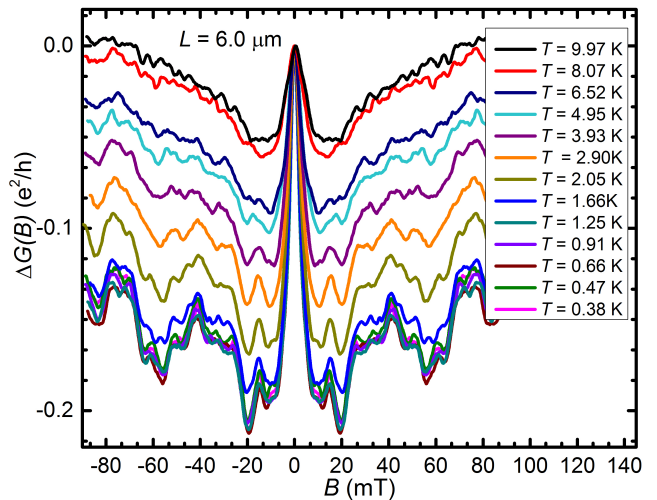


FIG. 2: Magnetoconductance $\Delta G(B)$ vs B for the wires with $L = 6.0 \mu\text{m}$ parameterized in T .

Aharonov-Bohm phases will reduce the effective coherence length. An effective time-reversal symmetry breaking length known as the magnetic length L_B is introduced, which forms a limit for the effective coherence length $1/\sqrt{L_\phi^{-2} + L_B^{-2}}$. The effect of L_B is to delay accumulation of magnetic flux Φ_B and its associated Aharonov-Bohm phases, to higher B in a narrow wire, and hence to spread out the magnetoresistance features over higher B . The Aharonov-Bohm phase weakens the constructive interference of time-reversed paths and leads to the negative magnetoresistance characteristic of weak-localization. Under SOI however, the effective vector potential due to SOI also introduces spin-dependent Aharonov-Casher phase shifts, leading to spin decoherence (properly dephasing) with a characteristic length scale L_{so} ⁴⁶. The pairing of time-reversed trajectories (Cooperons) then leads to singlet and triplet contributions to the quantum correction $\delta\sigma_{2D}$. Under SOI L_ϕ is thus replaced by a combination of length scales categorized as singlet and triplet lengths^{19,21,45-50}. The singlet length scale $L_{0,0}$ is expressed as:

$$L_{0,0} = \left(L_\phi^{-2} + L_B^{-2} \right)^{-\frac{1}{2}} \quad (2)$$

The singlet $L_{0,0}$ does not contain L_{so} and is not sensitive to spin decoherence under SOI since the correspond-

ing total spin adds to zero^{19,21,46,50}. Only L_ϕ and L_B limit $L_{0,0}$. The triplet length scales $L_{1,m}$ ($m = \pm 1, 0$) are expressed as:

$$\begin{aligned} L_{1,\pm 1} &= \left(L_\phi^{-2} + L_{so}^{-2} + L_B^{-2} \right)^{-\frac{1}{2}} \\ L_{1,0} &= \left(L_\phi^{-2} + 2L_{so}^{-2} + L_B^{-2} \right)^{-\frac{1}{2}} \end{aligned} \quad (3)$$

The difference between $L_{1,\pm 1}$ and $L_{1,0}$ lies in anisotropic spin decoherence in 2D systems³⁴, and does not exist in 3D systems^{45,49}. The triplet contributions to $\delta\sigma_{2D}$ will be negative (leading to positive magnetoconductance) while the singlet contribution will be positive and will reverse weak-localization to WAL (negative magnetoconductance at low B). In wide, laterally unconstrained 2D systems, $L_B = l_m \equiv \sqrt{\hbar/eB}$. When the 2DES is narrowed to a Q1D wire with $W \lesssim l_m$ the accumulation of Aharonov-Bohm phases is impeded (equivalently, the wave function boundary conditions are modified). If also $l_e \gtrsim 0.6W$, ballistic magnetic flux cancellation has to be considered due to self-crossing of time-reversed trajectories in narrow wires. Considered together, for low B , L_B is then modified to^{19,21,29,46,51}:

$$L_B = l_m \sqrt{\frac{C_1 l_m^2 \ell_{e1D}}{W^3}} \quad (4)$$

Here $C_1 = 4.75$ for specular boundary scattering and $C_1 = 2\pi$ for diffusive boundary scattering^{19,21,51}, while ℓ_{e1D} is the mean-free-path in the Q1D wire. From Eq. (1), the quantum correction $\delta\sigma_{2D}$ is finally expressed as:

$$\delta\sigma_{2D} = -\frac{1}{2} \frac{e^2}{\pi\hbar} \frac{1}{W} \left(\sum_{m=0,\pm 1} L_{1,m} - L_{0,0} \right) \quad (5)$$

The measured conductance correction $\delta G(B) = G(B) - G_0$, is related to $\delta\sigma_{2D}$ by $\delta G(B) = (W/L)\delta\sigma_{2D}$, with G_0 the classical conductance of the wire ($G_0 \neq G(0)$ due to the effects of L_ϕ and L_{so}). The dependence of $\delta G(B)$ on B thus reduces to a combination of length ratios^{19,21,45,46,49}:

$$\delta G(B) = -\frac{1}{2} \frac{e^2}{\pi\hbar} \frac{1}{L} (L_{1,+1} + L_{1,-1} + L_{1,0} - L_{0,0}) \quad (6)$$

The experimental data can be directly compared to fits to Eq. (6) since $\Delta G(B) = G(B) - G(0) = \delta G(B) - \delta G(0)$. With the presence of a depletion layer in InGaAs mesoscopic structures, a smooth potential is formed at the wire edges, and we expect boundary scattering to be specular. Hence $C_1=4.75$ is used^{21,51,52}. Values for L_ϕ , L_{so} and ℓ_{e1D} (entering in Eq. (4)) are used as fitting parameters to fit the experimental data for $\Delta G(B)$

to Eq. (6). It is to be noted that similarly to previous work²¹, we expect $\ell_{e1D} < \ell_{e2D}$, a drop in electron mean-free-path in the wire compared to the unpatterned 2DES (in Ref.²¹ equivalently expressed via a drop in D). The WAL analysis depends on ℓ_{e1D} and on W , neither of which are known a priori. While ℓ_{e1D} is obtained as a fitting parameter, W can be calculated as follows. A first estimate W_0 is obtained by assuming the sheet resistance in the wires $R_{\square 1D}$ equals $R_{\square 2D}$, and using $R_{B=0} = \frac{L}{W} R_{\square 2D}$ at $T=0.38$ K. By a least squares fitting over L , we obtain $W_0 = 0.34 \mu\text{m}$. By using the known wire resistance $R = \frac{\hbar}{e^2} \sqrt{\frac{2\pi}{N_s}} \frac{L}{W \ell_{e1D}}$ and assuming constant N_s , we obtain $W \rightarrow \frac{\ell_{e2D}}{\ell_{e1D}} W_0$. By consistent fitting over the 3 wire sets, we arrive at $\ell_{e1D} = 0.50 \mu\text{m}$ and $W = 0.41 \mu\text{m}$, common to the 3 wire sets.

IV. DATA ANALYSIS AND RESULTS

Fig. 3 depicts examples of fits of Eq. (6) to $\Delta G(B)$ for the Q1D wires with $L=11.0 \mu\text{m}$, $6.0 \mu\text{m}$ and $4.0 \mu\text{m}$. It is apparent that the model captures the experiments well. The fluctuations in magnetoconductance are due to universal conductance fluctuations surviving the averaging process, aggravated by the subtraction of the series resistance of unpatterned areas and the calculation of the magnetoconductance correction $\Delta G(B)$. Since the characteristic magnetoresistance due to WAL occurs predominantly at lower B , the fitting is not affected by the fluctuations.

In Fig. 4 the extracted L_ϕ is plotted *vs* T , parametrized in L . Prior to discussing the dependence of L_ϕ on L we note that L_ϕ decreases with increasing T , in agreement with other work, both theoretical and experimental^{4,5,19,20,53,54}. At lower $T < 1$ K a saturation of L_ϕ appears, also previously observed and discussed^{5,19,20,55-59}. While the origin of the saturation is under debate, several causes can be ruled out in our experiments. Magnetic impurities possibly present in metal samples are typically absent in semiconductor heterostructures grown by molecular-beam epitaxy^{12,33}. To rule out thermal causes due to sample current, we measured the wire magnetoresistance at $T=0.38$ K with $10 \text{ nA} \leq I \leq 100 \text{ nA}$. The magnetoresistance remained identical for $10 \text{ nA} \leq I \leq 50 \text{ nA}$, and at 100 nA shows a smaller WAL amplitude, implying that for $I \leq 50 \text{ nA}$ electron heating can be neglected. Present results were all measured at $I = 20 \text{ nA}$. Further, T in the measurement system is calibrated using Shubnikov-de Haas oscillations in a high- μ 2DES in GaAs/AlGaAs. The saturation of L_ϕ is not the focus of the present work and won't be discussed hereunder. A drop in L_ϕ with increasing T for all samples is present in Fig. 4 for $T > 1$ K. Analysis shows that for $T > 1$ K, the results fit $L_\phi \sim T^{-p/2}$ with $p/2 \approx 0.34 \pm 0.02$, leading to a decoherence rate $\tau_\phi^{-1} \sim T^p$ with $p \approx 0.69 \pm 0.03$.

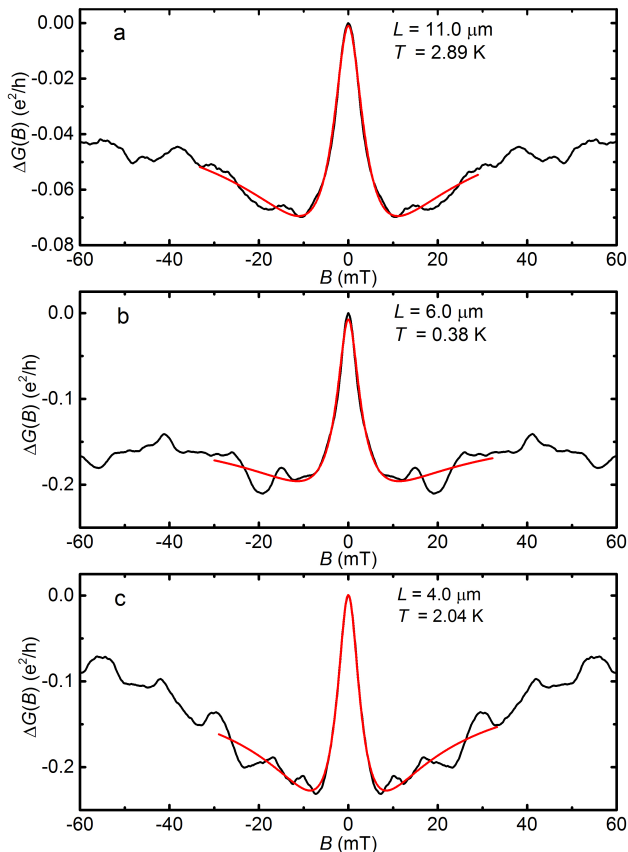


FIG. 3: Panel a: magnetoconductance $\Delta G(B)$ vs B for wire $L = 11.0 \mu\text{m}$ at $T = 2.89 \text{ K}$ (data in back, fitting of Eq. (6) in red). Panel b: magnetoconductance $\Delta G(B)$ vs B for wire $L = 6.0 \mu\text{m}$ at $T = 0.38 \text{ K}$ (data in back, fitting of Eq. (6) in red). Panel c: magnetoconductance $\Delta G(B)$ vs B for wire $L = 4.0 \mu\text{m}$ at $T = 2.04 \text{ K}$ (data in back, fitting of Eq. (6) in red).

Values for p are listed in Table. I. The dependence on T of τ_ϕ^{-1} can have several causes. Electron-phonon scattering leads to a decoherence rate $\tau_{ep}^{-1} \sim T^q$ with q experimentally determined as $2 \dots 4$ ^{5,20}. Electron-electron scattering^{4,5,20,31} with large energy transfer leads to a decoherence rate $\tau_{ee}^{-1} \sim T^2$ in 1D and 2D, while quasi-elastic Nyquist scattering leads to a decoherence rate $\tau_N^{-1} \sim T^{2/3}$ in 1D^{20,59} and $\tau_N^{-1} \sim T$ in 2D^{4,31,42,60}. Averaging of transport phenomena over incoherent channels, expressed as broadening of energy levels beyond the Thouless energy, leads to a decoherence rate $\tau_T^{-1} \sim T^{1/2}$, and can result from thermal effects or excitation by applied voltages or currents⁶. For the Q1D wires by fitting $L_\phi \sim T^{-p/2}$, we obtain $p = 0.690$, 0.679 and 0.716 respectively (Table. I), consistent with Nyquist scattering in 1D with $\tau_N^{-1} \sim T^{2/3}$. An analysis of L_ϕ on the unpatterned 2DES in the Hall bar (not shown) shows $L_\phi \sim T^{-p/2}$ with $p \approx 1.04$, consistent with a 2D Nyquist decoherence rate $\tau_N^{-1} \sim T$. According to discussion above and results in Fig. 4, we can conclude

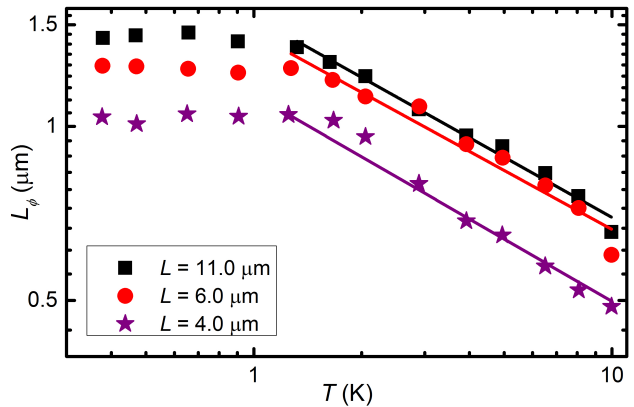


FIG. 4: Phase coherence lengths L_ϕ vs T extracted from $\Delta G(B)$ using 1D WAL analysis for the Q1D wire sets with $L = 4.0 \mu\text{m}$, $6.0 \mu\text{m}$ and $11.0 \mu\text{m}$.

that quasi-elastic Nyquist scattering plays a role in limiting L_ϕ in our samples.

Fig. 4 shows that L_ϕ maintains a positive correlation with L , whereby as L increases, L_ϕ also increases. The saturated values of L_ϕ for $T < 1 \text{ K}$ obey the same dependence on L as observed over $0.38 \text{ K} < T < 10.0 \text{ K}$. For $T < 1 \text{ K}$, L_ϕ of the long wires with $L = 11.0 \mu\text{m}$, reaches $1.42 \mu\text{m}$, substantially longer than $L_\phi = 1.04 \mu\text{m}$ for the shorter wire with $L = 4.0 \mu\text{m}$. Fig. 5 shows the L_ϕ measured at $T = 0.38 \text{ K}$ (saturated value) plotted vs L . The positive correlation of L_ϕ with L finds an explanation in the interaction of the quantum states in the wires with the classical environment^{18,39}. With the wires connected to the environment, taken as a macroscopic classical system, environmental coupling decoherence is introduced at the endpoints of the wires, while the decoherence is weaker into the wires from the endpoints. Averaging over L then shows that shorter wires are more sensitive to environmental coupling decoherence and will exhibit shorter L_ϕ .

The dependence of L_ϕ on both L and on T in Fig. 4 point to the importance of geometrical effects, expressed in environmental coupling decoherence. In general, the observations illustrate the sensitivity of quantum coherence in mesoscopic structures to interactions with wide neighboring regions. Environmental coupling decoherence can be quantified using a dwell time τ_d , via a total decoherence rate given by $\tau_\phi^{-1} = \tau_{\phi 0}^{-1} + \tau_d^{-1}$. The term $1/\tau_d$ quantifies an escape rate out of the quantum system, associated with environmental coupling, and hence denotes the environmental decoherence rate. The term $1/\tau_{\phi 0}$ equals the decoherence rate for an isolated system where $\tau_d \rightarrow \infty$. The dwell time has been invoked for decoherence in lateral quantum dots^{12,33}, while experiments show that the wider the aperture connecting the quantum dots to the environment, the shorter is τ_ϕ due to shorter τ_d ^{7,13}. In the present wires it is possible

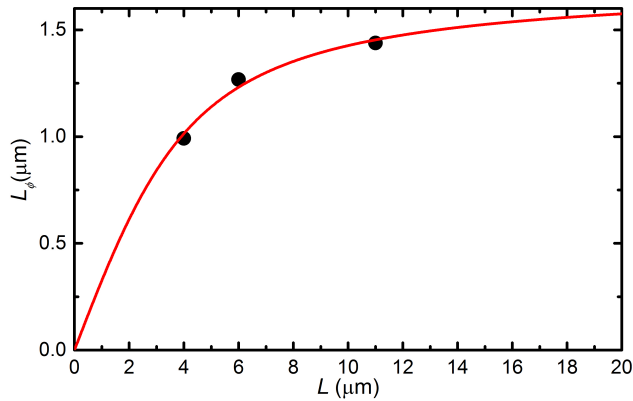


FIG. 5: Phase coherence lengths L_ϕ vs L at $T = 0.38$ K. Black dots are data, the red line represents the fit to Eq. (7) with $L_{\phi\infty} = 1.73 \mu\text{m}$.

that the limit imposed on τ_ϕ by τ_d is responsible for the saturation of L_ϕ at low T , where other decoherence mechanisms play a lesser role.

The effect of environmental decoherence (and equivalently of τ_d) on the effectively measured L_ϕ in a wire of length L can be quantified using expressions derived for the backscattered amplitude of a diffusing electron due to quantum interference^{18,39,40}. This approach bears a close similarity to the concept of escape rate, in that an electron diffusing from the wire into the wide 2D connecting regions at the endpoints of the wire, thereby escaping the quantum system, has a reduced probability of returning to its starting point and contributing to the quantum interference correction to conductance. Assuming perfect contacts between the wire and the wide 2D connecting regions at the endpoint, such that the backscattering amplitude for an electron diffusing into the environment is zero, one obtains^{19,39}:

$$L_\phi = L_{\phi\infty} \left(\coth \left(\frac{L}{L_{\phi\infty}} \right) - \frac{L_{\phi\infty}}{L} \right) \quad (7)$$

Here L_ϕ denotes the effectively measured coherence length in a wire of length L , and $L_{\phi\infty}$ denotes the coherence length in a wire with $L \rightarrow \infty$ for which interaction with the environment can be neglected. As depicted in Fig. 5, Eq. (7) can remarkably well reproduce the dependence of L_ϕ on L . The fit to the data yields $L_{\phi\infty} = 1.73 \mu\text{m}$ ($T = 0.38$ K).

V. CONCLUSIONS

Quantum phase coherence lengths L_ϕ as function of wire length L were obtained via a 1D WAL analysis, with ballistic transport corrections, for wires fabricated on a 2DES in a InGaAs/InAlAs heterostructure. It is observed that the measured L_ϕ increases with increasing L , effectively explained by the quantum decoherence effect introduced at the wire endpoints by environmental coupling. The decoherence effect of the coupling between the wire and the wide 2D connecting regions at the endpoints can be quantified by an expression for reduced coherent backscattering at the endpoints. The dependence of L_ϕ on T is consistent with the effects of quasi-elastic Nyquist scattering in both 1D and 2D regimes. The work underlines the influence of sample geometry and interactions with external neighboring regions on quantum decoherence in mesoscopic structures, with particular emphasis on decoherence in nanowires with relevance to the study of new quantum states of matter and with relevance in quantum technologies.

VI. ACKNOWLEDGMENTS

The work was supported by the U.S. Department of Energy, Office of Basic Energy Sciences, Division of Materials Sciences and Engineering under award DOE DE-FG02-08ER46532.

* heremans@vt.edu

¹ M. T. Deng, S. Vaitiekėnas, E. B. Hansen, J. Danon, M. Leijnse, K. Flensberg, J. Nygard, P. Krogstrup, and C. M. Marcus, *Science* **354**, 1557 (2016).

² S. Nakosai, J. C. Budich, Y. Tanaka, B. Trauzettel, and N. Nagaosa, *Phys. Rev. Lett.* **110**, 117002 (2013).

³ M. Ferrier, L. Angers, A. C. H. Rowe, S. Guéron, H. Bouchiat, C. Texier, G. Montambaux and D. Mailly, *Phys. Rev. Lett.* **93**, 246804 (2004).

⁴ B. Hackens, F. Delfosse, S. Faniel, C. Gustin, H. Boutry, X. Wallart, S. Bollaert, A. Cappy, and V. Bayot, *Phys. Rev. B* **66**, 241305(R) (2002).

⁵ J. J. Lin and J. P. Bird, *J. Phys.: Condens. Matter* **14**, R501 (2002).

⁶ S. L. Ren, J. J. Heremans, C. K. Gaspe, S. Vijayaragunathan, T. D. Mishima, and M. B. Santos, *J. Phys.: Condens. Matter* **25**, 435301 (2013).

⁷ J. P. Bird, A. P. Micolich, H. Linke, D. K. Ferry, R. Akis, Y. Ochiai, Y. Aoyagi, and T. Sugano, *J. Phys.: Condens. Matter* **10**, L55 (1988).

⁸ S. L. Ren, J. J. Heremans, S. Vijayaragunathan, T. D. Mishima, and M. B. Santos, *J. Phys.: Condens. Matter* **27**, 185801 (2015).

- ⁹ Y. Xie, C. Le Priol, and J. J. Heremans, *J. Phys.: Condens. Matter* **28**, 495003 (2016).
- ¹⁰ D. K. Ferry, A. M. Burke, R. Akis, R. Brunner, T. E. Day, R. Meisels, F. Kuchar, J. P. Bird, and B. R. Bennett, *Semicond. Sci. Technol.* **26**, 043001 (2011).
- ¹¹ M. Elhassan, J. P. Bird, R. Akis, D. K. Ferry, T. Ida, and K. Ishibashi, *J. Phys.: Condens. Matter* **17**, L351 (2005).
- ¹² B. Hackens, S. Faniel, C. Gustin, X. Wallart, S. Bollaert, A. Cappy, and V. Bayot, *Phys. Rev. Lett.* **94**, 146802 (2005).
- ¹³ J. P. Bird, A. P. Micolich, D. K. Ferry, R. Akis, Y. Ochiai, Y. Aoyagi, and T. Sugano, *Solid-State Electron.* **42**, 1281 (1998).
- ¹⁴ M. Katz, M. Ansmann, R. C. Bialczak, E. Lucero, R. McDermott, M. Neeley, M. Steffen, E. M. Weig, A. N. Cleland, J. M. Martinis, and A. N. Korotkov, *Science* **312**, 1498 (2006).
- ¹⁵ M. Schlosshauer, *Rev. Mod. Phys.* **76**, 1267 (2004).
- ¹⁶ D. Liang and X. P. A. Gao, *Nano Lett.* **12**, 3263 (2012).
- ¹⁷ P. Lehnen, Th. Schäpers, N. Kaluza, N. Thillozen and H. Hardtdegen, *Phys. Rev. B* **76**, 205307 (2007).
- ¹⁸ V. Chandrasekhar, D. E. Prober, and P. Santhanam, *Phys. Rev. Lett.* **61**, 2253 (1988).
- ¹⁹ R. L. Kallaher, J. J. Heremans, N. Goel, S. J. Chung, and M. B. Santos, *Phys. Rev. B* **81**, 035335 (2010).
- ²⁰ M. Rudolph and J. J. Heremans, *Phys. Rev. B* **83**, 205410 (2011).
- ²¹ R. L. Kallaher, J. J. Heremans, W. V. Roy, and G. Borghs, *Phys. Rev. B* **88**, 205407 (2013).
- ²² P. Rouleau, T. Choi, S. Riedi, T. Heinzl, I. Shorubalko, T. Ihn, and K. Ensslin, *Phys. Rev. B* **81**, 155449 (2010).
- ²³ D. Liang, J. Du, and X. P. A. Gao, *Phys. Rev. B* **81**, 153304 (2010).
- ²⁴ Th. Schäpers, V. A. Guzenk, M. G. Pala, U. Zülicke, M. Governale, J. Knobbe and H. Hardtdegen, *Phys. Rev. B* **74**, 081301(R) (2006).
- ²⁵ K. T. Lin, Y. Lin, C. C. Chi, and J. C. Chen, *Phys. Rev. B* **84**, 235404 (2011).
- ²⁶ C. Texier and G. Montambaux, *Phys. Rev. B* **72**, 115327 (2005).
- ²⁷ T. Ludwig and A. D. Mirlin, *Phys. Rev. B* **69**, 193306 (2004).
- ²⁸ C. Texier, P. Delplace, and G. Montambaux, *Phys. Rev. B* **80**, 205413 (2009).
- ²⁹ M. Ferrier, A. C. H. Rowe, S. Guéron, H. Bouchiat, C. Texier and G. Montambaux, *Phys. Rev. Lett.* **100**, 146802 (2008).
- ³⁰ C. Texier, *Phys. Rev. B* **76**, 153312 (2007).
- ³¹ A. G. Huibers, M. Switkes, C. M. Marcus, K. Campman, and A. C. Gossard, *Phys. Rev. Lett.* **81**, 200 (1998).
- ³² S. Faniel, B. Hackens, A. Vlad, L. Moldovan, C. Gustin, B. Habib, S. Melinte, M. Shayegan, and V. Bayot, *Phys. Rev. B* **75**, 193310 (2007).
- ³³ B. Hackens, S. Faniel, C. Gustin, X. Wallart, S. Bollaert, A. Cappy, and V. Bayot, *Physica E* **34**, 511 (2006).
- ³⁴ S. V. Iordanskii, Y. B. Lyanda-Geller, and G. E. Pikus, *Pis'ma Zh. Eksp. Teor. Fiz* **60**, 199 (1994) (*JETP Lett.* **60**, 206(1994)).
- ³⁵ G. Bergmann, *Int. J. Mod. Phys. B* **24**, 2015 (2010).
- ³⁶ S. McPhail, C. E. Yasin, A. R. Hamilton, M. Y. Simmons, E. H. Linfield, M. Pepper, and D. A. Ritchie, *Phys. Rev. B* **70**, 245311 (2004).
- ³⁷ V. Deo, Y. Zhang, V. Soghomonian, and J. J. Heremans, *Sci. Rep.* **5**, 9487 (2015).
- ³⁸ G. Bergmann, *Phys. Rep.* **107**, 1 (1984).
- ³⁹ B. Doucot and R. Rammal, *J. Physique* **47**, 973 (1986).
- ⁴⁰ E. Akkermans and G. Montambaux, *Mesoscopic physics of electrons and photons* (Cambridge, 2007).
- ⁴¹ M. Treiber, C. Texier, O. M. Yevtushenko, J. von Delft, and I. V. Lerner, *Phys. Rev. B* **84**, 054204 (2011).
- ⁴² K. K. Choi, D. C. Tsui, and K. Alavi, *Phys. Rev. B* **36**, 7751 (1987).
- ⁴³ T. Matsuoka, E. Kobayashi, K. Taniguchi, C. Hamaguchi, and S. Sasa, *Jpn. J. Appl. Phys.* **29**, 2017 (1990).
- ⁴⁴ E. Diez, Y. P. Chen, S. Avesque, M. Hilke, E. Peled, D. Shahar, J. M. Cerveró, D. L. Sivco and A. Y. Cho, *Appl. Phys. Lett.* **88**, 052107 (2006).
- ⁴⁵ J. C. Licini, G. J. Dolan, and D. J. Bishop, *Phys. Rev. Lett.* **54**, 1585 (1985).
- ⁴⁶ J. J. Heremans, R. L. Kallaher, M. Rudolph, M. Santos, W. V. Roy, and G. Borghs, *Proc. of SPIE* **9167**, 91670D (2014).
- ⁴⁷ S. Kettemann, *Phys. Rev. Lett.* **98**, 176808 (2007).
- ⁴⁸ S. Hikami, A. I. Larkin, and Y. Nagaoka, *Prog. Theor. Phys.* **63**, 707 (1980).
- ⁴⁹ G. J. Dolan, J. C. Licini, and D. J. Bishop, *Phys. Rev. Lett.* **56**, 1493 (1986).
- ⁵⁰ A. Zduniak, M. I. Dyakonov, and W. Knap, *Phys. Rev. B* **56**, 1996 (1997).
- ⁵¹ C. W. J. Beenakker and H. van Houten, *Phys. Rev. B* **38**, 3232 (1988).
- ⁵² Y. Kunihashi, M. Kohda, and J. Nitta, *Phys. Rev. Lett.* **102**, 226601 (2009).
- ⁵³ J. P. Bird, K. Ishibashi, D. K. Ferry, Y. Ochiai, Y. Aoyagi, and T. Sugano, *Phys. Rev. B* **51**, 18037 (1995).
- ⁵⁴ R. A. Jalabert, H. U. Baranger, and A. D. Stone, *Phys. Rev. Lett.* **65**, 2442 (1990).
- ⁵⁵ D. P. Pivin, A. Andresen, J. P. Bird, and D. K. Ferry, *Phys. Rev. Lett.* **82**, 4687 (1999).
- ⁵⁶ P. Mohanty and R. A. Webb, *Phys. Rev. B* **55**, R13452 (1997).
- ⁵⁷ P. Mohanty, E. M. Q. Jariwala, and R. A. Webb, *Phys. Rev. Lett.* **78**, 3366 (1997).
- ⁵⁸ T. Hiramoto, K. Hirakawa, Y. Iye, and T. Ikoma, *Appl. Phys. Lett.* **54**, 2103 (1989).
- ⁵⁹ D. Natelson, R. L. Willett, K. W. West, and L. N. Pfeiffer, *Phys. Rev. Lett.* **86**, 1821 (2001).
- ⁶⁰ K. H. Gao, G. Yu, Y. M. Zhou, W. Z. Zhou, T. Lin, J. H. Chu, N. Dai, D. G. Austing, Y. Gu, and Y. G. Zhang, *Phys. Rev. B* **79**, 085310 (2009).

Chapter 5

Effect of two-dimensional parity symmetry breaking in Aharonov-Bohm interference phenomena

This paper was previously published as: Yuantao Xie, J. J. Heremans and M. B. Santos, “Effect of two dimensional parity symmetry breaking in Aharonov-Bohm interference phenomena”, *Integrated Ferroelectrics* **174**, 8 (2016). Reproduced with permission.

Effect of two-dimensional parity symmetry breaking in Aharonov-Bohm interference phenomena

Yuantao Xie^a, J. J. Heremans^a, and M. B. Santos^b

^aDepartment of Physics, Virginia Tech, Blacksburg, VA, USA; ^bHomer L. Dodge Department of Physics and Astronomy, University of Oklahoma, Norman, OK, USA

ABSTRACT

The quantum-mechanical dephasing effect of a two-dimensional parity symmetry breaking is demonstrated in a solid-state quantum-coherent mesoscopic ring interferometer. The interferometer, fabricated on an InGaAs/InAlAs heterostructure, shows Aharonov-Bohm oscillations under magnetic fields at low temperatures. Under asymmetric bias voltage on side-gates, a weakening of the Aharonov-Bohm oscillations is observed. The weakening corresponds to an effective dephasing under two-dimensional parity symmetry breaking by the applied electric field, and is interpreted as a counterpart to the weakening observed under time-reversal symmetry breaking by a magnetic field.

KEYWORDS

Aharonov-Bohm phase; parity symmetry; quantum coherence; mesoscopic physics; InGaAs; interferometer

The quantum-mechanical effects of broken symmetries, including time-reversal symmetry and parity symmetry, can be studied experimentally via the resulting quantum dephasing in mesoscopic solid-state systems. In the present work, Aharonov-Bohm (AB) oscillations [1–5] are used to study dephasing under a broken parity symmetry induced in the respective arms of a quantum ring interferometer. The oscillations appear in the low-temperature electrical conductance of the interferometer structure versus applied magnetic field B . Symmetries play an important role in solid-state phenomena, among others in the categorization of ferroic orders (ferroelectric, ferromagnetic, multiferroic, and others) [6]. The work below focuses on the foundational nature and geometrical aspects of mirror symmetry breaking in a quantum mechanically coherent entity. Previously, the effects of time-reversal symmetry breaking by magnetic fields were studied in a similar structure, and the geometrical aspects, described by a magnetic length, of time-reversal symmetry breaking were emphasized [7]. The mirror symmetry manipulated in the present work is a two-dimensional parity symmetry, and its study in quantum phenomena is justified due to the role CPT (charge conjugation-parity-time) symmetry assumes in quantum physics.

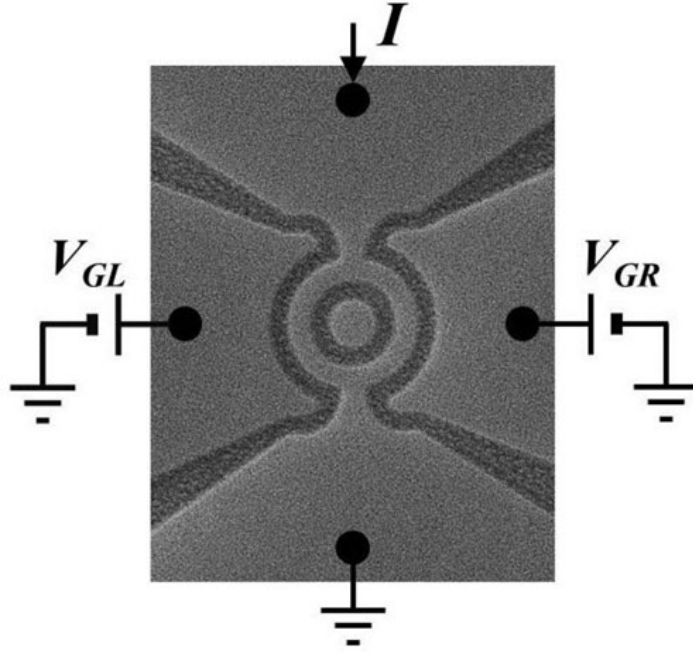


Figure 1. Scanning electron micrograph of the side-gated ring interferometer, with schematic measurement setup. Conducting areas are lighter in shade, etched non-conducting trenches darker. The ring's average radius is 650 nm.

Low-temperature mesoscopic quantum electronic transport on a narrow-gap semiconductor InGaAs quantum well is used, where the interferometer length scale is comparable to the spin coherence and quantum phase coherence lengths in the material. Hence phenomena relying on a retention of quantum coherence can be observed (for an example, see [8]). AB oscillations are evidence of the nonlocal quantum nature of mesoscopic conductance phenomena, and are caused by quantum interference between partial waves traveling in spatially separate interferometer arms when a magnetic flux φ threads between the two arms [2,7]. The two partial waves accumulate a total relative AB phase of 2π if they traverse separate trajectories enclosing a magnetic flux quantum h/e (where $h = 2\pi\hbar$ with \hbar the Planck constant and e the electron charge). Due to alternatively constructive and destructive quantum interference, the transmittance and conductance of the interferometer then oscillate in B with a periodicity corresponding to $\varphi = h/e$.

Figure 1 shows a scanning electron micrograph of the ring interferometer studied in this work. Conducting areas, including the ring, are defined by lighter-colored areas, whereas darker areas are depleted of carriers (the innermost lighter-colored disc has no function). The ring has a lithographic average radius $r = 650$ nm, and the arms have lithographic width 300 nm (the conducting width is narrower due to edge depletion [2]). A variable uniform B is applied over the ring area, while the resistance R of the ring is measured using low-frequency ac lock-in four-terminal measurements. Figure 1 indicates the direction of the ac excitation current through the ring, kept at 20 nA to prevent carrier heating. The expected AB oscillation period in B , given by $(h/e)/(\pi r^2)$, is 3.1 mT for the given r . Figure 1 also shows two side-gates

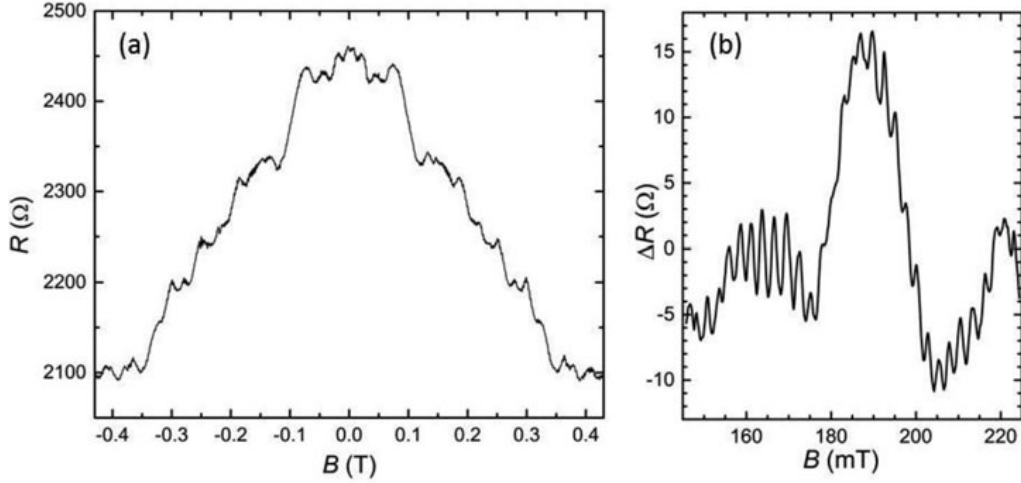


Figure 2. (a) Resistance R of the ring measured vs B normal to the surface, at $T = 0.38$ K and $V_{GL} = V_{GR} = 0$. Aharonov-Bohm oscillations (amplitude ~ 10 Ω not fully resolved in this wide-range figure) appear, modulated in amplitude, on top of a resistance background and universal conductance fluctuations. (b) High-resolution zoom-in on the region $145 \text{ mT} < B < 225 \text{ mT}$, showing R with the magnetoresistance background removed (ΔR) to emphasize the Aharonov-Bohm oscillations, with measured periodicity 2.9 mT.

[9,10] defined by the lighter-colored areas flanking the ring, and separated from the conducting arms by an insulating trench of width 250 nm. To each side-gate a voltage bias can be applied referred to the ring potential (or ground), V_{GL} or V_{GR} . The side-gate voltages V_{GL} and V_{GR} create an electric field (with dominant component in the plane of the ring), penetrating respectively the left or right interferometer arm. The difference in electric fields over the left and right interferometer arms breaks the mirror symmetry or two-dimensional parity symmetry of the structure. As an example, Fig. 2(a) shows the measured resistance of the ring ($V_{GL} = V_{GR} = 0$) at a temperature $T = 0.38$ K, as function of B . On top of the classical ring resistance of 2450Ω ($B = 0$) and of a long-period magnetoresistance structure due to universal conductance fluctuations [11], pronounced AB oscillations appear. The oscillations, appearing *e.g.* strongly at ± 0.05 T, ± 0.16 T, ± 0.24 T, ± 0.41 T, *etc.*, are non-uniform and modulated in amplitude as expected [2,12–14]. Figure 2(b) shows a zoom-in at higher-resolution, where a magnetoresistance background has been removed to accentuate the AB oscillations. The AB periodicity in Figs. 2(a) and 2(b) is 2.9 mT, in excellent agreement with the predicted periodicity of 3.1 mT.

The interferometer in Fig. 1, yielding a periodicity of h/e due to the AB phase as seen in Fig. 2, is a Mach–Zehnder interferometer, relying on spatially separate interferometer arms [7]. A spatial asymmetry between the two arms, either intentional or originating in fabrication and materials imperfections, can give rise to an additional phase shift between the two partial waves, possibly leading to dephasing and a decrease in the oscillations’ visibility. It is readily seen that in the extreme asymmetric case of elimination of one of the arms, or for a side-gate voltage sufficiently negative to deplete one of the arms of electrons, the oscillations will disappear.

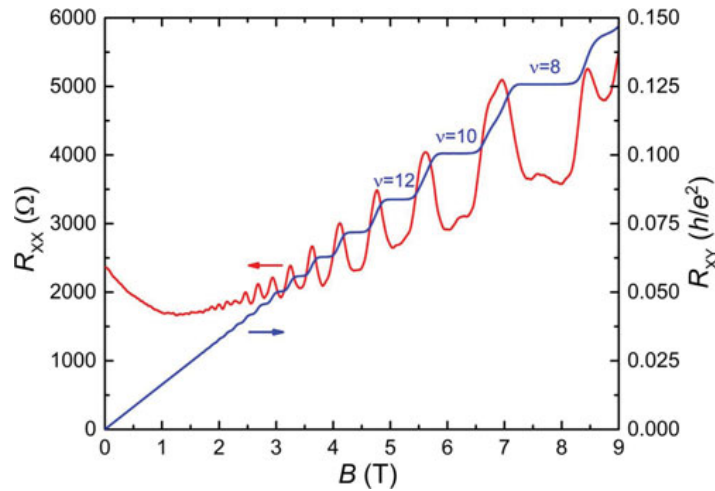


Figure 3. Left axis: resistance R ($= R_{XX}$) of the ring vs B up to the integer quantum Hall regime, at $T = 0.38$ K and $V_{GL} = V_{GR} = 0$. Shubnikov-de Haas oscillations appear for $B < \sim 3$ T, developing in integer quantum Hall features. Right axis: Hall resistance R_{XY} over unpatterned sample regions, showing integer quantum Hall plateaux, labeled with the Landau level filling factor ν .

The AB ring was fabricated on an $\text{In}_{0.64}\text{Ga}_{0.36}\text{As}/\text{In}_{0.45}\text{Al}_{0.55}\text{As}$ heterostructure by electron beam lithography and reactive ion etching (ICP-RIE). Electrons in the heterostructure form a two-dimensional electron system (2DES) located in a 10 nm wide $\text{In}_{0.64}\text{Ga}_{0.36}\text{As}$ quantum well at a depth 50 nm from the surface. The 2DES density $N_S = 1.48 \times 10^{16} \text{ m}^{-2}$ (resulting in a Fermi wavelength of 21 nm) and the mobility is $7.8 \text{ m}^2/\text{Vs}$ at 0.4 K, yielding in a 2DES resistivity $54 \text{ } \Omega/\square$. With non-parabolicity in the conduction band, the mean free path amounts to $3.2 \text{ } \mu\text{m}$, signifying the interferometer operates in the ballistic regime. The quality of the heterostructure is evident from Fig. 3, which shows the Hall resistance R_{XY} and the longitudinal resistance R_{XX} as measured over the ring ($T = 0.38$ K) up to high B . The R_{XY} trace shows integer quantum Hall plateaux, up to Landau level filling factor $\nu = 8$. The R_{XX} trace also shows integer quantum Hall effect features at higher B . Yet minima do not reach $R_{XX} = 0$ since R_{XX} was obtained over the mesoscopic ring in which opposite edge states communicate and hence backscatter [15]. At lower B the R_{XX} trace contains Shubnikov-de Haas oscillations. The value for N_S was obtained from both Shubnikov-de Haas and Hall data.

Figure 4 show the ring resistance R vs B obtained under asymmetric side-gate biasing, for $-75 \text{ mT} < B < 75 \text{ mT}$. AB oscillations of amplitude $\sim 4 \dots 10 \text{ } \Omega$, on a background of $\sim 2800 \dots 3300 \text{ } \Omega$, are clearly visible in specific regions of B (amplitude modulations are also present, as discussed in [2]). In these experiments, V_{GL} is varied from 1.8 V to -1.2 V, while $V_{GR} = 0$. The values $R(B = 0)$ in Fig. 4 demonstrates that the ring becomes more resistive at more negative V_{GL} as expected from a depletion of electrons in the left arm at more negative side-gate voltages. The background magnetoresistance, partially due to universal conductance fluctuations, also varies with V_{GL} since the mesoscopic representation of the sample changes for different V_{GL} . A slight hysteresis in both V_{GL} and V_{GR} occurs as well, but has no impact on the AB oscillation data. In Fig. 4 overall strongest AB oscillations in R occur

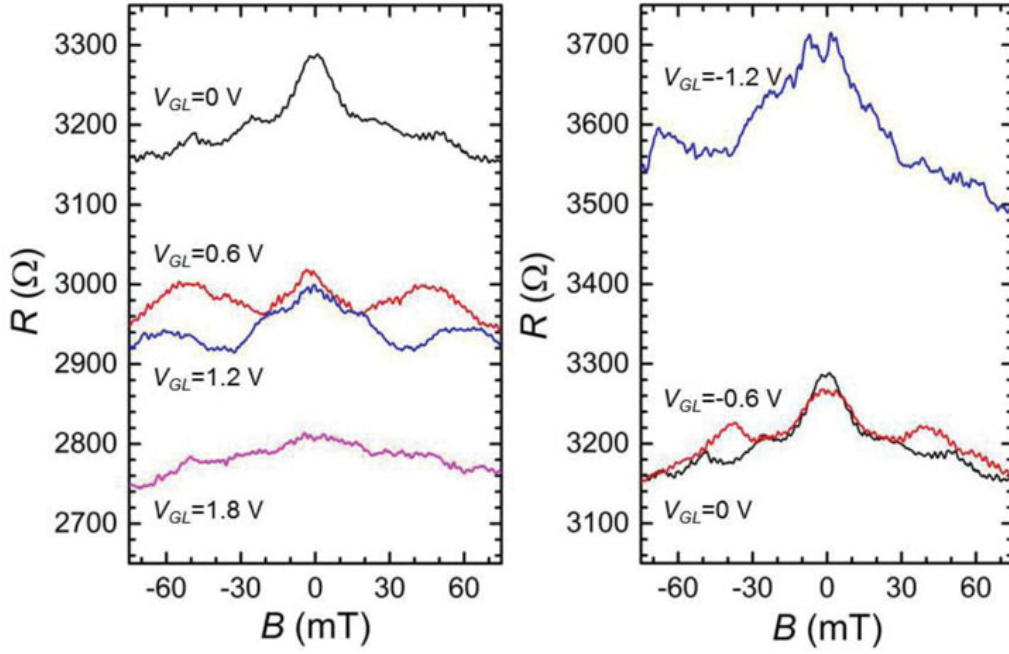


Figure 4. Resistance R of the ring measured vs B at $T = 0.38$ K under asymmetric side-gate bias, with V_{GL} as indicated and $V_{GR} = 0$. The left panel shows data for $V_{GL} \geq 0$, the right panel for $V_{GL} \leq 0$. Aharonov-Bohm oscillations are visible in all traces.

for $V_{GL} = V_{GR} = 0$, the mirror-symmetric case. For $V_{GL} = 0.6$ V with $V_{GR} = 0$ the oscillations are slightly diminished, whereas for $V_{GL} = 1.8$ V with $V_{GR} = 0$ the oscillations are clearly diminished. For $V_{GL} = -1.2$ V with $V_{GR} = 0$ the oscillations have weakened significantly. **Figure 5** contains a quantification of the observations relating to **Fig. 4**, with the maximum observed oscillation amplitude over -75 mT $< B < 75$ mT, plotted vs V_{GL} ($V_{GR} = 0$). The plotted amplitude forms an approximate measure of the strength of the quantum interference effect in the presence of the inevitable amplitude modulation. The strongest oscillations occur for $V_{GL} =$

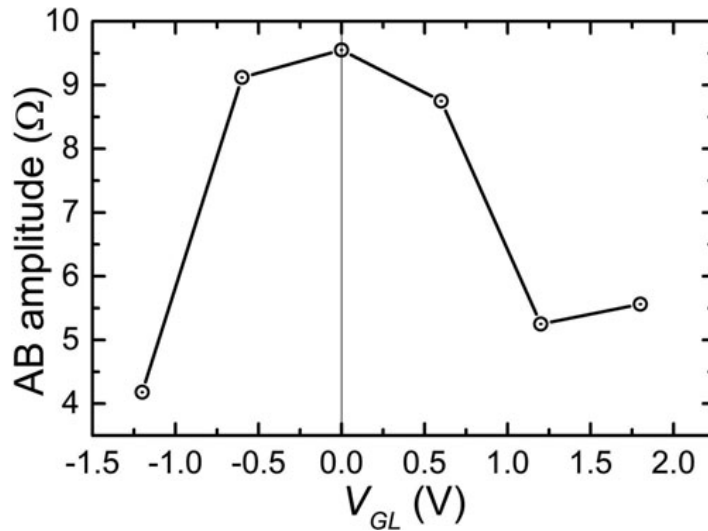


Figure 5. The maximum amplitude of Aharonov-Bohm oscillations observed in the data of **Fig. 4**, as function of V_{GL} (with $V_{GR} = 0$).

$V_{GR} = 0$, with visibility falling for both $V_{GL} < 0$ and $V_{GL} > 0$. The fall-off is stronger for $V_{GL} < 0$, likely due to secondary effects of electron depletion in the left arm for $V_{GL} < 0$. It is the maximum in oscillation strength observed for $V_{GL} = V_{GR} = 0$, the symmetric case, which forms the main result of the study.

The breaking of the two-dimensional parity symmetry hence results in a fading of the quantum interference signal, and thus effectively in a dephasing effect for the system. The Mach–Zehnder interferometer used in the experiment is specifically sensitive to spatial asymmetry, relying on spatially separate paths. The Mach–Zehnder interferometer can be contrasted with interferometer arrays wherein the signal arises from time-reversed paths, and such arrays hence show a sensitivity to time-reversal symmetry breaking, *e.g.* originating in B penetrating the arms [7]. The present experiment constitutes a dual to such interferometric measurements of time-reversal symmetry breaking, as in the present experiment an electric field breaks two-dimensional parity symmetry in an interferometer specifically sensitive to parity symmetry. The experiment shows that, in analogy to the effect of time-reversal symmetry breaking by a magnetic field, a breaking of parity symmetry by an electric field leads to an effective quantum dephasing.

In conclusion, a mesoscopic ring Mach-Zehnder interferometer with side-gates was fabricated on an InGaAs/InAlAs heterostructure. Aharonov-Bohm quantum interference oscillations in the interferometer are measured at 0.38 K under applied magnetic fields, to study the dephasing effect of spatial symmetry breaking over the ring. The side-gates allow application of transverse electric fields, and under asymmetric bias they allow a breaking of the mirror or two-dimensional parity symmetry of the device. It is observed that indeed the amplitude of the Aharonov-Bohm oscillations weakens under asymmetric side-gate bias, confirming the effective dephasing effect of a breaking of two-dimensional parity symmetry. The experiments form a dual counterpart to previous experiments studying the dephasing effects of time-reversal symmetry breaking and substantiate the non-trivial consequences of symmetry breaking in quantum-coherent structures.

Acknowledgments

The work was supported by the U.S. Department of Energy, Office of Basic Energy Sciences, Division of Materials Sciences and Engineering under award DOE DE-FG02-08ER46532 (JJH: experiment design, sample fabrication, and measurement), and by the National Science Foundation under award NSF DMR-1207537 (MBS: heterostructure growth).

References

1. Y. Aharonov, and D. Bohm “Significance of electromagnetic potentials in quantum theory”. *Phys. Rev.* **115**, 485–491 (1959).
2. S. L. Ren, J. J. Heremans, C. K. Gaspe, S. Vijayaragunathan, T. D. Mishima, and M. B. Santos “Aharonov–Bohm oscillations, quantum decoherence and amplitude modulation in mesoscopic InGaAs/InAlAs rings”. *J. Phys.: Cond. Mat.* **25**, 435301 (7pp) (2013).

3. S. Washburn, and R. A. Webb "Aharonov-Bohm effect in normal metal, quantum coherence and transport". *Adv. Phys.* **35**, 375–422 (1986).
4. S. Oliaru, and I. I. Popescu "The quantum effects of electromagnetic fluxes". *Rev. Mod. Phys.* **57**, 339–436 (1985).
5. A. G. Aronov, and Yu. V. Sharvin "Magnetic flux effects in disordered conductors". *Rev. Mod. Phys.* **59**, 755–779 (1987).
6. S.-W. Cheong, and M. Mostovoy "Multiferroics: a magnetic twist for ferroelectricity". *Nat. Mater.* **6**, 13–20 (2007).
7. S. L. Ren, J. J. Heremans, C. K. Gaspe, S. Vijayaragunathan, T. D. Mishima, and M. B. Santos "Determination of time-reversal symmetry breaking lengths in an InGaAs Sagnac interferometer array". *J. Phys.: Cond. Mat.* **27**, 185801 (7pp) (2015).
8. C. Texier, P. Delplace, and G. Montambaux "Quantum oscillations and decoherence due to electron-electron interaction in metallic networks and hollow cylinders". *Phys. Rev. B* **80**, 205413 (1–32) (2009).
9. M. Kohda, S. Nakamura, Y. Nishihara, K. Kobayashi, T. Ono, J. Ohe, Y. Tokura, T. Mineno, and J. Nitta "Spin-orbit induced electronic spin separation in semiconductor nanostructures". *Nat. Commun.* **3**, 1082 (8pp) (2012).
10. L. P. Rokhinson, L. N. Pfeiffer, and K. W. West "Spontaneous spin polarization in quantum point contacts". *Phys. Rev. Lett.* **96**, 156602 (1–4) (2006).
11. M. Rudolph, and J. J. Heremans "Spin-orbit interaction and phase coherence in lithographically defined bismuth wires". *Phys. Rev. B* **83**, 205410 (1–6) (2011).
12. M. A. Castellanos-Beltran, D. Q. Ngo, W. E. Shanks, A. B. Jayich, and J. G. E. Harris "Measurement of the full distribution of persistent current in normal-metal rings". *Phys. Rev. Lett.* **110**, 156801 (1–5) (2013).
13. L. C. Mur, C. J. P. M. Harmans, and W. G. van der Wiel "Competition between h/e and $h/2e$ oscillations in a semiconductor Aharonov-Bohm interferometer". *New J. Phys.* **10**, 073031 (16pp) (2008).
14. F. Nichele, Y. Komijani, S. Hennel, C. Gerl, W. Wegscheider, D. Reuter, A. D. Wieck, T. Ihn, and K. Ensslin "Aharonov-Bohm rings with strong spin-orbit interaction: the role of sample-specific properties". *New J. Phys.* **15**, 033029 (15pp) (2013).
15. V. J. Goldman, J. Liu, and A. Zaslavsky "Electron tunneling spectroscopy of a quantum antidot in the integer quantum Hall regime". *Phys. Rev. B* **77**, 115328 (1–10) (2008).

This paper was previously published as:

Yuantao Xie, J. J. Heremans and M. B. Santos, "Effect of two-dimensional parity symmetry breaking in Aharonov-Bohm interference phenomena", *Integrated Ferroelectrics* **174**, 8 (2016).

Chapter 6

Mapping electromagnetic dualities via quantum decoherence measurements in 2D materials

This paper was previously published as: J. J. Heremans, Yuantao Xie, S. L. Ren, C. Le Priol and M. B. Santos, “Mapping electromagnetic dualities via quantum decoherence measurements in 2D materials”, *Proceedings of SPIE* **9932**, 993207-1 (2016). Reproduced with permission.

Mapping electromagnetic dualities via quantum decoherence measurements in 2D materials

J. J. Heremans^a, Yuantao Xie^a, S. L. Ren^a, C. Le Priol^b, and M. B. Santos^c

^aPhysics Department, Virginia Tech, Blacksburg, VA 24061, USA

^bPhysics Department, Ecole Polytechnique, 91128 Palaiseau, France

^cHomer L. Dodge Department of Physics and Astronomy, University of Oklahoma, Norman, OK 73019, USA

ABSTRACT

The quantification of quantum phase coherence can reveal several properties of charge carriers in systems of given dimensionality, illuminating mechanisms leading to quantum decoherence due to inelastic scattering events, to decoherence mechanisms due to device geometry, and to dephasing due to geometrical phases from applied fields. Examples of several effects are presented. Quantum phase coherence lengths were measured in mesoscopic geometries by quantum transport methods including universal conductance fluctuations, weak-localization, and quantum interferometry. The geometries were fabricated from two-dimensional starting materials. In wires of materials with strong spin-orbit interaction, we show that spin decoherence due to spin-orbit interaction and dephasing due to applied magnetic fields show an electromagnetic duality. We show that dephasing due to applied magnetic fields can be expressed in terms of a magnetic length quantifying time-reversal symmetry breaking. In wires, the main orbital quantum decoherence mechanism related to the wire length appears as environmental coupling decoherence, with longer wires showing asymptotically longer phase coherence lengths. For mesoscopic stadia, the geometry plays an additional role, inducing stadium-wire coupling decoherence.

Keywords: quantum coherence, mesoscopic physics, spin-orbit interaction, quantum wire, weak-localization, universal conductance fluctuations

Address all correspondence to: Jean J. Heremans, Virginia Polytechnic Institute and State University, Department of Physics, 850 West Campus Drive, Blacksburg, VA 24061, Tel: 1 540-231-4604; E-mail:heremans@vt.edu

1. INTRODUCTION

The rise of quantum information processing and quantum technologies lend new importance to the understanding of quantum phase decoherence. Important parameters in this respect are the electrons' quantum phase coherence length L_ϕ (defined as the length scale over which quantum coherence is maintained when the system is considered spinless), and the spin coherence length L_S . In mesoscopic systems, the quantum phases of carrier states can be randomized by inelastic or quasi-elastic processes dependent on temperature T , such as electron-phonon and electron-electron scattering¹⁻³ and energy

level broadening exceeding the Thouless energy.⁴ Decoherence can also be caused by mechanisms without T -dependence, such as environmental coupling decoherence^{5,6} due to connecting quantum systems to classical environments. Environmental coupling decoherence is often expressed using an escape rate $1/\tau_d$, where the dwell time τ_d is proportional to system size and limits the quantum phase coherence time τ_ϕ at low T .⁷ Here $L_\phi = \sqrt{D\tau_\phi}$, where D denotes the carrier diffusion coefficient. In this work we describe how in addition to decoherence mechanisms, dephasing by geometrical quantum phases can also reduce apparent quantum coherence (decoherence is irreversible, while dephasing is reversible⁸). The two contributions blend in actual experiments. Dephasing by geometrical quantum phases contains information about fundamental physics phenomena. To extract this information however, it is necessary to quantify sources of decoherence. In this work, mesoscopic wires were studied, fabricated on InGaAs/InAlAs and InSb/InAlSb heterostructures harboring two-dimensional electron systems (2DESs). Also studied were wires fabricated on thin film Bi and mesoscopic stadia with side-wires fabricated on InGaAs/InAlAs heterostructures. Few previous investigations studied the effects of device-device coupling on decoherence between devices of different geometries, and here we describe a notable influence of *stadium-wire* coupling in the stadia with side-wires. The experiments use quantum interference effects in electronic transport, namely weak-antilocalization (WAL)^{9–13} and universal conductance fluctuations (UCFs),^{1,14–16} to measure L_ϕ . Since in the wires WAL dominates over UCFs, and *vv* for stadia, WAL is used to extract L_ϕ in the wires and UCFs are used in the stadia. Measurements were obtained by four-contact techniques under low constant-current excitation in a ³He cryostat, over variable T from 0.38 K to 5.0 K. The low T leads to sufficiently long L_ϕ to study quantum interference phenomena,^{4,17} and brings out decoherence mechanisms weakly dependent on T .

2. EXPERIMENTAL ASPECTS

The mesoscopic geometries studied in this work consisted of wires and stadia (wide 2D quantum dots). Parent materials to fabricate the mesoscopic devices were Bi(111) thin films (rhombohedral notation),^{16,18} an InSb/In_{0.85}Al_{0.15}Sb heterostructure,¹⁹ a high-mobility In_{0.64}Ga_{0.36}As/In_{0.45}Al_{0.55}As heterostructure,^{4,17} and an In_{0.53}Ga_{0.47}As/In_{0.52}Al_{0.48}As lattice-matched bottom-doped heterostructure.²⁰ The devices were defined by electron-beam lithography and wet and reactive ion etching. Figure 1 depicts scanning electron micrographs of example geometries defined on the In_{0.53}Ga_{0.47}As/In_{0.52}Al_{0.48}As heterostructure, and conveys the dimensions of the devices as discussed below. Bi(111) thin films were thermally evaporated from 99.999% Bi sources on a SiO₂ (oxidized Si(001)) substrate,^{16,18} to a thickness of 75 nm. The films show an orientation with the trigonal axis perpendicular to the substrate with grains of size 200-500 nm randomly oriented. The film surface is hence the trigonal face (Bi(111) in rhombohedral notation). The surface carriers on Bi(111)²¹ dominate the transport properties with particularly a central electron pocket (along the trigonal axis) with effective mass $\sim 0.5 m_e$ with m_e the free electron mass) determining the quantum transport measurements. As expected for high-quality semimetallic Bi, multicarrier fits to the magnetotransport data show compensated electron and hole densities $\sim 2 \times 10^{24} \text{ m}^{-3}$ and show mobilities $\sim 0.1 \text{ m}^2/\text{Vs}$. Wires on Bi had a length $L = 16 \mu\text{m}$ and varying widths W . The In_{0.85}Al_{0.15}Sb/InSb/In_{0.85}Al_{0.15}Sb heterostructure, grown by molecular beam epitaxy (MBE) on (001) GaAs substrate, housed an InSb quantum well of thickness 25 nm¹⁹ in which the 2DES is located. At $T = 0.39 \text{ K}$ the unpatterned 2DES had areal electron density $N_S = 5.2 \times 10^{15} \text{ m}^{-2}$ with mobility $\mu = 9.7 \text{ m}^2/\text{Vs}$, yielding a mean-free-path $\ell_e \approx 3.3 \mu\text{m}$. Here $\ell_e = v_F \tau_e$ where τ_e is the momentum scattering time and v_F the Fermi velocity. Wires on the InSb 2DES had $L = 24 \mu\text{m}$ and varying W . The high-mobility In_{0.64}Ga_{0.36}As/In_{0.45}Al_{0.55}As heterostructure^{4,17} was obtained by MBE

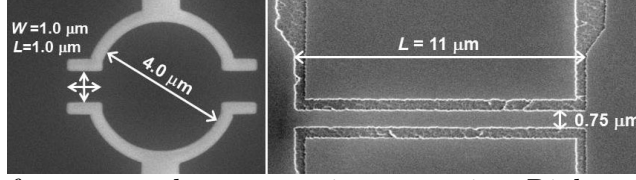


Figure 1: Micrographs of two example mesoscopic geometries. Right panel: an example stadium sample with side-wires with $W = 1 \mu\text{m}$ and $L = 1 \mu\text{m}$. Etched trenches, which form barriers confining the electrons, appear as lighter regions. Left panel: two U-shaped trenches define a wire between them, here with length $L = 11 \mu\text{m}$

on (001) GaAs substrate, and housed an $\text{In}_{0.64}\text{Ga}_{0.36}\text{As}$ quantum well of thickness 10 nm, with at $T = 0.39$ K unpatterned 2DES density $N_S = 1.1 \times 10^{16} \text{ m}^{-2}$ with $\mu = 4.7 \text{ m}^2/\text{Vs}$ and $\ell_e \approx 1.5 \mu\text{m}$. Wires on the InSb 2DES had $L = 24 \mu\text{m}$ and varying W . The $\text{In}_{0.53}\text{Ga}_{0.47}\text{As}/\text{In}_{0.52}\text{Al}_{0.48}\text{As}$ heterostructure²⁰ was bottom-doped to obtain asymmetry in the quantum well confinement potential and hence strong spin-orbit interaction (SOI). The heterostructure was grown by MBE on InP(001) substrate, with a 10 nm wide $\text{In}_{0.53}\text{Ga}_{0.47}\text{As}$ quantum well. The 2DES showed $N_S = 2.02 \times 10^{16} \text{ m}^{-2}$ and $\mu = 1.49 \text{ m}^2/(\text{Vs})$ at $T = 0.38$ K, with $\ell_e = 0.77 \mu\text{m}$. Wires with $L = 2.0 \mu\text{m}$, $4.0 \mu\text{m}$, $6.0 \mu\text{m}$ and $11.0 \mu\text{m}$ and with lithographic width $0.75 \mu\text{m}$, as well as stadia with constant inner diameter $4.0 \mu\text{m}$, and with varying wire-like necks (for dimensions, *cf* Fig. 1) were patterned on this heterostructure. For all materials, transport properties stayed appreciably constant over the range of T in the measurements. Starting from the 2D parent materials, the wires on the heterostructures operate in the quasi-one-dimensional (Q1D) regime, meaning that the Fermi wavelengths $\lambda_F \ll W$ such that quantization in transverse subbands can be neglected, and that both $L_\phi > W$ and $\ell_e > W$.

3. MODELS FOR QUANTUM TRANSPORT

The data used to extract values for L_ϕ consists of device conductance G as function of magnetic field B applied normally to the 2D material. The data display the characteristic shape of WAL, where the magnetoconductance $G(B)$ drops sharply as $|B|$ is increased from zero, and UCFs¹⁶ are also prominent. An example of measured $G(B)$ vs B with strong UCFs and the characteristic WAL negative magnetoconductance at low B , is contained in Fig. 2 for a stadium with side-wires of dimensions $W = 1.4 \mu\text{m}$ and $L = 1.0 \mu\text{m}$ (Fig. 1). We describe the models fitted to the measured $G(B)$ to extract values of L_S (by WAL analysis) and L_ϕ (by WAL or UCF analysis). The parent materials possess substantial SOI and are non-magnetic, and hence L_S is here limited by spin decoherence originating in SOI. WAL results from quantum interference of time-reversed trajectories of a diffusing electron returning to its starting point. Under SOI, singlet and triplet contributions arise from the pairs of time-reversed trajectories. In 1D, the quantum correction to conductance $\delta G(B)$ due to each contribution scales as an effective coherence length and the combination of the lengths amounts to the 1D WAL correction^{9, 10, 22, 23}

$$\delta G(B) = -\frac{1}{2} \frac{e^2}{\pi \hbar} \frac{1}{L} (L_{1,1} + L_{1,-1} + L_{1,0} - L_{0,0}) \quad (1)$$

where $L_{0,0} = (L_\phi^{-2} + L_B^{-2})^{-\frac{1}{2}}$ is the effective length for the singlet, and $L_{1,\pm 1} = (L_\phi^{-2} + L_S^{-2} + L_B^{-2})^{-\frac{1}{2}}$ and $L_{1,0} = (L_\phi^{-2} + 2L_S^{-2} + L_B^{-2})^{-\frac{1}{2}}$ are effective lengths for the triplets. In laterally unconfined 2D

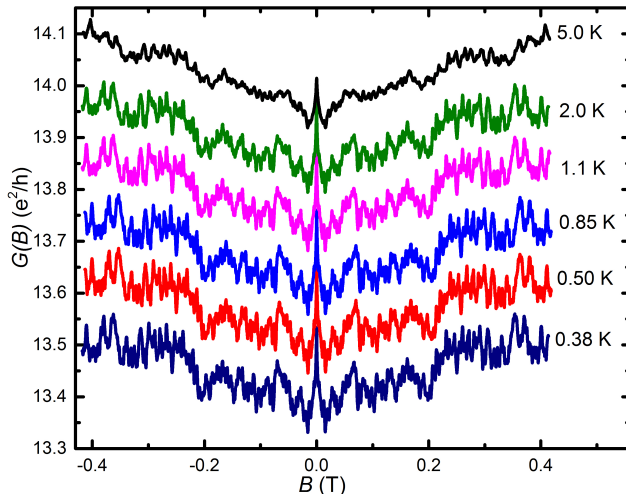


Figure 2: Magnetoconductance data $G(B)$ vs B for a stadium with side-wires with $W = 1.4 \mu\text{m}$ and $L = 1.0 \mu\text{m}$, plotted over variable T . The amplitude of the UCFs decreases with increasing T due to the expected decrease in L_ϕ with increasing T . The dominant UCF signature was used in the stadia samples to obtain L_ϕ .

or 3D systems, the magnetic length $L_B = l_m \equiv \sqrt{\hbar/eB}$. In narrow wires in the ballistic transport regime with $\ell_e \gtrsim 0.6W$ and at low B limited by $l_m > \sqrt{W\ell_e}$, an expression accounting for flux cancellation^{17,24} is used, $L_B = l_m \sqrt{C_1 l_m^2 \ell_e / W^3}$. In the ballistic regime and at intermediate B such that $W < l_m < \sqrt{W\ell_e}$, the crossover expression^{9,10,17,24} is used, $L_B = l_m \sqrt{C_1 l_m^2 \ell_e / W^3 + C_2 \ell_e^2 / W^2}$. Here $C_1 = 4.75$ and $C_2 = 2.4$ for specular boundary scattering adopted in the samples here due to the existence of depletion layers at edges.^{9,10,24}

UCFs in $G(B)$ are analyzed using a correlation function to bring out quantum coherence effects dependent on L_ϕ . The correlation function is defined⁸ as $\overline{\delta G(B)\delta G(B + \Delta B)} = \langle [G(B) - \langle G(B) \rangle][G(B + \Delta B) - \langle G(B) \rangle] \rangle$, where angled brackets denote an average over a range of B . Taking $B_\phi = \hbar/(4eL_\phi^2)$ as the B under which one flux quantum h/e threads the area $8\pi L_\phi^2$, if $B \gg B_\phi$ the following expression allows determination of L_ϕ :

$$\overline{\delta G(B)\delta G(B + \Delta B)} = \overline{\delta G^2(B)} \frac{1}{b} \Psi' \left(\frac{1}{2} + \frac{1}{b} \right) \quad (2)$$

with $\Psi(x)$ the digamma function and $b = \Delta B/2B_\phi$.

4. ANALYSIS OF GEOMETRICAL PHASE EFFECTS

Figure 3 shows values of L_S obtained using WAL analysis at $T = 0.39$ K on InSb and Bi wires, vs wire width W .^{9,16} It is apparent that L_S increases with decreasing W , and in fact $L_S \sim 1/W$. In unconfined 2D systems, we have $L_S = L_\Omega$ for Rashba SOI,²⁵ assuming the D'yakanov-Perel motional narrowing spin decoherence is dominant. Here the spin precession length $L_\Omega = v_F/\Omega$ with Ω the spin precession frequency from the effective magnetic field arising from SOI. The unconfined spin decoherence rate is then expressed as $1/\tau_S = \Omega^2 \tau_e/2$.²⁶ With $L_S = \sqrt{D\tau_S}$, where D is the diffusion coefficient, we

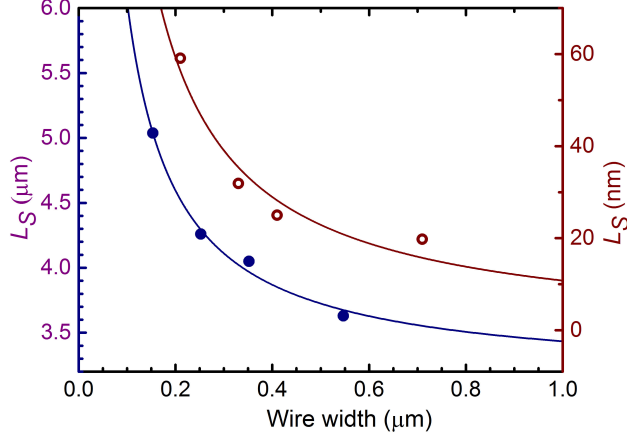


Figure 3: Values for L_S obtained by WAL analysis *vs* wire width (W). For InSb wires navy-colored filled symbols are used (left vertical axis) and for Bi wires brown open symbols are used (right vertical axis). Solid lines represent fits to a relation $L_S \propto 1/W$.

indeed have $L_S = L_\Omega$. Yet, in wires it is predicted²⁶ that $L_S = \sqrt{12}L_\Omega^2/W$, consistent with Fig. 3. This expression maps onto the behavior of L_B in wires,^{17,24} where the expressions above for L_B denote a dependence on W such that L_B increases when W narrows. In fact in the non-ballistic case, boundary conditions for a wire yield $L_B = \sqrt{3}l_m^2/W$, emphasizing the similar function of L_Ω under SOI and the magnetic l_m under B . The data in Fig. 3 are hence consistent with an electromagnetic mapping between phenomena under SOI and under applied B . The role played by L_B in decoherence phenomena is illustrated by the singlet length $L_{0,0} = \left(L_\phi^{-2} + L_B^{-2}\right)^{-\frac{1}{2}}$, where L_B and L_ϕ have identical influence in limiting quantum coherence effects in Eq. (1). The triplet lengths illustrate that L_S likewise assumes this influence in limiting quantum coherence, albeit in a more complicated way due to the specific nature of spin. We now investigate why B , via L_B , contributes to an effective decoherence. Quantum interference between partial waves in B experience an Aharonov-Bohm (AB) geometrical quantum phase^{3,4,17,27} dependent on their path in real space. Time-reversed paths will accumulate opposite AB phases, the mechanism whereby B breaks time-reversal symmetry. The magnetic length l_m (unconfined) or L_B (confined) serves as the characteristic length over which time-reversed partial waves dephase in B due to their relative accumulated AB phases. A unity quantum AB phase is accumulated in an unconfined system over a closed loop if the loop encloses a magnetic flux \hbar/e . Denoting the area enclosed by the loop as L_B^2 , it is found that $L_B = l_m \equiv \sqrt{\hbar/(eB)}$. As noted above, $L_B = \sqrt{\hbar/(eB)}$ only applies to unconfined systems, while the above other expressions for L_B have been specifically derived to apply to confined and ballistic systems. Yet in general the characteristic length for breaking of time-reversal symmetry by dephasing, is L_B and for this reason L_B has a role equivalent to L_ϕ in expressions of decoherence. It is not surprising that the accumulation of an AB phase can be expressed in terms of a length scale L_B , because the AB quantum phase is an example of a geometrical phase. This fact also delivers insight in the expression $L_B = \sqrt{3}l_m^2/W$. If the closed loop is constrained to have dimension $W < l_m$ in one direction, the electron can acquire the same AB phase by traveling a length $\propto l_m^2/W$ along the wire direction to enclose the same geometrical area. The AB phase arises from a magnetic vector potential \vec{A} . A mapping exists from Rashba SOI to the physics arising from an effective vector potential²⁸ involving \vec{E} , the actual or effective electric field at the origin of SOI by breaking inversion

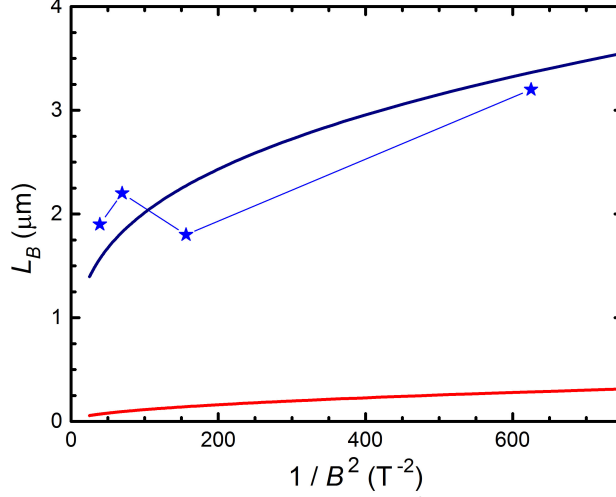


Figure 4: Experimental values for L_B plotted *vs* $1/B^2$ to emphasize the expected dependence of L_B on B (blue symbols). The upper navy-colored solid line represents the expression for L_B mentioned in the text. The lower red solid line represents $L_B = \sqrt{3}l_m^2/W$, which does not fit the data. The respective fits show that despite scatter in the data, the experiment¹⁷ succeeds in differentiating between models for L_B .

symmetry (in duality to B breaking time-reversal symmetry). This so-called Aharonov-Casher vector potential^{29,30} is $\vec{A}_{ac} = (1/c^{*2})\vec{\mu} \times \vec{E}$, where $\vec{\mu}$ is the particle's magnetic moment and c^* the effective velocity of light (a bandstructure parameter³¹). It can be shown that under SOI L_Ω takes the role assumed in B by l_m , providing an equivalent geometrical phase relation. Within prefactors of order unity dependent on boundary conditions, the geometrical phase argument that yielded $L_B \propto l_m^2/w$ now yields $L_S \propto L_\Omega^2/W$. We note that if SOI is weak, then $L_S \rightarrow \infty$ and the only length scale entering Eq. (1) is $(L_\phi^{-2} + L_B^{-2})^{-\frac{1}{2}}$. The role of L_B in this expression was confirmed experimentally in previous work¹⁷ performed using the high-mobility $\text{In}_{0.64}\text{Ga}_{0.36}\text{As}/\text{In}_{0.45}\text{Al}_{0.55}\text{As}$ heterostructure. The sample geometry was a 5×5 interferometric ring array operating in a Sagnac-like mode, which emphasizes the contribution of time-reversed paths. The measurement geometry was thus sensitive to time-reversal symmetry breaking, and indeed confirmed the phase-breaking role of L_B . Quantitative results (Fig. 4) showed that the expression $L_B = l_m \sqrt{C_1 l_m^2 \ell_e / W^3 + C_2 \ell_e^2 / W^2}$ fit the data obtained for $L_B(B)$ best, as expected for a ballistic confined system over a wider range of B . It is hence concluded that geometrical quantum phases, illustrated here by the AB phase and its electromagnetic dual, the Aharonov-Casher phase, lead to quantifiable dephasing effects in quantum transport via effective lengths, L_B and L_S *resp.* The quantifiable aspect further leads us to conclude that other geometrical phases, *e.g.* Berry's phases³² arising from the kinematics of a system, can likewise be accessed using this mesoscopic quantum transport approach.

5. ANALYSIS OF EFFECTS DUE TO DEVICE GEOMETRY

Values for L_ϕ in wires (Fig. 1) fabricated on the $\text{In}_{0.53}\text{Ga}_{0.47}\text{As}/\text{In}_{0.52}\text{Al}_{0.48}\text{As}$ heterostructure show a positive correlation with the wire length L . Figure 5 depicts L_ϕ (obtained at $T = 0.38$ K) *vs* a

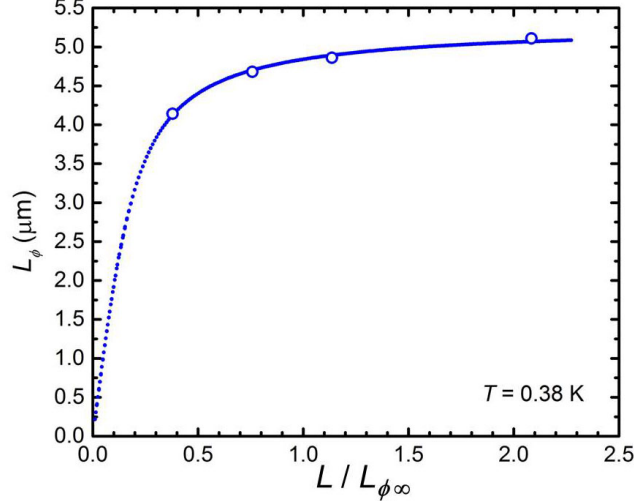


Figure 5: L_ϕ vs $L/L_{\phi\infty}$, in wires of length L at $T = 0.38$ K. Open circles represent data, and the dashed line represents a fit to the expression mentioned in the text, with $L_{\phi\infty} = 5.3$ μm .

normalized value for L in wires with $L = 2.0$ μm , 4.0 μm , 6.0 μm and 11.0 μm . An increase in L yields an increase in L_ϕ , with L_ϕ tending asymptotically to a value $L_{\phi\infty}$ for long L . The result of Fig. 5 can be explained by decoherence via interaction of electrons at the wire endpoints with the wider classical environment, named environmental coupling decoherence.⁵⁻⁷ In longer wires the interaction at the endpoints is relatively less important wires due to averaging of the measured L_ϕ over the wire. Hence longer wires show longer L_ϕ tending towards an asymptotic value $L_{\phi\infty}$ as observed. In Fig. 5 we find $L_{\phi\infty} = 5.3$ μm . $L_{\phi\infty}$ was obtained using a fit (depicted in Fig. 5) to the expression^{8,33} $L_\phi = L_{\phi\infty}(\coth(\frac{L}{L_{\phi\infty}}) - \frac{L_{\phi\infty}}{L})$, derived for the amplitude of quantum-coherent backscattering for a diffusing electron assuming perfectly transparent contacts at the wire endpoints.

In contrast to simple wires, values for L_ϕ in stadia with side-wires (Fig. 1) fabricated on the $\text{In}_{0.53}\text{Ga}_{0.47}\text{As}/\text{In}_{0.52}\text{Al}_{0.48}\text{As}$ heterostructure show a more intricate dependence on the side-wire W and L . The samples featured stadia with a common inner diameter 4.0 μm , but with varying side-wire dimensions: $W = 1.4$ μm and $L = 1.0$ μm ($W/L = 1.4$); $W = 1.0$ μm and $L = 1.0$ μm ($W/L = 1.0$); $W = 1.0$ μm and $L = 3.0$ μm ($W/L = 0.33$); $W = 0.6$ μm and $L = 1.0$ μm ($W/L = 0.6$). Figure 6 depicts L_ϕ (obtained at $T = 0.38$ K) vs W/L in the stadia. Environmental coupling decoherence predicts that the wider or shorter the side wire is, the shorter L_ϕ is, and hence cannot explain the observed dependence of L_ϕ on W/L . The results can be explained by the composite nature of the samples, namely by stadium-wire coupling decoherence. Device-device (here stadium-wire) coupling decoherence finds its origin in low wavefunction hybridization between different geometries. We express the total decoherence rate as $\frac{1}{\tau_\phi} = \frac{1}{\tau_{\phi 0}} + \frac{1}{\tau_d} + 2\gamma_\alpha$ where γ_α denotes the stadium-wire coupling decoherence rate with the factor 2 originating in 2 connection points. The second term denotes environmental interaction decoherence via τ_d .^{7,34} Between identical quantum dots in arrays,^{5,35} a low *dot-dot* coupling decoherence rate γ_α was deduced due to the identical geometries of the interacting quantum dots. In stadium-wire coupling, γ_α is similarly dependent on any geometrical similarity between the circular stadia and the side-wires. In the data of Fig. 6, the effects of γ_α are sufficiently large to be observed, dominating over $1/\tau_d$ due to

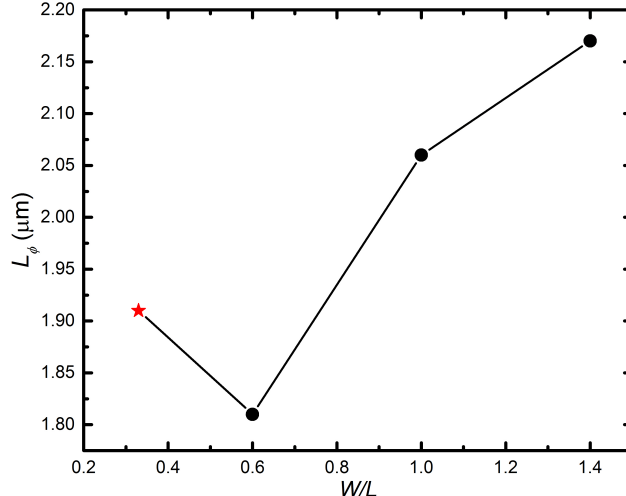


Figure 6: L_ϕ vs W/L , in stadia of with side-wires of width W and length L , at $T = 0.38$ K. Symbols represent data, and the solid line function as guide only. The datapoint represented by a red star is explained in the text.

the difference in geometry between stadia and side-wires. W and L of side-wires are comparable to the $2 \mu\text{m}$ radius of the stadia and hence stronger geometrical similarity with the stadia and the side-wires can be quantified by W/L with a lower W/L denoting stronger geometrical similarity. For the samples with $W/L > 0.33$, increasing W/L by either wider W or shorter L , increases wavefunction hybridization and hence increases L_ϕ , as shown in Fig. 6. For the sample with $W/L = 0.33$ the side-wire with long $L = 3 \mu\text{m}$ dominates the results, and environmental interaction decoherence partially masks the effect of stadium-wire coupling decoherence.

Apart from the effects of geometrical phases, the above examples show that sample geometry, including internal layout of the device and its interaction with a classical wider environment, plays an important role in determining measured values for L_ϕ .

6. CONCLUSIONS

The dependence of the quantum phase coherence length L_ϕ on geometrical phases and on device geometry is described, starting from experimental observations. An analysis of the dependence of L_ϕ on the phase space allowed for geometrical phases to develop yields insight in and a quantification of geometrical phases, which play an important role in quantum physics. Interaction with a classical environment is shown to limit quantum coherence in short wires, leading to a decreasing L_ϕ in shorter wires. For stadia, experiments show that internal stadium-wire coupling decoherence can dominate over environmental coupling decoherence effects.

ACKNOWLEDGMENTS

The work was supported by the U.S. Department of Energy, Office of Basic Energy Sciences, Division of Materials Sciences and Engineering under award DOE DE-FG02-08ER46532 (JJH), and by the National Science Foundation under award DMR-1207537 (MBS).

REFERENCES

- [1] B. Hackens, F. Delfosse, S. Faniel, C. Gustin, H. Boutry, X. Wallart, S. Bollaert, A. Cappy, and V. Bayot. Long dephasing time and high-temperature conductance fluctuations in an open InGaAs quantum dot. *Phys. Rev. B*, 66:241305(R), 2002.
- [2] J. J. Lin and J. P. Bird. Recent experimental studies of electron dephasing in metal and semiconductor mesoscopic structures. *J. Phys.: Condens. Matter*, 14:R501, 2002.
- [3] M. Ferrier and L. Angers and A. C. H. Rowe and S. Guéron and H. Bouchiat and C. Texier and G. Montambaux and D. Mailly. Direct measurement of the phase-coherence length in a GaAs/GaAlAs square network. *Phys. Rev. Lett.*, 93:246804, 2004.
- [4] S. L. Ren, J. J. Heremans, C. K. Gaspe, S. Vijayaragunathan, T. D. Mishima, and M. B. Santos. Aharonov-Bohm oscillations, quantum decoherence and amplitude modulation in mesoscopic InGaAs/InAlAs rings. *J. Phys.: Condens. Matter*, 25:435301, 2013.
- [5] M. Elhassan, J. P. Bird, R. Akis, D. K. Ferry, T. Ida, and K. Ishibashi. Dephasing due to coupling to the external environment in open quantum-dot arrays. *J. Phys.: Condens. Matter*, 17:L351, 2005.
- [6] J. P. Bird, A. P. Micolich, D. K. Ferry, R. Akis, Y. Ochiai, Y. Aoyagi, and T. Sugano. The influence of environmental coupling on phase breaking in open quantum dots. *Solid-State Electron.*, 42:1281, 1998.
- [7] B. Hackens, S. Faniel, C. Gustin, X. Wallart, S. Bollaert, A. Cappy, and V. Bayot. Dwell-time-limited coherence in open quantum dots. *Phys. Rev. Lett.*, 94:146802, 2005.
- [8] E. Akkermans and G. Montambaux. *Mesoscopic physics of electrons and photons*. Cambridge, 2007.
- [9] R. L. Kallaher, J. J. Heremans, N. Goel, S. J. Chung, and M. B. Santos. Spin and phase coherence lengths in n-InSb quasi-one-dimensional wires. *Phys. Rev. B*, 81:035335, 2010.
- [10] R. L. Kallaher, J. J. Heremans, W. Van Roy, and G. Borghs. Spin and phase coherence lengths in InAs wires with diffusive boundary scattering. *Phys. Rev. B*, 88:205407, 2013.
- [11] S. V. Iordanskii, Y. B. Lyanda-Geller, and G. E. Pikus. Weak localization in quantum wells with spin-orbit interaction. *Pis'ma Zh. Eksp. Teor. Fiz*, 60:199, 1994) (JETP Lett. 60, 206(1994)).
- [12] G. Bergmann. Weak localization and its applications as an experimental tool. *Int. J. Mod. Phys. B*, 24:2015, 2010.
- [13] V. Deo, Y. Zhang, V. Soghomonian, and J. J. Heremans. Quantum interference measurement of spin interactions in a bio-organic/semiconductor device structure. *Sci. Rep.*, 5:9487, 2015.
- [14] R. A. Jalabert, H. U. Baranger, and A. D. Stone. Conductance fluctuations in the ballistic regime: A probe of quantum chaos? *Phys. Rev. Lett.*, 65:2442, 1990.
- [15] D. K. Ferry, R. A. Akis, D. P. Pivin Jr, J. P. Bird, and N. Holmberg. Quantum transport in ballistic quantum dots. *Phys. E*, 3:137, 1998.
- [16] M. Rudolph and J. J. Heremans. Spin-orbit interaction and phase coherence in lithographically defined bismuth wires. *Phys. Rev. B*, 83:205410, 2011.
- [17] S. L. Ren, J. J. Heremans, S. Vijayaragunathan, T. D. Mishima, and M. B. Santos. Determination of time-reversal symmetry breaking lengths in an InGaAs interferometer array. *J. Phys.: Condens. Matter*, 27:185801, 2015.
- [18] M. Rudolph and J. J. Heremans. Electronic and quantum phase coherence properties of bismuth thin films. *Appl. Phys. Lett.*, 100:241601, 2012.

- [19] R. L. Kallaher, J. J. Heremans, N. Goel, S. J. Chung, and M. B. Santos. Spin-orbit interaction determined by antilocalization in an InSb quantum well. *Phys. Rev. B*, 81:075303, 2010.
- [20] Yao Zhang and J. J. Heremans. Effects of ferromagnetic nanopillars on spin coherence in an InGaAs quantum well. *Solid State Comm.*, 177:36, 2014.
- [21] P. Hofmann. The surfaces of bismuth: Structural and electronic properties. *Prog. Surf. Sci.*, 81:191, 2006.
- [22] J. J. Heremans, R. L. Kallaher, M. Rudolph, M. Santos, W. Van Roy, and G. Borghs. Spin-orbit interaction and spin coherence in narrow-gap semiconductor and semimetal wires. *Proc. of SPIE*, 9167:91670D, 2014.
- [23] A. Zduniak, M. I. Dyakonov, and W. Knap. Universal behavior of magnetoconductance due to weak localization in two dimensions. *Phys. Rev. B*, 56:1996, 1997.
- [24] C. W. J. Beenakker and H. van Houten. Boundary scattering and weak localization of electrons in a magnetic field. *Phys. Rev. B*, 38:3232, 1988.
- [25] R. Winkler. *Spin-Orbit Coupling Effects in Two-Dimensional Electron and Hole Systems*. Springer Tracts in Modern Physics 191, 2003.
- [26] S. Kettemann. Dimensional control of antilocalization and spin relaxation in quantum wires. *Phys. Rev. Lett.*, 98:176808, 2007.
- [27] A. G. Aronov and Yu. V. Sharvin. Magnetic flux effects in disordered conductors. *Rev. Mod. Phys.*, 59:755, 1987.
- [28] S. G. Tan T. Fujita, M. B. A. Jalil and S. Murakami. Gauge fields in spintronics. *J. Appl. Phys.*, 110:121301, 2011.
- [29] Y. Aharonov and A. Casher. Topological quantum effects for neutral particles. *Phys. Rev. Lett.*, 53:319, 1984.
- [30] S. Ren L. L. Xu and J. J. Heremans. Magneto-electronics at edges in semiconductor structures: helical aharonov-casher edge states. *Integr. Ferroelectr.*, 131:36, 2011.
- [31] W. Zawadzki. Zitterbewegung and its effects on electrons in semiconductors. *Phys. Rev. B*, 72:085217, 2005.
- [32] M.-C. Chang Di Xiao and Qian Niu. Berry phase effects on electronic properties. *Rev. Mod. Phys.*, 82:1959, 2010.
- [33] B. Doucot and R. Rammal. Interference effects and magnetoresistance oscillations in normal-metal networks:1-weak localization approach. *J. Physique*, 47:973, 1986.
- [34] B. Hackens, S. Faniel, C. Gustin, X. Wallart, S. Bollaert, A. Cappy, and V. Bayot. Dwell-time related saturation of phase coherence in ballistic quantum dots. *Physica E*, 34:511, 2006.
- [35] M. Elhassan, J. P. Bird, A. Shailos, C. Prasad, R. Akis, D. K. Ferry, Y. Takagaki, L.-H. Lin, N. Aoki, Y. Ochiai, K. Ishibashi, and Y. Aoyagi. Coupling-driven transition from multiple to single-dot interference in open quantum-dot arrays. *Phys. Rev. B*, 64:085325, 2001.

Jean J. Heremans is professor of Physics at Virginia Tech. He received his MS and PhD degrees from Princeton University. His current research interests include spin physics in the solid-state, spin-orbit interaction, quantum coherence, and quantum transport.

Biographies and photographs of the other authors are not available.

List of Figures

- 1 Micrographs of two example mesoscopic geometries. Right panel: an example stadium sample with side-wires with $W = 1 \mu\text{m}$ and $L = 1 \mu\text{m}$. Etched trenches, which form barriers confining the electrons, appear as lighter regions. Left panel: two U-shaped trenches define a wire between them, here with length $L = 11 \mu\text{m}$
- 2 Magnetoconductance data $G(B)$ vs B for a stadium with side-wires with $W = 1.4 \mu\text{m}$ and $L = 1.0 \mu\text{m}$, plotted over variable T . The amplitude of the UCFs decreases with increasing T due to the expected decrease in L_ϕ with increasing T . The dominant UCF signature was used in the stadia samples to obtain L_ϕ .
- 3 Values for L_S obtained by WAL analysis vs wire width (W). For InSb wires navy-colored filled symbols are used (left vertical axis) and for Bi wires brown open symbols are used (right vertical axis). Solid lines represent fits to a relation $L_S \propto 1/W$.
- 4 Experimental values for L_B plotted vs $1/B^2$ to emphasize the expected dependence of L_B on B (blue symbols). The upper navy-colored solid line represents the expression for L_B mentioned in the text. The lower red solid line represents $L_B = \sqrt{3} l_m^2/W$, which does not fit the data. The respective fits show that despite scatter in the data, the experiment¹⁷ succeeds in differentiating between models for L_B .
- 5 L_ϕ vs $L/L_{\phi\infty}$, in wires of length L at $T = 0.38$ K. Open circles represent data, and the dashed line represents a fit to the expression mentioned in the text, with $L_{\phi\infty} = 5.3 \mu\text{m}$.
- 6 L_ϕ vs W/L , in stadia of with side-wires of width W and length L , at $T = 0.38$ K. Symbols represent data, and the solid line function as guide only. The datapoint represented by a red star is explained in the text.

This paper was previously published as:

J. J. Heremans, Yuantao Xie, S. L. Ren, C. Le Priol and M. B. Santos, "Mapping electromagnetic dualities via quantum decoherence measurements in 2D materials", Proceedings of SPIE **9932**, 993207-1 (2016).

Chapter 7

Epitaxial thin films of pyrochlore iridate $\text{Bi}_{2+x}\text{Ir}_{2-y}\text{O}_{7-\delta}$: structure, defects and transport properties

This paper was previously published as: W. C. Yang, Yuantao Xie, W. K. Zhu, K. Park, A. P. Chen, Y. Losovyj, Z. Li, H. M. Liu, M. Starr, J. A. Acosta, C. G. Tao, N. Li, Q. X. Jia, J. J. Heremans and S. X. Zhang, “Epitaxial thin films of pyrochlore iridate $\text{Bi}_{2+x}\text{Ir}_{2-y}\text{O}_{7-\delta}$: structure, defects and transport properties”, *Scientific Reports* **7**, 7740 (2017). Reproduced with permission.

Epitaxial thin films of pyrochlore iridate $\text{Bi}_{2+x}\text{Ir}_{2-y}\text{O}_{7-\delta}$: structure, defects and transport properties

W. C. Yang¹, Y. T. Xie², W. K. Zhu¹, K. Park², A. P. Chen³, Y. Losovyj⁴, Z. Li^{1,3}, H. M. Liu¹, M. Starr¹, J. A. Acosta¹, C. G. Tao², N. Li³, Q. X. Jia^{3,5}, J. J. Heremans² & S. X. Zhang¹

While pyrochlore iridate thin films are theoretically predicted to possess a variety of emergent topological properties, experimental verification of these predictions can be obstructed by the challenge in thin film growth. Here we report on the pulsed laser deposition and characterization of thin films of a representative pyrochlore compound $\text{Bi}_2\text{Ir}_2\text{O}_7$. The films were epitaxially grown on yttria-stabilized zirconia substrates and have lattice constants that are a few percent larger than that of the bulk single crystals. The film composition shows a strong dependence on the oxygen partial pressure. Density-functional-theory calculations indicate the existence of Bi_i antisite defects, qualitatively consistent with the high Bi: Ir ratio found in the films. Both Ir and Bi have oxidation states that are lower than their nominal values, suggesting the existence of oxygen deficiency. The iridate thin films show a variety of intriguing transport characteristics, including multiple charge carriers, logarithmic dependence of resistance on temperature, antilocalization corrections to conductance due to spin-orbit interactions, and linear positive magnetoresistance.

Iridates have recently emerged as a fertile ground for novel topological electronic states that arise from the interplay of electron interactions and spin-orbit coupling¹⁻⁹. In particular, the pyrochlore compounds with a chemical formula of $\text{A}_2\text{Ir}_2\text{O}_7$ (A-227, where A = Bi, Y or rare-earth element) are predicted to host a variety of topological phases, including topological Mott insulators^{3,4}, Weyl semimetals⁶, topological crystalline insulators¹⁰, and Weyl-Mott insulators¹¹. The pyrochlore iridate compounds have a cubic crystal structure ($Fm\bar{3}m$), in which the A^{3+} and Ir^{4+} cations form inter-penetrating networks of corner-sharing tetrahedra. The energy scale of electron interaction relative to electron hopping (i.e. U/t) increases monotonically as the A-site ionic radius decreases¹²; and the electrical transport properties can be divided roughly into three categories^{8,13}: 1) compounds with large A^{3+} (e.g. Bi-227 and Pr-227) show a metallic behavior down to the lowest measured temperature $T^5,13-16$; 2) those with intermediate A^{3+} (e.g. Eu-227 and Nd-227) display a metal-to-insulator transition^{13,16-19}, which is often accompanied by a paramagnetic to an antiferromagnetic phase transition; and 3) substances with small A^{3+} (e.g. Lu-227 and Yb-227) exhibit an insulating-like behavior^{13,15,20} throughout the entire region of T .

While significant experimental progress has recently been made in bulk A-227 compounds^{5,17-38}, including the demonstration of all-in/all-out non-collinear magnetic order^{24,38}, observation of giant magnetoresistance associated with metallic domain walls³⁴⁻³⁶ and indication of Weyl semimetal phases^{18,37}, there are only a few studies on thin film samples³⁹⁻⁴³, which is largely due to the great challenges in obtaining high quality films. Theoretical studies on pyrochlore iridate thin films have suggested a variety of emergent topological properties, including the quantized anomalous Hall conductance⁴⁴ and the correlated Chern insulator⁴⁵ that are otherwise not accessible in bulk samples. While these topological properties have yet been realized experimentally, remarkable transport phenomena have been observed in thin films, including a linear magnetoresistance (MR) up to 35 Tesla in Bi-227³⁹ and a cooling field-dependent, asymmetric MR in Eu-227⁴⁰. Moreover, thin film structures provide an excellent platform to engineer physical properties by means of, for example, electric gating and elastic strain, offering great potentials for device applications.

¹Department of Physics, Indiana University, Bloomington, Indiana, 47405, USA. ²Department of Physics, Virginia Tech, Blacksburg, Virginia, 24061, USA. ³Center for Integrated Nanotechnologies, Los Alamos National Laboratory, Los Alamos, 87545, USA. ⁴Department of Chemistry, Indiana University, Bloomington, Indiana, 47405, USA. ⁵Department of Materials Design and Innovation, University at Buffalo, The State University of New York, Buffalo, NY, 14260, USA. W. C. Yang, Y. T. Xie and W. K. Zhu contributed equally to this work. Correspondence and requests for materials should be addressed to S.X.Z. (email: sxzhang@indiana.edu)

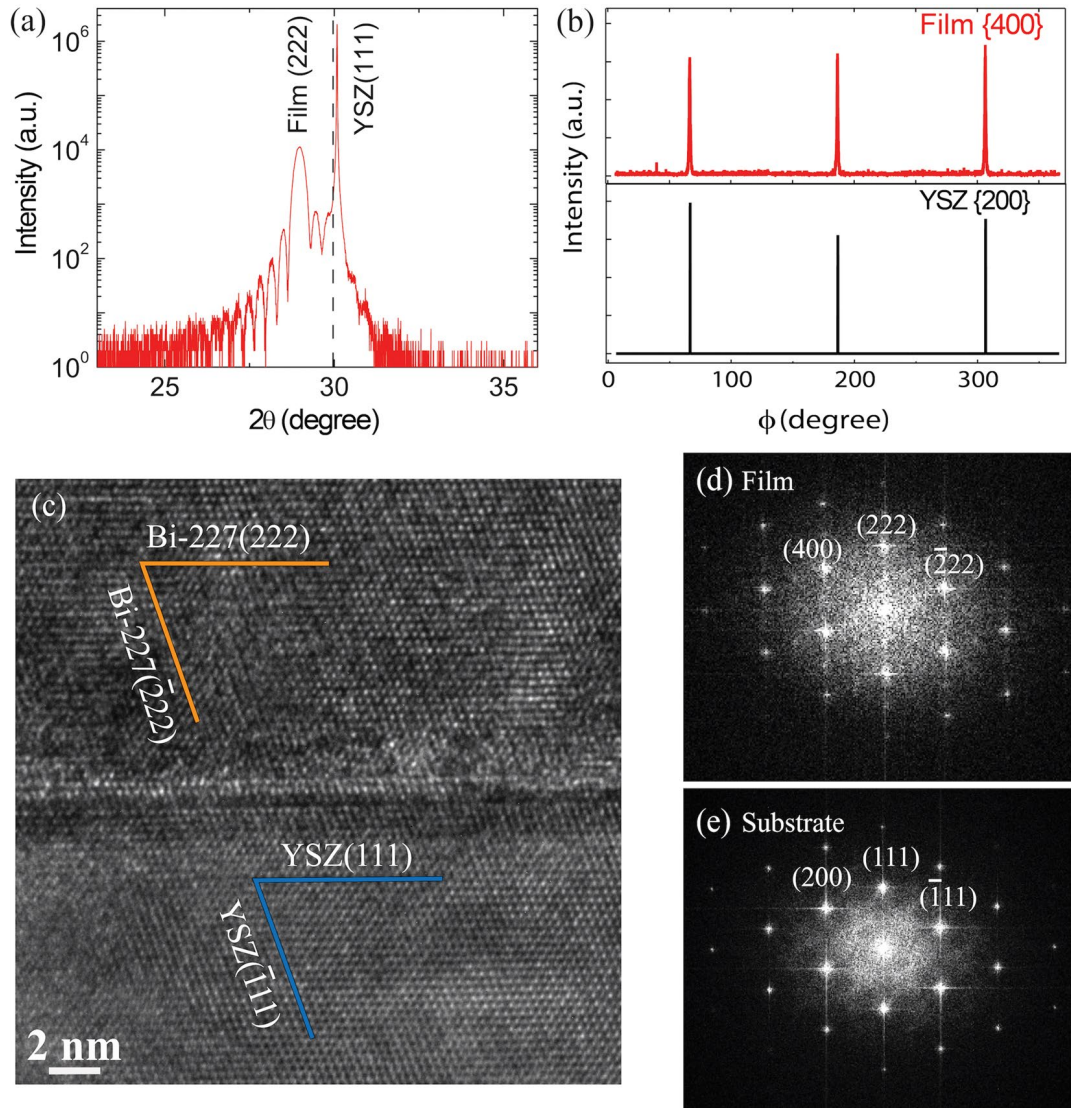


Figure 1. X-ray diffraction characterizations and TEM studies of a representative Bi-227 thin film grown at $P_{O_2} = 50$ mTorr using Ir/Bi@1 target (f1): (a) 2θ - ω scan around YSZ (111) reflection showing the (111) and (222) peaks of the substrate and thin film, respectively. The dashed line indicates the (222) peak position of the bulk single crystal Bi-227^{14,29}. (b) in-plane φ -scan for the {200} of YSZ substrate and the {400} of thin film. (c) Cross-sectional TEM image taken at the interface of thin film and substrate; Fast Fourier Transform images from (d) thin film and (e) substrate.

In this paper, we report on systematic measurements of the structural, compositional, and electrical transport properties of a prototypical pyrochlore iridate, namely Bi-227 thin films. The films were grown epitaxially along the [111] direction on the yttrium-stabilized zirconia (YSZ) (111) substrates by pulsed laser deposition (PLD). The out-of-plane lattice parameters of thin films were found to be a few percent larger than that of the bulk samples. Compositional characterizations, density-functional-theory (DFT) calculations, along with X-ray photoelectron spectroscopy (XPS) studies suggest the existence of Bi_{Ir} antisite defects and oxygen vacancies. With varied defect densities, thin films show a broad spectrum of electronic transport characteristics, including multiple charge carriers, logarithmic dependence of resistance on T , antilocalization, and linear positive magnetoresistance.

Results and Discussions

PLD growth, structural and compositional characterizations. Thin films were grown by PLD using two targets that were prepared via a solid state reaction method with IrO_2 and Bi_2O_3 as source materials at Ir/Bi ratios of 1 and 3 (labeled as Ir/Bi@1 target and Ir/Bi@3 target, respectively). X-ray diffraction (XRD) measurements suggest that thin films are epitaxially grown on the YSZ substrates along the [111] direction of a cubic phase. Figure 1(a) shows a local 2θ - ω scan taken on a representative film grown at oxygen partial pressure $P_{O_2} = 50$ mTorr using the Ir/Bi@1 target. A well-defined oscillation was observed near the thin film (222) peak, indicating a high crystalline quality and smooth film surface. The film thickness was determined to be ~ 26 nm

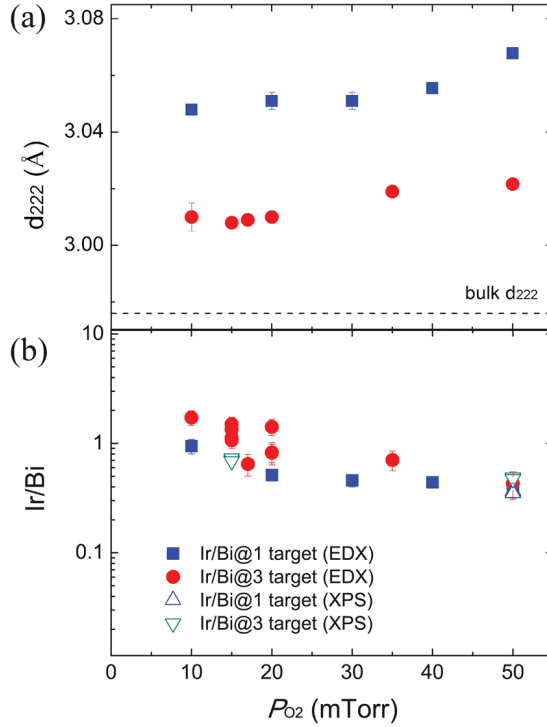


Figure 2. (a) lattice spacing d_{222} versus oxygen pressure P_{O_2} . The error bars were estimated according to the diffraction peaks. (b) Ir/Bi ratio versus P_{O_2} (multiple data points at the same pressure were taken at different spots/areas of the sample). The error bars were determined based on the EDX analysis in the AZtech software.

based on the X-ray reflectivity. The out-of-plane d -spacing for the (222) film peak (d_{222}) is ~ 3.07 Å, which is $\sim 3\%$ larger than that of bulk Bi-227, i.e., $d_{222} \sim 2.98$ Å^{44,29}. The in-plane φ -scan shows a clear three-fold symmetry (Fig. 1 (b)), confirming that the film has a cubic crystalline structure and is epitaxially grown on the substrate. The epitaxial relationship between the thin film and the substrate was determined to be (222)Bi-227|| (111)YSZ and [022]Bi-227|| [011]YSZ based on the φ -scan and the cross-sectional transmission electron microscopy (TEM) measurements (Fig. 1(c,d and e)).

We note that elongation (contraction) in the out-of-plane d -spacing was also observed in a layered iridate Sr_2IrO_4 and its origin was demonstrated to be in-plane compression (tension)^{46,47}. While a compressive in-plane strain may exist in the Bi-227 film due to its lattice mismatch with the substrate ($a_{\text{bulk Bi-227}} \sim 10.32$ Å versus $2a_{\text{YSZ}} \sim 10.25$ Å), the elongation in out-of-plane d -spacing here cannot be solely attributed to the in-plane compression. Indeed, a 1.5% in-plane compression is required for 3% out-of-plane elongation in order to maintain the unit cell volume constant. However, the lattice mismatch between the film (assuming bulk lattice constant) and the substrate is only 0.6%, smaller than the required compression. To understand the origin of the large lattice elongation, we further carried out film growth at different P_{O_2} using two different targets since oxygen content and cation stoichiometry can be strongly correlated with the out-of-plane lattice parameters in complex oxide thin films⁴⁸⁻⁵⁰. As shown in Fig. 2(a), the spacing d_{222} (and hence the lattice constant $a = 2\sqrt{3}d_{222}$ of the cubic unit cell) decreases with the decrease of P_{O_2} . At the same P_{O_2} , the film grown using the Ir/Bi@3 target has a smaller lattice constant than that grown using the Ir/Bi@1 target. The minimum d_{222} (or a) obtained in these films is still $\sim 1.3\%$ larger than that of the bulk sample. To gain further insight, we characterized the chemical compositions of the films using two complementary techniques, i.e. XPS and energy-dispersion X-ray spectroscopy (EDX) which show consistent dependence of Ir/Bi ratio on P_{O_2} (Fig. 2(b)). The ratio increases from ~ 0.4 to ~ 1 when P_{O_2} is decreased from 50 mTorr to 10 mTorr. The low Ir/Bi ratio at high P_{O_2} should be attributed to the high vapor pressure of IrO_3 . We also note that a Pt/Bi ratio of ~ 0.62 (or Bi/Pt ~ 1.62) was determined in another pyrochlore film $Bi_2Pt_2O_7$ ⁵¹; these results suggest that the pyrochlore phase is stable over a wide range of compositions. When P_{O_2} is 30 mTorr or lower, a small Ir (111) peak is observed in the XRD pattern (see Supplementary Fig. S1), indicating the formation of Ir metal impurity. The film grown at $P_{O_2} = 1$ mTorr is dominated by Ir metal and the Ir/Bi ratio is found to be > 10 (see Supplementary Figs S1 and S2(c)). The high Ir/Bi ratio obtained in low P_{O_2} may be attributed to the high volatility of Bi metal and stability of Ir. At the same P_{O_2} , the films deposited from the Ir/Bi@3 target have slightly higher Ir/Bi ratios than the ones from the Ir/Bi@1 target. Nevertheless, the dependence of film composition on the target is much weaker than on P_{O_2} .

Density Functional Theory Calculations. The low Ir/Bi ratio in the films grown at high P_{O_2} indicates the possible existence of antisite (Bi_{Ir}) and/or Bi interstitial (Bi_{int}) defects which can result in a larger lattice constant than the stoichiometric compound (the ionic radius of Bi^{3+} is larger than Ir^{4+}). To verify this possibility, we computed the formation energies of the above two types of defects via DFT calculations, in which a range of chemical

Bi: Ir antisite [Bi interstit.]	Case 1	Case 2	Case 3	Case 4	Case 5
$\Delta_{\text{Bi}}^{T=0}$ (eV)	0	-3.77	0	-2.20	0
$\Delta_{\text{Ir}}^{T=0}$ (eV)	-7.54	-3.77	-5.79	-2.20	0
$\Delta\mu_{\text{O}}^{T=0}$ (eV)	0	0	-0.5	-0.9	-2.15
Form. Eng. ΔE_f (eV)	-7.47 [4.86]	-4.04 [6.50]	-5.72 [4.86]	-4.04 [4.93]	4.04 [4.86]
Notes	ΔE_f at $T = 550$ C, $P = 50$ mTorr	ΔE_f at $T = 550$ C, $P = 15$ mTorr	ΔE_f at $T = 550$ C, $P = 50$ mTorr	ΔE_f at $T = 550$ C, $P = 15$ mTorr	ΔE_f at $T = 0$

Table 1. Calculated formation energies ΔE_f of a single Bi_{Ir} defect and a Bi_{int} in the pyrochlore structure of Bi_{227} with the chemical potential differences of Bi, Ir, and O, $\Delta_{\text{Bi}}^{T=0}$, $\Delta_{\text{Ir}}^{T=0}$, and $\Delta\mu_{\text{O}}^{T=0}$ at $T = 0$ in five different cases. The un-bracketed (bracketed) numbers are the formation energies of the Bi_{Ir} (Bi_{int}) defect. Here the minimum value of both $\Delta_{\text{Bi}}^{T=0}$ and $\Delta_{\text{Ir}}^{T=0}$ is -7.54 eV, and the minimum value of $\Delta\mu_{\text{O}}^{T=0}$ is -2.15 eV, considering the zero-temperature DFT-calculated Bi_{227} formation enthalpy per unit (consisting of 2 Bi, 2 Ir, and 7 O atoms) to be -15.08 eV. For the calculation of ΔE_f , the temperature and oxygen pressure dependence of $\Delta\mu_{\text{O}}$ was included except for Case 5.

potential differences of Bi, Ir and O are considered (Table 1). When the chemical potential of elemental Bi, Ir, or O is the same as that of bulk Bi, bulk Ir, or O_2 gas, respectively, i.e. the chemical potential difference is zero, the Bi, Ir, or O is said to be in an “abundant” condition. A decrease of chemical potential difference corresponds to the decrease of element content; in other words, the lower the chemical potential difference is, the “more deficient” the element is. Our calculations show that the Bi_{int} defects have a consistently high formation energy (4.86 ~6.50 eV), indicating a low possibility of this defect in the films. In contrast, the formation energy of the antisite Bi_{Ir} defect varies from negative to positive, depending mainly on the oxygen content or the chemical potential difference between the element O and O_2 gas. When oxygen is abundant (cases #1 and 2) or slightly deficient (cases #3 and 4), the formation energy is found to be negative. Comparing case #1 with #2 (or #3 with #4) suggests that the more deficient the Ir is, the more stable the Bi_{Ir} defect is; furthermore, comparison between cases #1 and 3 (or between #2 and 4) indicates that the more abundant the oxygen is, the more stable the defect is. Particularly, in case #1 when oxygen is abundant and Ir is deficient, the formation energy reaches a minimum value of -7.47 eV, suggesting that the antisite defect is very stable in this condition. The calculated result is qualitatively consistent with the experimental result in Fig. 2(a), i.e. the Ir/Bi ratio in the film increases as P_{O_2} decreases. When oxygen is very deficient but Bi and Ir are abundant (case #5), the antisite defect is unlikely to form as indicated by a positive formation energy of 4.04 eV, consistent with the high Ir/Bi (>10) observed at the lowest P_{O_2} (see Supplementary Fig. S2(c)).

X-ray photoelectron spectroscopy studies of oxidation states. The films grown at $P_{\text{O}_2} = 15\sim 50$ mTorr were found to be slightly oxygen-deficient, as suggested by the XPS studies. The XPS measurement was taken on three representative films, i.e. f1 ($P_{\text{O}_2} = 50$ mTorr, Ir/Bi@1 target), f2 ($P_{\text{O}_2} = 50$ mTorr, Ir/Bi@3 target), and f3 ($P_{\text{O}_2} = 15$ mTorr, Ir/Bi@3 target), along with two control samples, i.e. bulk IrO_2 and Bi_2O_3 . The Ir 4f spectrum and Bi 4f spectrum for films f1 and f3 are presented in Fig. 3, and the same for f2 are provided in the Supplementary Fig. S3. A qualitative comparison between the spectra of the films and that of the bulk IrO_2 (and Bi_2O_3) (see Supplementary Fig. S4) suggests that both Ir (and Bi) have a component with an oxidation state lower than the nominal +4 (and +3). We fitted the spectra using two components in CasaXPS software to obtain more quantitative information. The symmetric component is described by the Gaussian-Lorentz profile GL(m), while the asymmetric lineshape which is used to capture the many-body, screening effects⁵² is described by the convolution of Gelius profile A(a,b,n) and Gaussian-Lorentz profile GL(m), in which the asymmetry is determined by the parameters a and b. More detailed information about the fitting process is provided in the supplemental information. The fitting spectra at the optimal a and b values are shown in Fig. 3. The obtained binding energies for Ir 4f_{5/2} peaks are: 65.8~66.1 eV (component 1) and 64.4~64.5 eV (component 2); the binding energies for Ir 4f_{7/2} peaks are: 62.8~63.1 eV (component 1); and 61.4~61.5 eV (component 2). The existence of two components may be attributed to the appearance of two final states in the photoemission process^{53, 54}, the coexistence of the core lines and plasmon satellite^{55, 56}, and a mixed oxidation state⁵⁷. In either case, however, the fact that the entire measured spectra are shifted to lower binding energies in comparison to IrO_2 (Ir^{4+}) suggests the formation of oxygen vacancies in the films. Similarly, the Bi spectrum can be fitted using two components as well (Fig. 3(b)): binding energies of 163.8~164.1 eV (component 1) and 163.0~163.2 eV (component 2) for the 4f_{5/2} peak; and 158.5~158.8 eV (component 1) and 157.7~157.9 eV (component 2) for the 4f_{7/2} peak. Again the binding energies being lower than for Bi^{3+} indicates the presence of oxygen deficiency.

The existence of Bi_{Ir} defects and oxygen vacancies in our pyrochlore thin films is not too surprising. First, cation antisite defects have already been observed in other pyrochlore compounds such as $\text{Gd}_2\text{Zr}_2\text{O}_7$ ⁵⁸. Second, the structure of pyrochlore $\text{Bi}_2\text{Ir}_2\text{O}_7$ is remarkably similar to that of the cubic $\delta\text{-Bi}_2\text{O}_3$ ⁵⁹ which can be viewed as $\text{Bi}_2\text{Bi}_2\text{O}_6$. Figure 4 shows a unit cell of the cubic $\delta\text{-Bi}_2\text{O}_3$, a 1/8 unit cell of $\text{Bi}_2\text{Ir}_2\text{O}_7$ with and without antisite defects and oxygen vacancies. In comparison to $\text{Bi}_2\text{Ir}_2\text{O}_7$, the cubic $\delta\text{-Bi}_2\text{O}_3$ has one less oxygen atom and all Ir sites are occupied by Bi. As a result, a significant amount of Bi_{Ir} defects and oxygen vacancies can exist in $\text{Bi}_2\text{Ir}_2\text{O}_7$ while maintaining its cubic crystal structure.

Transport measurements and discussion. With the existence of antisite defects and oxygen vacancies, the $\text{Bi}_{2+x}\text{Ir}_{2-y}\text{O}_{7-\delta}$ thin films show revealing electronic transport properties. The dependence on T of the

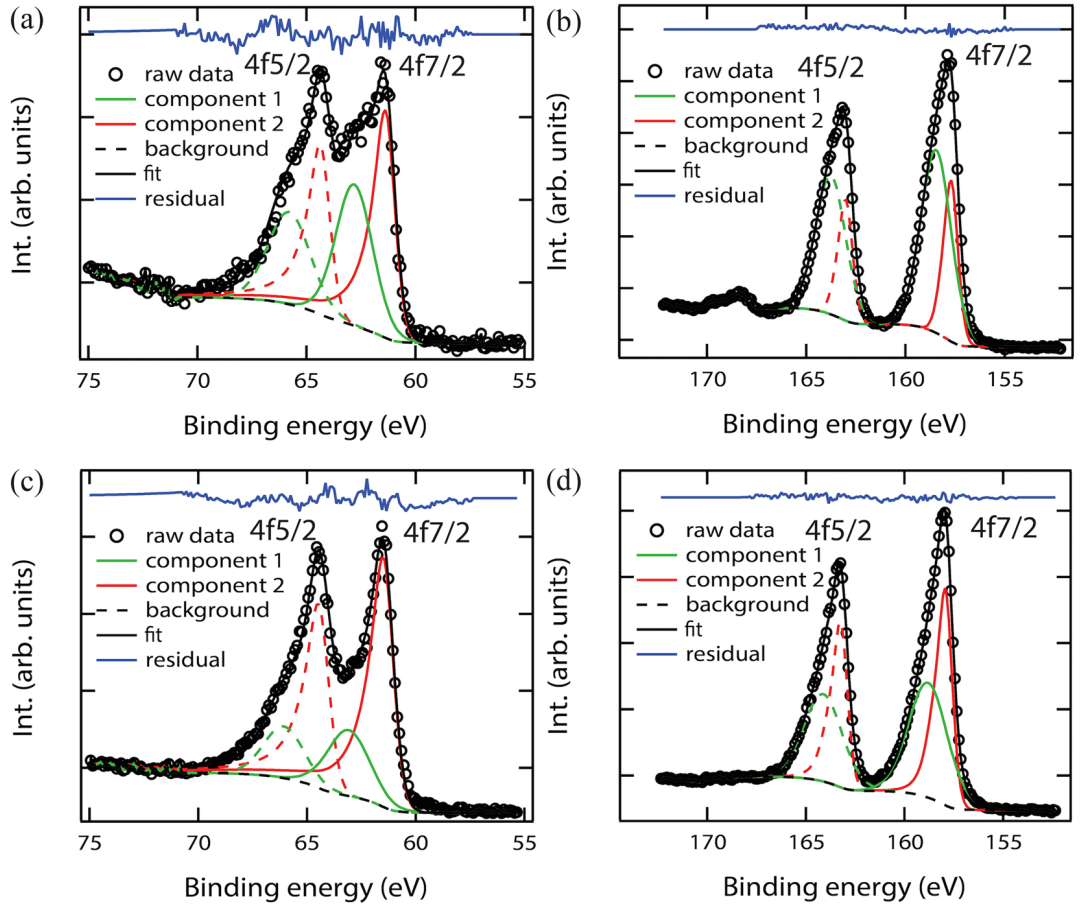


Figure 3. XPS (a) Ir $4f_{5/2}$ and $4f_{7/2}$ spectra and (b) Bi $4f_{5/2}$ and $4f_{7/2}$ spectra taken on film f1. (c) Ir $4f_{5/2}$ and $4f_{7/2}$ spectra and (d) Bi $4f_{5/2}$ and $4f_{7/2}$ spectra taken on film f3. The spectra were fitted using two components: a symmetric component (higher binding energy peak) described by the Gaussian-Lorentz profile $GL(m)$, and an asymmetric component (lower binding energy peak) by the convolution of Gelius profile $A(a,b,n)$ and Gaussian-Lorentz profile $GL(m)$. The parameters a and b are optimized as described in the supplementary information.

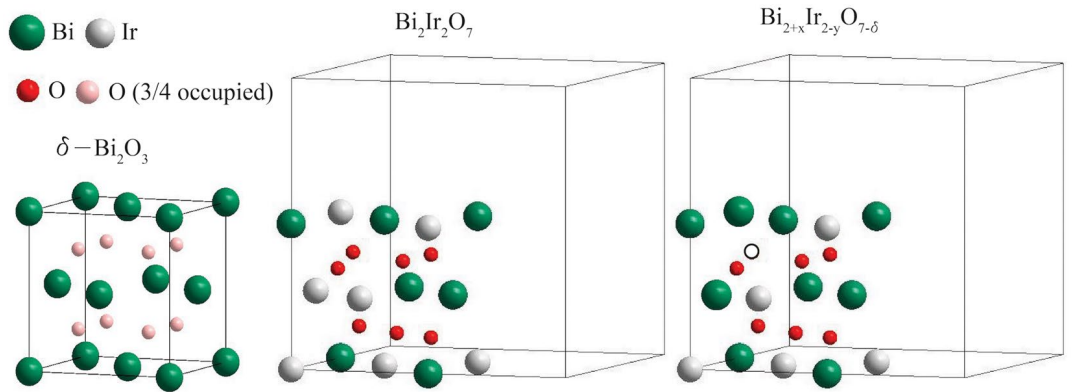


Figure 4. A unit cell of cubic δ - Bi_2O_3 , $1/8$ unit cell of $\text{Bi}_2\text{Ir}_2\text{O}_7$ and $\text{Bi}_{2+x}\text{Ir}_{2-y}\text{O}_{7-\delta}$. In the $\text{Bi}_{2+x}\text{Ir}_{2-y}\text{O}_{7-\delta}$ shown above (as an example), two Ir atoms are replaced by Bi atoms and one oxygen atom is missing (represented by the open circle).

sheet resistance (2D resistivity) R_{\square} at magnetic field $B=0$ and the low- T magnetoresistance (MR, R_{\square} vs B) and the Hall resistance R_H vs B were obtained on Hall bars (inset in Fig. 5 and *cfr.* Methods) prepared by photolithography and dry etching on the three representative films, f1, f2, and f3. Values for R_{\square} at $B=0$ and $T=0.39$ K are, $483\Omega/\square$ (f1), $1334\Omega/\square$ (f2), and $1013\Omega/\square$ (f3). As observed in Fig. 5 at $T=0.39$ K, R_H shows a non-linear

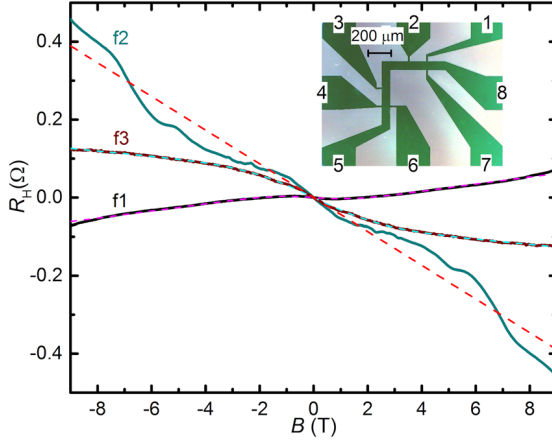


Figure 5. Hall resistance R_H vs B at $T = 0.39$ K for films f1, f2 and f3 (solid lines, films as indicated), with fits to a two-carrier model (f1, f3, dashed lines) or an averaging single-carrier model (f2, dashed line). The polarities are chosen such that a negative slope corresponds to positive charge carriers. The inset represents the L-shaped Hall bar geometry used on all 3 films (contacts 5 and 8 are current contacts, contacts 1, 2, 3, 4, 6, 7 are voltage contacts for measurement of R_H and R_{\square}).

dependence on B for all films, suggesting the existence of multiple types of charge carriers. In particular, $R_H(B)$ of f1 can be fitted to a two-carrier model by including both electrons and holes, while f3 is found to host two types of holes with different carrier mobilities. The sheet charge carrier densities (n_e for electrons, n_h for holes) and mobilities (μ_e for electrons, μ_h for holes) determined from the fittings at $T = 0.39$ K are: $n_e = 8.0 \times 10^{20} \text{ m}^{-2}$, $\mu_e = 1.5 \times 10^{-5} \text{ m}^2 \text{ V}^{-1} \text{ s}^{-1}$ and $n_h = 2.0 \times 10^{12} \text{ m}^{-2}$, $\mu_h = 0.38 \text{ m}^2 \text{ V}^{-1} \text{ s}^{-1}$ for film f1; $n_h = 6.4 \times 10^{20} \text{ m}^{-2}$, $\mu_h = 1.0 \times 10^{-5} \text{ m}^2 \text{ V}^{-1} \text{ s}^{-1}$ and $n_h = 3.0 \times 10^{12} \text{ m}^{-2}$, $\mu_h = 0.23 \text{ m}^2 \text{ V}^{-1} \text{ s}^{-1}$ for film f3. $R_H(B)$ for f2 cannot be fitted to a two-carrier model, yet the use of more than two types of carriers will lead to uncertainty in the fitting values due to the proliferation of fitting parameters. While the complicated $R_H(B)$ for f2 indicates the presence of multiple carriers, its slope indicates that the dominant charge carriers are holes, with average $n_h = 1.4 \times 10^{20} \text{ m}^{-2}$. The clear experimental evidence for the presence of multiple charge carriers in films f1, f2 and f3 is qualitatively consistent with the existence of multiple bands in the electronic structures⁶⁰. The multiple bands will impart different effective masses, qualitatively consistent also with the experimental evidence for different mobilities. While oxygen vacancies are expected to function as n -type dopants and Bi_{Ir} antisite defects as p -type dopants, it is less certain that the observed carrier densities should be associated with doping via these different types of defects since thermal ionization of defect levels may not be effective at $T = 0.39$ K. At the high defect density present in the films, *e.g.* where 1/3 of Ir is replaced by Bi, the defects can be expected to impact the electronic band structure instead of solely change the Fermi level via doping, not captured in DFT calculations based on assumed stoichiometry. Association between observed transport properties and specific defects therefore requires future theoretical and experimental studies of band structure in the presence of high defect densities.

All three films show metallic behavior in R_{\square} vs T at high T , as Fig. 6 shows. At intermediate T , the films show a logarithmic increase of R_{\square} with decreasing T such that $1/R_{\square} \sim \ln(T/T_0)$ (Fig. 6). The transition from metallic to logarithmic insulating behavior occurs for f1 at 10 K, for f2 at 50 K and for f3 at 55 K. It is apparent that among the three films, f1 maintains its metallic character to the lowest T , compatible with a higher crystalline quality. Indeed, XRD for f1 shows the sharpest features (see Supplementary Fig. S1), a sign of the best crystalline quality among the films. The logarithmic dependence of the sheet conductance (2D conductivity) $G_{\square} = 1/R_{\square}$ on T , depicted in Fig. 7, can at $B = 0$ be expressed as:

$$G_{\square} = G_{\square 0} + \alpha(e^2/2\pi^2\hbar)\ln(T/T_0) \quad (1)$$

where $G_{\square 0}$ denotes a T -independent part, T_0 is a normalization constant, and α denotes a prefactor. Figure 7 depicts $G_{\square}(B = 0)$ vs T on a semi-logarithmic graph, with fits to Equation (1) yielding $\alpha = 0.67$ for f1, $\alpha = 0.71$ for f2 and $\alpha = 0.87$ for f3. The values for α are typical for thin films in general, where α of order unity is most often encountered⁶¹. Two mechanisms can lead to a logarithmic dependence but in all present films have opposite effects on G_{\square} : antilocalization which will tend to increase G_{\square} with decreasing T at $B = 0$, and electron-electron interactions which will tend to decrease G_{\square} with decreasing T . Antilocalization results from the destructive interference of partial waves on time-reversed paths returning to the origin of the paths, occurring in the presence of spin-orbit interaction when the mobility mean-free-path is shorter than the quantum phase coherence length⁶¹⁻⁶⁶. Antilocalization is accompanied by a characteristic positive MR, observed in the films⁶¹⁻⁶⁶. Figure 8 shows the MR obtained at $T = 0.39$ K for the films. A pronounced low- B positive MR characteristic of antilocalization is observed for all three films, transitioning to a linear positive MR at high B (discussed below). The existence of antilocalization confirms the presence of spin-orbit interaction in the films, and accounts for the observation of relatively low $\alpha < 1$. As a quantum coherence effect, the antilocalization correction to the classical

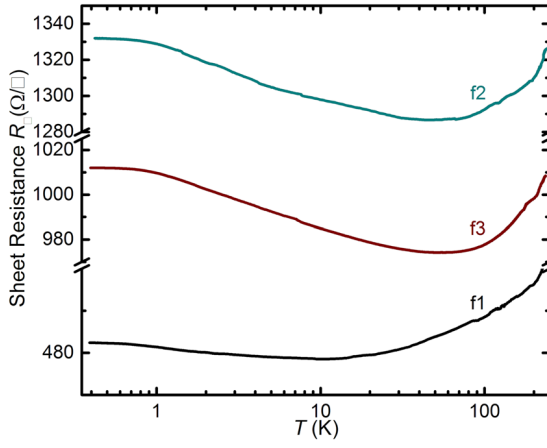


Figure 6. Sheet resistance R_{\square} vs T at $B=0$ for films f1, f2 and f3 (films as indicated).

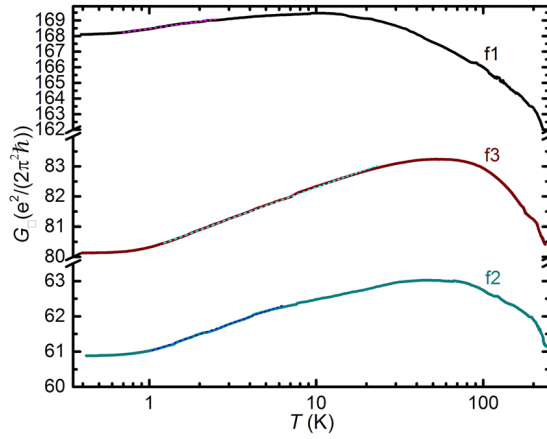


Figure 7. Sheet conductance G_{\square} vs T at $B=0$ for films f1, f2 and f3 (solid lines, films as indicated), with fits to the low- T data using Equation (1) (dashed lines).

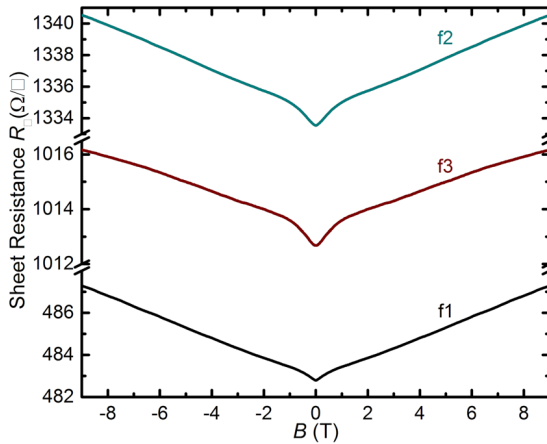


Figure 8. Sheet resistance R_{\square} vs B at $T=0.39$ K for films f1, f2 and f3 (films as indicated). A positive MR attributed to antilocalization is visible for $B < 1$ T, and a linear positive MR appears for $B > 1.5$ T.

sheet conductance strengthens with decreasing T , which increases G_{\square} with decreasing T . On the other hand, electron-electron interactions can directly decrease G_{\square} ($B=0$) with decreasing T via the Aronov-Altshuler mechanism⁶⁷, where the interaction leads to an effective suppression of the density-of-states at the Fermi level

in diffusive transport. The Aronov-Altshuler mechanism results in a logarithmic dependence on T as expressed in Equation (1) with α ranging from 0.25 (strong screening of electron-electron interactions) to 1 (no screening)^{61,66}. The Aronov-Altshuler mechanism is also accompanied by a weak positive MR⁶¹. In the present films the dependence $G_{\square} \sim \ln(T/T_0)$ down to $T \approx 1$ K with prefactor $\alpha < 1$, and the upturn in G_{\square} for $T < 1$ K are attributed to the competing effects of antilocalization and the Aronov-Altshuler electron-electron interaction mechanism. The observation of positive MR at low B (Fig. 8) is further consistent with the presence of both antilocalization and the Aronov-Altshuler mechanism. A detailed analysis of the exact contribution of each effect is outside the scope of this work. The linear positive MR at higher $B > 1.5$ T in Fig. 8 is similar to the MR observed in previous work on thin film Bi-227³⁹, although no hysteresis was observed in our thin films. We ascribe the linear positive MR at high B to the underlying electronic structure featuring a linear dispersion. Although its exact origins are still debated, a positive linear MR has indeed consistently appeared in the context of materials with a linear dispersion or quasi-relativistic dispersion (Dirac materials, topological insulators, Bi, InSb)⁶⁸.

Conclusions

In conclusion, we have achieved epitaxial growth of pyrochlore iridate thin films on yttria-stabilized zirconia substrate via pulsed laser deposition. The lattice constants of the films are a few percent larger than that of the bulk single crystal, and the film composition shows a strong dependence on the oxygen partial pressure P_{O_2} . DFT calculations indicate the existence of Bi_{Ir} , which is qualitatively consistent with the large lattice constant and low Ir/Bi ratio found in the films grown at a relatively high P_{O_2} . Both Ir and Bi have oxidation states that are lower than their nominal values, suggesting the existence of oxygen deficiency. With antisite defects and oxygen vacancies, the $Bi_{2+x}Ir_{2-y}O_{7-\delta}$ thin films show a variety of intriguing electronic transport properties, including multi-carrier transport, a logarithmic dependence of conductance on T , an antilocalization quantum correction to conductance due to spin-orbit interaction, and linear positive magnetoresistance.

Methods

Experimental details. Thin films of $Bi_{2+x}Ir_{2-y}O_{7-\delta}$ were grown on yttria-stabilized zirconia (YSZ) (111) substrates by PLD. Two ceramic targets were prepared via a solid state reaction method using IrO_2 and Bi_2O_3 as source materials at Ir/Bi ratios of 1 and 3 (labeled as Ir/Bi@1 target and Ir/Bi@3 target, respectively). The repetition rate of the KrF excimer laser ($\lambda = 248$ nm) was 1 Hz and the nominal energy density was ~ 3.33 J/cm². The substrate heater temperature was set to 750 °C (actual substrate temperature ~ 550 °C), and P_{O_2} was varied from 1 to 50 mTorr. Films grown at three representative conditions labeled as f1 ($P_{O_2} = 50$ mTorr, Ir/Bi@1 target); f2 ($P_{O_2} = 50$ mTorr, Ir/Bi@3 target); and f3 ($P_{O_2} = 15$ mTorr, Ir/Bi@3 target), were the focus of this work. After deposition, the PLD chamber was filled with oxygen gas up to about atmosphere pressure, in which thin films were cooled down. X-ray diffraction (Panalytical X'Pert PRO MRD) 2θ - ω (Triple axis mode) and φ -scans (Rocking curve mode) were carried out in Los Alamos National Laboratory to obtain information on the orientation, lattice parameters and epitaxial quality of the thin films. Further XRD measurements were also carried out in Indiana University using a standard PANalytical instrument with a Chi-Phi-Z sample stage (Cu K_{α}). Cross-section specimens for TEM were prepared by mechanical polishing of the film to a final thickness of ~ 60 μ m with a diamond lapping film, followed by a thinning process using a Gatan Precision Ion Polishing System Model 691. TEM characterization was conducted in an FEI Tecnai F30 transmission electron microscope. Energy-dispersion X-ray spectroscopy (EDX) measurement was carried out in a scanning electron microscope (SEM, Quanta FEI). X-ray photoelectron spectroscopy (XPS) data were obtained on a PHI VersaProbe II Scanning X-ray Microprobe system. All XPS spectra were calibrated using the carbon 1s peak at 284.8 eV. Magnetotransport measurements were performed on microfabricated Hall bars (*cfr.* inset in Fig. 5), obtained by photolithography followed by reactive ion etching in BCl_3 . The Hall elements were L-shaped to enable characterization of anisotropic transport properties (anisotropy was not observed). The active region of the Hall elements had a length-to-width ratio of 2 (160 μ m length, 80 μ m width), sufficiently high to allow observation of a clear Hall signal despite the low values for $R_H(B)$. Ohmic contacts were photolithographically fabricated as unannealed pads of 5 nm Cr / 40 nm Au. Magnetotransport was measured over 390 mK $< T < 270$ K in a sample-in-liquid ³He system. Excitation currents varied between 5 nA (for R_{\square}) to 20 nA (for R_H), sufficiently low to avoid carrier heating. Zero-field resistances were measured during cool-down from 270 K to 390 mK with magnetic field $B = 0$ T (ZFC). Magnetoresistances were then measured at 390 mK over -9 T $< B < 9$ T. Samples were subsequently brought to $T = 30$ K and $B = 4.0$ T and cooled to $T = 390$ mK at $B = 4.0$ T (FC). Magnetoresistances were then remeasured at 390 mK over -9 T $< B < 9$ T. Differences in data between ZFC and FC conditions were not apparent and hence magnetotransport data obtained under ZFC conditions only are shown.

DFT calculation details. Density-functional theory calculations were carried out on the pyrochlore structure with and without defects by using DFT code, VASP^{69,70}. The generalized gradient approximation (GGA)⁷¹ was used for exchange-correlation functional and projector-augmented wave (PAW) pseudopotentials⁷². Spin-orbit coupling was included self-consistently within the DFT calculation. For the perfect Bi-227 pyrochlore structure, we considered a face-centered cubic (fcc) primitive unit cell of 22 atoms with the experimental lattice constant of 5.155 Å¹⁴ and relaxed the geometry until the residual forces became less than 0.01 eV/Å. The energy cutoff of 400 eV and $9 \times 9 \times 1$ k -point mesh were used for the relaxation and the self-consistent run of the optimized geometry.

For the structure with defects, we considered two different types of defects, i.e. Bi: Ir antisite (Bi_{Ir}) and Bi interstitial (Bi_{int}) that could result in the high Bi to Ir ratio found in the experiment. In each defect type, we simulated an 88-atom supercell with one defect when the structure is electrically neutral (see Supplementary Fig. S6). Possible oxygen vacancies were not introduced in the structure. In the structure with defects, the geometry was relaxed with $5 \times 5 \times 1$ k -point mesh and an energy cutoff of 400 eV until the residual forces were less than

0.01 eV/Å. The formation energy of a Bi antisite defect is $\Delta E_f = E_{anti} - E_0 - (\mu_{Bi}^{bulk} + \Delta\mu_{Bi}) + (\mu_{Ir}^{bulk} + \Delta\mu_{Ir})$, whereas the formation energy of an interstitial Bi defect is $\Delta E_f = E_{int} - E_0 - (\mu_{Bi}^{bulk} + \Delta\mu_{Bi})$, where E_{anti} , E_{int} , and E_0 are total energies of the structure with an antisite defect, with an interstitial defect, and without any defects, respectively⁷³⁻⁷⁵. Here μ_{Bi}^{bulk} and μ_{Ir}^{bulk} are the chemical potential of bulk Bi and Ir, while $\Delta\mu_{Bi}$ and $\Delta\mu_{Ir}$ are the chemical potential differences from their bulk values. The chemical potentials of bulk Bi and Ir were calculated from DFT. The chemical potential differences depend on sample growth conditions, and their ranges are bounded by the formation enthalpy ΔH_f of Bi-227 (without defects) such as $\Delta H_f = 2\Delta\mu_{Bi} + 2\Delta\mu_{Ir} + 7\Delta\mu_O$, where $\Delta\mu_O$ is the chemical potential difference of two O atoms from an O₂ molecule in the gas phase. The DFT-calculated formation enthalpy of Bi-227 from the elemental Bi, Ir, and O₂ gas molecule is -15.08 eV. Therefore, the minimum values of $\Delta\mu_{Bi}$, $\Delta\mu_{Ir}$, and $\Delta\mu_O$ are -7.54 , -7.54 , and -2.15 eV, respectively, since their maximum values are zero. These DFT-calculated numbers assume $T = 0$. To include the temperature and oxygen pressure effect, we considered $\Delta\mu_O(T, P) = \Delta\mu_O(T, P_0) + (1/2)k_B T \ln(T/T_0)$, where the first term is the chemical potential difference of oxygen at T and pressure $P_{O_2} = 1$ atm which can be obtained by applying the ideal gas law and the standard tabulated values for the O₂ gas ($T_0 = 298$ K, $P_{O_2} = 1$ atm)⁷⁴.

References

- Kim, B. J. *et al.* Novel $J_{eff} = 1/2$ Mott state induced by relativistic spin-orbit coupling in Sr₂IrO₄. *Phys. Rev. Lett.* **101**, 076402 (2008).
- Kim, B. J. *et al.* Phase-Sensitive Observation of a Spin-Orbital Mott State in Sr₂IrO₄. *Science* **323**, 1329–1332 (2009).
- Pesin, D. & Balents, L. Mott physics and band topology in materials with strong spin-orbit interaction. *Nature Physics* **6**, 376–381 (2010).
- Yang, B. J. & Kim, Y. B. Topological insulators and metal-insulator transition in the pyrochlore iridates. *Phys. Rev. B* **82**, 085111 (2010).
- Machida, Y., Nakatsuji, S., Onoda, S., Tayama, T. & Sakakibara, T. Time-reversal symmetry breaking and spontaneous Hall effect without magnetic dipole order. *Nature* **463**, 210–213 (2010).
- Wan, X. G., Turner, A. M., Vishwanath, A. & Savrasov, S. Y. Topological semimetal and Fermi-arc surface states in the electronic structure of pyrochlore iridates. *Phys. Rev. B* **83**, 205101 (2011).
- Kim, J. *et al.* Magnetic excitation spectra of Sr₂IrO₄ probed by resonant inelastic x-ray scattering: establishing links to cuprate superconductors. *Phys. Rev. Lett.* **108**, 177003 (2012).
- Witczak-Krempa, W., Chen, G., Kim, Y. B. & Balents, L. Correlated Quantum Phenomena in the Strong Spin-Orbit Regime. *Annu. Rev. Condens. Matter Phys.* **5**, 57–82 (2014).
- Schaffer, R., Kin-Ho Lee, E., Yang, B.-J. & Kim, Y. B. Recent progress on correlated electron systems with strong spin-orbit coupling. *Rep. Prog. Phys.* **79**, 094504 (2016).
- Kargarian, M. & Fiete, G. A. Topological Crystalline Insulators in Transition Metal Oxides. *Phys. Rev. Lett.* **110**, 156403 (2013).
- Morimoto, T. & Nagaosa, N. Weyl Mott Insulator. *Scientific Reports* **6**, 19853 (2016).
- Koo, H. J., Whangbo, M. H. & Kennedy, B. J. Similarities and Differences in the Structural and Electronic Properties of Ruthenium and Iridium Pyrochlores A₂M₂O_{7-γ} (M=Ru, Ir). *J. Solid State Chem.* **136**, 269–273 (1998).
- Matsuhira, K., Wakeshima, M., Hinatsu, Y. & Takagi, S. Metal-Insulator Transitions in Pyrochlore Oxides Ln₂Ir₂O₇. *J. Phys. Soc. Jpn.* **80**, 094701 (2011).
- Qi, T. F. *et al.* Strong magnetic instability in correlated metallic Bi₂Ir₂O₇. *J. Phys. Condens. Matter* **24**, 345601 (2012).
- Yanagishima, D. & Maeno, Y. Metal-nonmetal changeover in pyrochlore iridates. *J. Phys. Soc. Jpn.* **70**, 2880–2883 (2001).
- Matsuhira, K. *et al.* Metal-Insulator Transition in Pyrochlore Iridates Ln₂Ir₂O₇ (Ln=Nd, Sm, and Eu). *J. Phys. Soc. Jpn.* **76**, 043706 (2007).
- Ishikawa, J. J., O'Farrell, E. C. T. & Nakatsuji, S. Continuous transition between antiferromagnetic insulator and paramagnetic metal in the pyrochlore iridate Eu₂Ir₂O₇. *Phys. Rev. B* **85**, 245109 (2012).
- Ueda, K. *et al.* Variation of charge dynamics in the course of metal-insulator transition for pyrochlore-type Nd₂Ir₂O₇. *Phys. Rev. Lett.* **109**, 136402 (2012).
- Disseler, S. M. *et al.* Magnetic order and the electronic ground state in the pyrochlore iridate Nd₂Ir₂O₇. *Phys. Rev. B* **85**, 174441 (2012).
- Disseler, S. M. *et al.* Magnetic order in the pyrochlore iridates A₂Ir₂O₇ (A=Y, Yb). *Phys. Rev. B* **86**, 014428 (2012).
- Tafti, F. F., Ishikawa, J. J., McCollam, A., Nakatsuji, S. & Julian, S. R. Pressure-tuned insulator to metal transition in Eu₂Ir₂O₇. *Phys. Rev. B* **85**, 205104 (2012).
- Guo, H. J. *et al.* Magnetic order in the pyrochlore iridate Nd₂Ir₂O₇ probed by muon spin relaxation. *Phys. Rev. B* **88**, 060411 (2013).
- Zhao, S. *et al.* Magnetic transition, long-range order, and moment fluctuations in the pyrochlore iridate Eu₂Ir₂O₇. *Phys. Rev. B* **83**, 180402(R) (2011).
- Sagayama, H. *et al.* Determination of long-range all-in-all-out ordering of Ir⁴⁺ moments in a pyrochlore iridate Eu₂Ir₂O₇ by resonant x-ray diffraction. *Phys. Rev. B* **87**, 100403(R) (2013).
- Shapiro, M. C. *et al.* Structure and magnetic properties of the pyrochlore iridate Y₂Ir₂O₇. *Phys. Rev. B* **85**, 214434 (2012).
- Sakata, M. *et al.* Suppression of metal-insulator transition at high pressure and pressure-induced magnetic ordering in pyrochlore oxide Nd₂Ir₂O₇. *Phys. Rev. B* **83**, 041102(R) (2011).
- Tomiyasu, K. *et al.* Emergence of Magnetic Long-range Order in Frustrated Pyrochlore Nd₂Ir₂O₇ with Metal-Insulator Transition. *J. Phys. Soc. Jpn.* **81**, 034709 (2012).
- Baker, P. J. *et al.* Weak magnetic transitions in pyrochlore Bi₂Ir₂O₇. *Phys. Rev. B* **87**, 180409(R) (2013).
- Lee, Y. S. *et al.* Infrared study of the electronic structure of the metallic pyrochlore iridate Bi₂Ir₂O₇. *Phys. Rev. B* **87**, 195143 (2013).
- Takatsu, H., Watanabe, K., Goto, K. & Kadowaki, H. Comparative study of low-temperature x-ray diffraction experiments on R₂Ir₂O₇ (R=Nd, Eu, and Pr). *Phys. Rev. B* **90**, 235110 (2014).
- Hozoi, L. *et al.* Longer-range lattice anisotropy strongly competing with spin-orbit interactions in pyrochlore iridates. *Phys. Rev. B* **89**, 115111 (2014).
- Liu, H. *et al.* Magnetic order, spin dynamics and transport properties of the pyrochlore iridate Y₂Ir₂O₇. *Solid State Commun.* **179**, 1–5 (2014).
- Zhu, W. K., Wang, M., Seradjeh, B., Yang, F. & Zhang, S. X. Enhanced weak ferromagnetism and conductivity in hole-doped pyrochlore iridate Y₂Ir₂O₇. *Phys. Rev. B* **90**, 054419 (2014).
- Ueda, K. *et al.* Magnetic Field-Induced Insulator-Semimetal Transition in a Pyrochlore Nd₂Ir₂O₇. *Phys. Rev. Lett.* **115**, 056402 (2015).
- Ma, E. Y. *et al.* Mobile metallic domain walls in an all-in-all-out magnetic insulator. *Science* **350**, 538–541 (2015).
- Tian, Z. *et al.* Field-induced quantum metal-insulator transition in the pyrochlore iridate Nd₂Ir₂O₇. *Nat Phys* **12**, 134–138 (2016).
- Sushkov, A. B. *et al.* Optical evidence for a Weyl semimetal state in pyrochlore Eu₂Ir₂O₇. *Phys. Rev. B* **92**, 241108 (2015).

38. Disseler, S. M. Direct evidence for the all-in/all-out magnetic structure in the pyrochlore iridates from muon spin relaxation. *Phys. Rev. B* **89**, 140413 (2014).
39. Chu, J.-H. *et al.* Linear magnetoresistance and time reversal symmetry breaking of pyrochlore iridates $\text{Bi}_2\text{Ir}_2\text{O}_7$. *arXiv* **1309**, 4750 (2013).
40. Fujita, T. C. *et al.* Odd-parity magnetoresistance in pyrochlore iridate thin films with broken time-reversal symmetry. *Sci Rep* **5**, 9711 (2015).
41. Fujita, T. C. *et al.* All-in-all-out magnetic domain wall conduction in a pyrochlore iridate heterointerface. *Phys. Rev. B* **93**, 064419 (2016).
42. Gallagher, J. C. *et al.* Epitaxial growth of iridate pyrochlore $\text{Nd}_2\text{Ir}_2\text{O}_7$ films. *Sci Rep* **6**, 22282 (2016).
43. Fujita, T. C. *et al.* All-in-all-out magnetic domain size in pyrochlore iridate thin films as probed by local magnetotransport. *Appl. Phys. Lett.* **108**, 022402 (2016).
44. Yang, B. J. & Nagaosa, N. Emergent topological phenomena in thin films of pyrochlore iridates. *Phys. Rev. Lett.* **112**, 246402 (2014).
45. Chen, Q., Hung, H.-H., Hu, X. & Fiete, G. A. Correlation effects in pyrochlore iridate thin films grown along the [111] direction. *Phys. Rev. B* **92**, 085145 (2015).
46. Rayan Serrao, C. *et al.* Epitaxy-distorted spin-orbit Mott insulator in Sr_2IrO_4 thin films. *Phys. Rev. B* **87**, 085121 (2013).
47. Nichols, J. *et al.* Tuning electronic structure via epitaxial strain in Sr_2IrO_4 thin films. *Appl. Phys. Lett.* **102**, 141908 (2013).
48. Chen, A. P. *et al.* Strong oxygen pressure dependence of ferroelectricity in $\text{BaTiO}_3/\text{SrRuO}_3/\text{SrTiO}_3$ epitaxial heterostructures. *J. Appl. Phys.* **114**, 124101 (2013).
49. Enriquez, E. *et al.* Oxygen vacancy-driven evolution of structural and electrical properties in $\text{SrFeO}_{3-\delta}$ thin films and a method of stabilization. *Appl. Phys. Lett.* **109**, 141906 (2016).
50. Harrell, Z. *et al.* Oxygen content tailored magnetic and electronic properties in cobaltite double perovskite thin films. *Appl. Phys. Lett.* **110**, 093102 (2017).
51. Gutiérrez-Llorente, A. *et al.* Epitaxial crystals of $\text{Bi}_2\text{Pt}_2\text{O}_7$ pyrochlore through the transformation of $\delta\text{-Bi}_2\text{O}_3$ fluorite. *APL Mater.* **3**, 036105 (2015).
52. Campagna, M., Wertheim, G. K., Shanks, H. R., Zumsteg, F. & Banks, E. Local Character of Many-Body Effects in X-Ray Photoemission from Transition-Metal Compounds: Na_xWO_3 . *Phys. Rev. Lett.* **34**, 738–741 (1975).
53. Kahk, J. M. *et al.* Understanding the Electronic Structure of IrO_2 Using Hard-X-ray Photoelectron Spectroscopy and Density-Functional Theory. *Phys. Rev. Lett.* **112**, 117601 (2014).
54. Pfeifer, V. *et al.* The electronic structure of iridium and its oxides. *Surf. Interface. Anal.* **48**, 261–273 (2016).
55. Payne, D. J. *et al.* Why is lead dioxide metallic? *Chem. Phys. Lett.* **411**, 181–185 (2005).
56. Bourlange, A. *et al.* The influence of Sn doping on the growth of In_2O_3 on Y-stabilized ZrO_2 (100) by oxygen plasma assisted molecular beam epitaxy. *J. Appl. Phys.* **106**, 013703 (2009).
57. Sanchez Casalongue, H. G. *et al.* In situ observation of surface species on iridium oxide nanoparticles during the oxygen evolution reaction. *Angewandte Chemie International Edition* **53**, 7169–7172 (2014).
58. Gregg, D. J. *et al.* Cation antisite disorder in uranium-doped gadolinium zirconate pyrochlores. *J. Nucl. Mater.* **452**, 474–478 (2014).
59. Yashima, M. & Ishimura, D. Crystal structure and disorder of the fast oxide-ion conductor cubic Bi_2O_3 . *Chem. Phys. Lett.* **378**, 395–399 (2003).
60. Wang, Q. *et al.* Experimental electronic structure of the metallic pyrochlore iridate $\text{Bi}_2\text{Ir}_2\text{O}_7$. *J. Phys.: Condens. Matter* **27**, 015502 (2014).
61. Lee, P. A. & Ramakrishnan, T. V. Disordered electronic systems. *Rev. Mod. Phys.* **57**, 287–337 (1985).
62. Akkermans, E. & Montambaux, G. *Mesoscopic physics of electrons and photons*. (Cambridge University Press, 2007).
63. Kallaher, R. L. & Heremans, J. J. Spin and phase coherence measured by antilocalization in n-InSb thin films. *Phys. Rev. B* **79**, 075322 (2009).
64. Rudolph, M. & Heremans, J. J. Spin-orbit interaction and phase coherence in lithographically defined bismuth wires. *Phys. Rev. B* **83**, 205410 (2011).
65. Hikami, S., Larkin, A. I. & Nagaoka, Y. Spin-orbit interaction and magnetoresistance in the two dimensional random system. *Prog. Theor. Phys.* **63**, 707–710 (1980).
66. Markiewicz, R. S. & Rollins, C. J. Localization and electron-interaction effects in a two-dimensional metal with strong spin-orbit scattering: Pd films. *Phys. Rev. B* **29**, 735–747 (1984).
67. Altshuler, B. L. & Aronov, A. G. Zero bias anomaly in tunnel resistance and electron-electron interaction. *Solid State Commun.* **30**, 115–117 (1979).
68. Veldhorst, M. *et al.* Magnetotransport and induced superconductivity in Bi based three-dimensional topological insulators. *physica status solidi (RRL) - Rapid Research Letters* **7**, 26–38 (2013).
69. Kresse, G. & Furthmüller, J. Efficient iterative schemes for ab initio total-energy calculations using a plane-wave basis set. *Phys. Rev. B* **54**, 11169–11186 (1996).
70. Kresse, G. & Furthmüller, J. Efficiency of ab-initio total energy calculations for metals and semiconductors using a plane-wave basis set. *Comp. Mater. Sci.* **6**, 15–50 (1996).
71. Perdew, J. P., Burke, K. & Ernzerhof, M. Generalized gradient approximation made simple. *Phys. Rev. Lett.* **77**, 3865–3868 (1996).
72. Blöchl, P. E. Projector augmented-wave method. *Phys. Rev. B* **50**, 17953–17979 (1994).
73. Zhang, S. B. & Northrup, J. E. Chemical potential dependence of defect formation energies in GaAs: Application to Ga self-diffusion. *Phys. Rev. Lett.* **67**, 2339–2342 (1991).
74. Osorio-Guillen, J., Lany, S., Barabash, S. V. & Zunger, A. Magnetism without magnetic ions: percolation, exchange, and formation energies of magnetism-promoting intrinsic defects in CaO. *Phys. Rev. Lett.* **96**, 107203 (2006).
75. Van de Walle, C. G. First-principles calculations for defects and impurities: Applications to III-nitrides. *J. Appl. Phys.* **95**, 3851 (2004).

Acknowledgements

We thank Professor J. Wang, Dr. Y. Wang, Prof. Y. Lan, Dr. C.-H. Chen and S. Cheema for fruitful discussions. S. X. Z. acknowledges start-up support from Indiana University (IU) College of Arts and Sciences. J. J. H. and Y. X. were supported for the transport measurements by the U.S. Department of Energy, Office of Basic Energy Sciences, Division of Materials Sciences and Engineering under award DOE DE-FG02-08ER46532. K.P. is grateful to John W. Villanova for creating the initial pyrochlore structure and to Denis Demchenko for an advice in computation of formation energy, and was supported by U.S. National Science Foundation DMR-1206354, San Diego Supercomputer Center (SDSC) Comet and Gordon under DMR060009N, and Advanced Research Computing at Virginia Tech. We thank the IU Nanoscale Characterization Facility for access to the scanning electron microscope. XPS instrument at Nanoscale Characterization Facility of IU Nanoscience Center was funded by NSF Award DMR MRI-1126394. The X-ray diffraction facilities at the IU Molecular Structure Center was supported by NSF Grant No. CHE-1048613. The work at Los Alamos National Laboratory was supported by

the NNSA's Laboratory Directed Research and Development Program and was performed, in part, at the Center for Integrated Nanotechnologies, an Office of Science User Facility operated for the U.S. Department of Energy (DOE) Office of Science. Los Alamos National Laboratory, an affirmative action equal opportunity employer, is operated by Los Alamos National Security, LLC, for the National Nuclear Security Administration of the U.S. Department of Energy under contract DE-AC52-06NA25396.

Author Contributions

W.C.Y., W.K.Z. and M.S. carried out thin film growth. W.C.Y. performed XRD and EDX measurements and XPS analysis. W.K.Z. carried out XRD characterizations. Y.T.X. conducted transport measurements and data analysis under the supervision of J.J.H., K.P. carried out DFT calculations and analysis. A.P.C. performed XRD characterizations under the supervision of Q.X.J., Y.L. conducted XPS measurements and guided W.C.Y. on XPS analysis. Z.L. carried out TEM characterizations and analysis under the supervision of N.L., L.H. and J.A.A. assisted on EDX characterizations. S.X.Z., J.J.H., W.K.Z., W.C.Y., and K.P. prepared the manuscript. All authors participated in discussion and reviewed the manuscript. S.X.Z. conceived and directed the overall project.

This paper was previously published as:

W. C. Yang, YuantaoXie, W. K. Zhu, K. Park, A. P. Chen, Y. Losovyj, Z. Li, H. M. Liu, M. Starr, J. A. Acosta, C. G. Tao, N. Li, Q. X. Jia, J. J. Heremans and S. X. Zhang, "Epitaxial thin films of pyrochlore iridate $\text{Bi}_{2+x}\text{Ir}_{2-y}\text{O}_{7-\delta}$: structure, defects and transport properties", *Scientific Reports* **7**, 7740 (2017).

Chapter 8

Magnetotransport properties of epitaxial Ge/AlAs heterostructures integrated on GaAs and silicon

This paper was previously published as: M. K. Hudait, M. Clavel, P. S. Goley, Yuantao Xie and J. J. Heremans, “Magnetotransport properties of epitaxial Ge/AlAs heterostructures integrated on GaAs and silicon”, *ACS Applied Materials & Interfaces* **7**, 22315 (2015). Reproduced with permission.

Magnetotransport Properties of Epitaxial Ge/AlAs Heterostructures Integrated on GaAs and Silicon

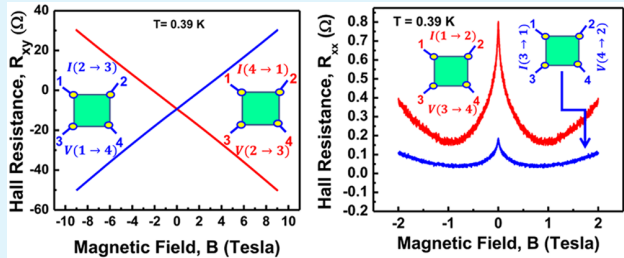
Mantu K. Hudait,^{*,†} Michael Clavel,[†] Patrick S. Goley,[†] Yuantao Xie,[‡] and Jean J. Heremans[‡]

[†]Advanced Devices & Sustainable Energy Laboratory (ADSEL), Bradley Department of Electrical and Computer Engineering, Virginia Tech, Blacksburg, Virginia 24061, United States

[‡]Department of Physics, Virginia Tech, Blacksburg, Virginia 24061, United States

ABSTRACT: The magnetotransport properties of epitaxial Ge/AlAs heterostructures with different growth conditions and substrate architectures have been studied under ± 9 T magnetic field and at 390 mK temperature. Systematic mobility measurements of germanium (Ge) epilayers grown on GaAs substrates at growth temperatures from 350 to 450 °C allow us to extract a precise growth window for device-quality Ge, corroborated by structural and morphological properties. Our results on Si substrate using a composite metamorphic AlAs/GaAs buffer at 400 °C Ge growth temperature, show that the Ge/AlAs system can be tailored to have a single carrier transport while keeping the charge solely in the Ge layer. Single carrier transport confined to the Ge layer is demonstrated by the weak-localization quantum correction to the conductivity observed at low magnetic fields and 390 mK temperature. The weak localization effect points to a near-absence of spin-orbit interaction for carriers in the electronically active layer and is used here for the first time to pinpoint Ge as this active layer. Thus, the epitaxial Ge grown on Si using AlAs/GaAs buffer architecture is a promising candidate for next-generation energy-efficient fin field-effect transistor applications.

KEYWORDS: germanium, transport, epitaxy, molecular beam epitaxy, heterostructure



INTRODUCTION

Germanium (Ge) is an attractive material due to its higher electron and hole mobilities than silicon (Si) for future generation low-power and high-speed nanoscale logic transistors. In the last several decades, transistors using Ge directly deposited on Si,^{1,2} Ge on Si using graded SiGe buffer,^{3,4} Ge-on-insulator-on-Si (GeOI) by bonding,⁵ compressively strained Ge in a quantum well (QW) configuration on Si,⁶ and bulk Ge,⁷ all have been studied. Yet these methods have not achieved higher valence band and conduction band offsets for carrier confinement. Very recently, epitaxial Ge heterogeneously integrated on Si using composite metamorphic AlAs/GaAs buffers^{8,9} obtained by molecular beam epitaxy (MBE) illustrated a promising path to understand the effect of growth temperature, the role of an AlAs buffer layer underneath the Ge layer and their effect on the magnetotransport properties of epitaxial Ge. It has been well-documented that the large bandgap semiconductor buffer layers such as GaAs, InAlAs,^{10,11} or oxide buffer layer¹² can be considered to eliminate the parallel conduction either from the substrate or through the buffer layer to the active device layer of interest. For example, in a metamorphic InGaAs QW transistor structure on Si, the composite GaAs/In_xAl_{1-x}As buffer eliminates the parasitic conduction to the active InGaAs channel.^{10,11} In order to achieve a device-quality epitaxial Ge layer on large bandgap buffer, it is necessary to understand the role of the buffer layer, the growth temperature, and the growth pause that provides the film quality.

The temperature-dependent mobility as measured by the van der Pauw technique and subsequent analysis by the quantitative mobility spectrum (QMSA) are often used to determine the (1) channel mobility, (2) parallel conduction to active channel, and (3) the carrier freeze-out for high mobility III-V materials.^{10,11,13,14} However, the QMSA method fails for materials with mobility below 1000 cm²/(V s). Therefore, it is necessary to find an alternative way to determine the mobility and carrier density contributed solely by the Ge layer grown on a large bandgap material, such as AlAs, where carriers are confined within the Ge layer. Furthermore, a well-controlled heterointerface between the epitaxial Ge and the large bandgap AlAs buffer layer is crucial to realize high-performance nanoscale Ge transistors. Here, we report on the growth by MBE of a series of Ge/AlAs/GaAs structures as well as a Ge/AlAs/GaAs/Si structure and their characterization. In particular, we discuss the effect of (1) the AlAs buffer layer, (2) the duration of the growth pause, (3) the growth temperature, (4) the different annealing temperatures, and (5) the reliability of repeated mobility measurements from 90 to 315 K of the Ge layers. The structures were grown using two solid-source MBE chambers, connected via an ultrahigh vacuum transfer chamber. We also note that the in situ growth process of Ge following

the large bandgap AlAs buffer is mandatory since the AlAs layer is prone to oxidize once removed from the ultrahigh vacuum chamber prior to epitaxial Ge layer growth. The Ge/AlAs/GaAs/Si structure was characterized at low temperatures (down to 390 mK) under magnetic fields up to 9 T to investigate the carrier transport behavior inside the Ge layer. The magneto-transport measurements demonstrate single carrier confinement inside the Ge layer. Furthermore, the Ge/AlAs/GaAs/Si structure exhibited weak-localization, pointing to a near absence of spin-orbit interaction. This observation in turn suggests that only carriers within the Ge layer contribute to transport. The weak localization quantum correction to the conductivity was obtained by careful sweeps of the magnetic field at the lowest measurement temperatures. Furthermore, X-ray analysis was performed to ascertain interface quality, surface morphology was visualized by atomic force microscopy (AFM), and defect/interface properties were evaluated using cross-sectional transmission electron microscopy (TEM), all to establish pathways for Ge based materials and their device structures.

RESULTS AND DISCUSSION

Structural Analysis of Epitaxial Ge on GaAs with AlAs Buffer. Figure 1 shows the schematic of layer structures

80 nm Ge (350°C, 400°C, 450°C)	240 nm Ge (400°C)
170 nm AlAs	170 nm AlAs
250 nm GaAs	2.0 μm GaAs
(100)/2° GaAs (a)	(100)/6° Si (b)

Figure 1. Schematic of epitaxial Ge layers grown on (a) GaAs and (b) Si substrates, respectively. Ge epitaxial layers were grown at 350, 400, and 450 °C on GaAs substrate, and at 400 °C on Si substrate.

studied in this work. The 80 nm epitaxial Ge layers were grown on semi-insulating (100)/2° offcut GaAs substrates at growth temperatures of 350, 400, and 450 °C with the growth rate of approximately 25 nm/h. The growth temperature in this study refers to thermocouple temperature during growth. The low growth rate was selected to prevent interdiffusion at the Ge/AlAs heterointerface.^{8,9} The 240 nm Ge layer was grown on (100)/6° Si substrate using the composite metamorphic AlAs/GaAs buffer shown in Figure 1b. The detailed material analysis of Ge on Si using AlAs/GaAs buffer was reported earlier.⁸ The structural quality and the relaxation state of each Ge layer structure on GaAs were evaluated using high-resolution (004) X-ray rocking curves as shown in Figure 2. The peak positions of Ge, AlAs, and GaAs substrate are clearly visible in these figures. The angular separation $\Delta\theta$ between the (004) diffraction peaks of GaAs and Ge resulting from the difference in lattice plane spacing $\Delta d/d$ can also provide the microstructural quality. Both the AlAs and Ge peak positions with respect to the GaAs substrate attest to the lattice matched nature of the layer structure, as expected. The full width at half-maximum (FWHM) of Ge layers were found to be 50, 51, and 47 arcsec for the growth temperatures of 350, 400, and 450 °C, respectively. The X-ray analysis thus suggests that there is a wide range of growth temperature window for the epitaxial Ge layer. However, the higher growth temperature must be avoided to minimize the interdiffusion of Ga, As, and Ge atoms at the heterointerface.

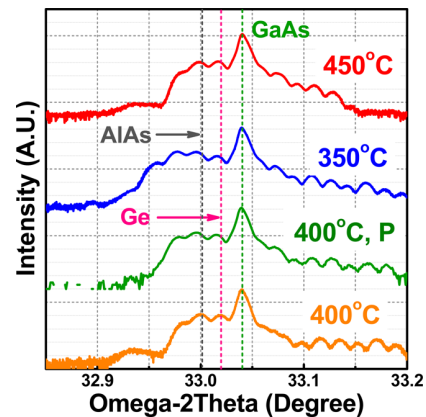


Figure 2. X-ray rocking curves for the 80 nm Ge layer grown on (100)/2° GaAs substrates at 350, 400, and 450 °C, respectively. The Pendellösung oscillations from these samples show the superior epitaxial crystalline quality. The X-ray curves were shifted vertically for clarity. The “P” represents the long growth pause prior to Ge layer growth.

The structure was further investigated by AFM to quantify the surface roughness and other growth-related defects. Figure 3 shows the AFM surface morphology of the epitaxial Ge layer grown at three growth temperatures on GaAs substrates using AlAs buffer layers without any long growth pause prior to the Ge layer growth. The AFM data reveals a root-mean-square (rms) roughness of ~ 1.8 – 2.5 nm over $20 \times 20 \mu\text{m}$ for the Ge, which is about 5 times higher than the Ge layer grown on (100)/6° GaAs substrate using MBE.¹⁵ The anticipated uniform and low surface roughness is an indication of high-quality two-dimensional epitaxy of Ge on AlAs/GaAs. The increase in surface roughness could be due to the growth of the AlAs layer on GaAs. The same growth rate (25 nm/h) and growth temperature (400 °C) exhibited a surface roughness of about 0.38 nm for the Ge grown on (100)/6° GaAs substrate.¹⁵ This is also consistent with reflection high energy electron diffraction (RHEED) observation during growth, which displayed a streakier (2×2) surface reconstruction pattern for Ge.¹⁵

During MBE growth, the active device layer is typically grown after a time pause of variable duration following growth of underlying layers. To understand the effect of a long growth pause prior to the growth of the Ge layer on the structural and electrical transport properties of the Ge layer, we kept the AlAs/GaAs sample under a vacuum of $\sim 10^{-9}$ Torr at 150 °C temperature inside the MBE chamber for about 12 h after the growth of AlAs, prior to the growth of the Ge layer. Figure 4 shows the AFM surface morphology of the epitaxial Ge layers on (100)/2° GaAs substrate grown at 400 °C with the growth pause. The measured surface roughness was ~ 2.21 nm, similar to the Ge layer grown at 400 °C without long growth pause (rms roughness of ~ 2.25 nm), as shown in Figure 3b. The surface roughness of Ge layers with and without the growth pause after the growth of AlAs layer, are almost identical. The X-ray analysis of this structure is shown in Figure 2. The electrical transport properties of these Ge layers would provide information whether the long growth pause prior to the Ge layer impacts the carrier mobility and ultimately the device properties. The insight will help device and process engineers by providing flexibility for designing Ge-based nanoscale transistor structures where a long growth pause in the process

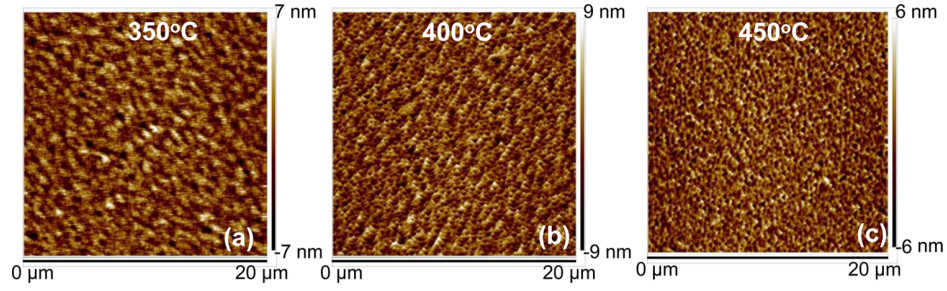


Figure 3. Surface morphology of the epitaxial Ge layers grown at three different growth temperatures on $(100)/2^\circ$ GaAs substrates. The measured surface roughness are in the range of 1.8–2.5 nm.

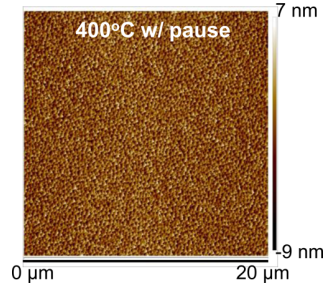


Figure 4. Surface morphology of the epitaxial Ge layer on $(100)/2^\circ$ GaAs substrate grown at 400 °C with 12 h growth pause after the AlAs layer growth. The measured surface roughness was 2.21 nm.

cannot be avoided. Table 1 shows the summary of the results obtained from these samples.

Table 1. Summary of Growth Parameter, Structural Analysis, And Electrical Transport Parameters of Ge Layers Grown on GaAs Substrates Presented in This Study

Ge growth temperature (°C)	Ge FWHM (arcsec)	RMS roughness (nm)	sheet carrier density (cm^{-2})	electron mobility ($\text{cm}^2/(\text{V s})$)
350 no pause	49.93	1.96	1.34×10^{14}	202.84
400 no pause	50.98	2.55	2.84×10^{13}	280.44
400 pause	49.10	2.21	5.86×10^{13}	252.05
450 no pause	47.23	1.78	2.07×10^{13}	202.75

The structural quality and the defect properties of the 80 nm Ge/170 nm AlAs/GaAs and 240 nm Ge/170 nm AlAs/2.2 μm

GaAs/Si structures were examined by cross-sectional TEM. Figure 5 shows a typical cross-sectional bright field TEM micrograph of the Ge/AlAs/GaAs and Ge/AlAs/GaAs/Si structure, respectively, showing the interfaces between Ge and AlAs as well as AlAs and GaAs. The layer structure shown in Figure 5 was grown at 400 °C without long growth pause. The image in Figure 5 shows a high contrast at each heterointerface and the Ge/AlAs/GaAs structure is lattice matched, as expected since the lattice constants of Ge, AlAs, and GaAs are almost identical (the lattice mismatch between Ge and GaAs is 0.07%). The lattice matched nature of the Ge layer revealed by the TEM micrograph is consistent with the results from the X-ray analysis above, demonstrating the significant achievement toward correlated synthesis–structure–property behavior. We also note that the AlAs layer will provide carrier confinement inside the Ge layer via the large band offsets of Ge/AlAs.⁸ A sufficiently high barrier for holes and electrons is indeed desired for carrier confinement. Further, the AlAs layer can serve as an etch stop layer when fabricating nanoscale Ge transistors.

Electrical Transport Properties. Effect of Growth Temperature and Growth Pause on Ge. To further investigate the quality of Ge layers grown at different temperatures, we measured the carrier mobility of the Ge films using electronic transport measurements in the van der Pauw configuration over a temperature range of 90–315 K. The transport measurements assess the quality and the carrier density in the semiconductor layers, with the mobility as an important figure-of-merit. Additionally, the mobility and the sheet carrier density obtained as a function of temperature are important design parameters for the next-generation nanoscale transistors. It is important that the carrier freeze-out be minimal at lower temperature and that transport in the layers be dominated by a single carrier.

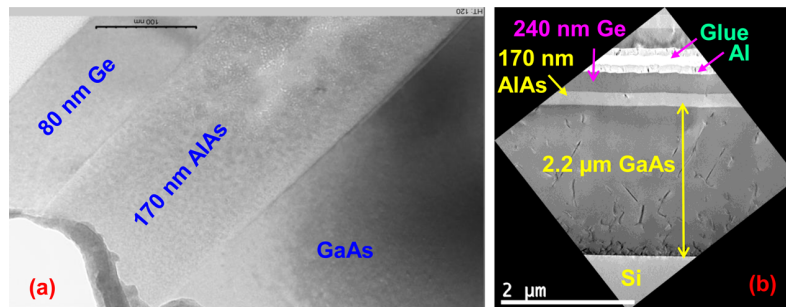


Figure 5. (a) Cross-sectional TEM micrograph of 80 nm Ge grown on GaAs substrate using a 170 nm AlAs buffer layer. The granular spots in some areas of AlAs layer are due to the damage during ion milling process. (b) Cross-sectional TEM micrograph of the Ge/AlAs/GaAs/Si structure. The TEM measurement was performed after depositing the aluminum metal.

Figure 6 shows the electron mobility and sheet carrier density as a function of temperature in Ge layers grown at different

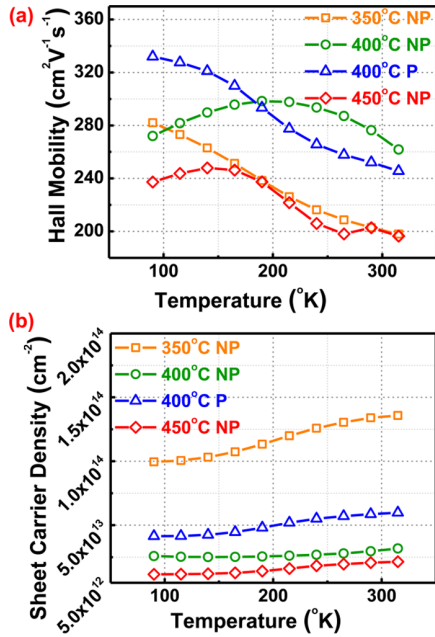


Figure 6. (a) Hall mobility and (b) sheet carrier density as a function of temperature in Ge layers grown at 350, 400, and 450 $^\circ\text{C}$, respectively. Ge layers were grown with without pause (NP) and with a long growth pause (P).

temperatures. The mobility at 290 K was $\sim 280 \text{ cm}^2/(\text{V s})$ for the sample grown at 400 $^\circ\text{C}$ compared to $\sim 200 \text{ cm}^2/(\text{V s})$ for samples grown at 350 and 450 $^\circ\text{C}$ without any long growth pause. However, at 290 K the sample grown at 400 $^\circ\text{C}$ with long growth pause exhibited a mobility value of about $255 \text{ cm}^2/(\text{V s})$. The sheet carrier density at 290 K is about $3 \times 10^{13} \text{ cm}^{-2}$ for a 400 $^\circ\text{C}$ growth temperature without growth pause. The lower mobilities at both 350 and 450 $^\circ\text{C}$ growth temperatures measured at 290 K rule out the possibility of growing high-quality Ge epitaxial layers on GaAs at these temperatures. However, these Ge layers exhibited similar X-ray FWHM and surface roughness as the sample grown at 400 $^\circ\text{C}$ (between the results from structural analysis and electrical transport properties, the electrical transport properties should be given preference). The complex dependences of mobility on temperature in Figure 6a are due to competing effects of phonon scattering, scattering on Coulombic impurities and dislocations, and interface scattering at the Ge/AlAs hetero-interface. It is interesting to compare the two samples grown at 400 $^\circ\text{C}$. Above 180 K, the mobility is higher for the sample grown without growth pause than for the sample grown with growth pause and slowly increases with decreasing temperature. Below 180 K, the mobility in the sample without growth pause decreases with decreasing temperature, whereas the mobility in the sample with growth pause keeps increasing. Of the competing scattering mechanisms, phonon scattering has the most pronounced temperature dependence. Phonon scattering increases with increasing temperature. Phonon-limited scattering will thus lead to a mobility decreasing with increasing temperature. A phonon-limited mobility denotes a good sample quality, since it implies other scattering mechanisms, originating in sample defects, do not dominate. The temperature

dependence of the mobility in the sample with growth pause indicates just such phonon-limited behavior, indicative of improved quality. The lower mobility from 180 to 315 K for the sample with growth pause (compared to without), could be due to the effect of the complex balance between phonon scattering, and the other scattering mechanisms, particularly interface scattering at Ge/AlAs hetero-interface. The sheet carrier densities do not change substantially over temperatures from 90 to 315 K for all samples. These results suggest an ideal growth temperature of 400 $^\circ\text{C}$ for the Ge layer, omitting the long growth pause. The sheet carrier density and the electron mobility of these samples measured at 290 K are also summarized in Table 1.

Effect of Forming Gas Annealing on Ge/AlAs/GaAs. To investigate the effect of forming gas annealing on the mobility and the sheet carrier density of a Ge layer grown at 400 $^\circ\text{C}$ without growth pause, we annealed a van der Pauw sample for different durations but at same annealing temperature of 350 $^\circ\text{C}$ under forming gas. After each measurement, the sample was annealed in forming gas (95% N_2 /5% H_2) for a prescribed time. Figure 7 shows the mobility and sheet carrier density of the Ge

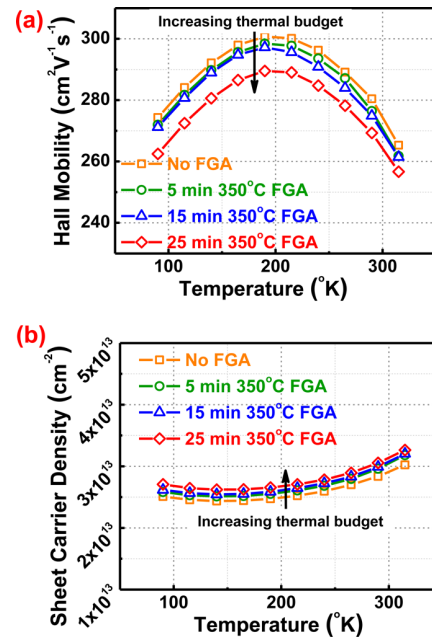


Figure 7. (a) Hall mobility and (b) sheet carrier density as a function of temperatures in Ge layers grown at 400 $^\circ\text{C}$ without long growth pause under different forming gas annealing (FGA) time at fixed annealing temperature of 350 $^\circ\text{C}$, respectively.

epilayer for annealing durations of 5, 15, 25 min, and without annealing. The 15 min annealing duration was a cumulative time of a 5 min annealing followed by a 10 min annealing. After 15 min annealing and measurement, the sample was further annealed for another 10 min (25 min total). In each case, the Hall mobility measurement was performed from 90 to 315 K. The shape of the mobility vs temperature graph is almost identical for different annealing durations at this fixed annealing temperature, while the mobility value decreases for longer annealing duration. The decrease is attributed to the effect of interface intermixing, creating defects within the Ge film. The sheet carrier density increases with annealing time, as shown in Figure 7b. Therefore, there exists a need to carefully balance the

annealing duration and ultimately the total thermal budget for the epitaxial Ge layer, such that device fabrication avoids mobility degradation. It is interesting to note that the repeated thermal annealing and temperature cycle measurements from 90 to 315 K (low-temperature thermal cycle or cryogenic stress) on the same Hall sample have minimal effect on the carrier mobility and density, indicating that the mobility of this structure is not affected by the cryogenic stress.

Effect of Forming Gas Annealing on Epitaxial Ge on Si Using AlAs/GaAs Buffer. Results on mobility measurements on the epitaxial Ge grown on Si using large bandgap AlAs/GaAs buffer layers were provided in earlier work.⁸ In order to understand the effect of annealing in forming gas on the mobility and carrier density, a van der Pauw sample was repeatedly annealed in forming gas and measured over the temperature range of 90–315 K, as described above. One purpose of these measurements is to understand the effect of hydrogen on the passivation of the shallow donors and the concomitant effect on carrier density. These experiments also allow us to ascertain the reliability of repeated mobility measurements data after cryogenic stressing on this sample. During the repeated measurements, the sample might generate a crack due to the thermal mismatch of the Ge/III–V layer and the Si substrate by the differences in thermal expansion in the aforementioned structure. Figure 8 shows the mobility and the

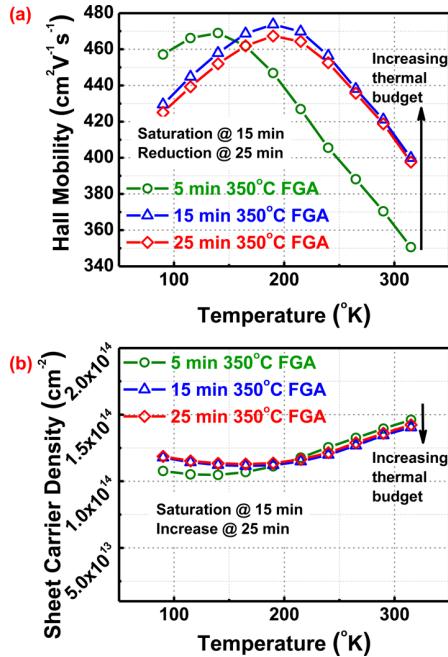


Figure 8. (a) Mobility and (b) sheet carrier density as a function of temperature in the Ge layer grown at 400 $^{\circ}\text{C}$ under different forming gas annealing FGA time, respectively, on Si using a composite AlAs/GaAs buffer layer.

carrier density as a function of measurement temperature and forming gas annealing conditions. One can find from Figure 8a that the mobility value increased from 370 to 420 $\text{cm}^2/(\text{V s})$ at 290 K when the sample was annealed for an additional 10 min. This increase in mobility is attributed to the reduction of the point defects by the thermal annealing. However, the further forming gas annealing by an additional 10 min reduces the mobility, similar to Figure 7a. Thus, a crucial total thermal

budget exists for the transport properties of Ge layer either grown on GaAs or on Si substrates. The carrier density is almost constant over temperature for different annealing temperatures, suggesting that the carriers are confined to the Ge layer, with the AlAs layer acting as a parallel conduction blocking barrier over this temperature range. Furthermore, comparing the electron mobility of Ge layer grown on Si as well as on GaAs, one can find that the electron mobility is higher on Si substrate than on GaAs substrate. One might expect better crystalline quality of Ge on GaAs than on Si and hence higher electron mobility. However, the mobility may not correlate one-on-one with the crystal quality, and optimization of mobility is the ultimate aim. Depending on the scattering mechanism induced by crystal defects, the mobility may not severely be affected. For instance, small-angle scattering mechanisms, as due to extended Coulombic scattering potentials, will not much affect mobility since small-angle scattering is ineffective at diffusing forward momentum. We presume that the lower crystal quality obtained on Si still affords a higher mobility since the scattering mechanisms induced by the lower crystal quality can be ineffective at reducing mobility, whereas effective scattering mechanisms have been reduced.

Magnetotransport Measurement of Epitaxial Ge on Si using AlAs/GaAs Buffer. To confirm the single carrier conduction, we performed magnetotransport measurements at 390 mK and over ± 9 T magnetic field applied normally to a sample in the van der Pauw geometry. Figure 9a shows the antisymmetric component of the Hall resistance (off-diagonal component R_{xy}) up to ± 9 T magnetic field with the different configurations of current and voltage contacts as depicted schematically in the insets for the van der Pauw geometry. The Hall resistance R_{xy} is linear up to high B in both the field directions and shows minimal intermixing with the symmetric component of Hall resistance R_{xx} . The linearity in B indicates single carrier conduction in the Ge layer. According to the linear slope, the Hall mobility measured at this temperature yielded a carrier density of $N_B = 1.42 \times 10^{14} \text{ cm}^{-2}$ and an electron mobility of $\mu_B = 392 \text{ cm}^2/(\text{V s})$, respectively, which is in agreement with the measurements depicted in Figure 8a,b. With a different contact configuration as depicted in Figure 9a, also yielding a linear slope, very nearly the same carrier density is obtained. Assuming one dominant carrier for conduction, at 390 mK it is found that the sheet resistance is $112.72 \Omega/\square$, the sheet carrier density $1.42 \times 10^{14} \text{ cm}^{-2}$, and the mobility $392 \text{ cm}^2/(\text{V s})$ for the epitaxial Ge on Si using AlAs/GaAs buffer.

Magnetotransport measurements at low temperatures (below ~ 1 K, here at 390 mK) reveal quantum corrections to the conductivity in materials with moderate disorder, called weak-localization and antilocalization.^{16–19} The quantum correction of weak-localization is observed in the measurements depicted in Figure 9b,c, as discussed below. Weak localization is a manifestation of the near-absence of spin–orbit interaction, in contrast to antilocalization which is a manifestation of the presence of spin–orbit interaction.^{18–22} The quantum corrections result from quantum interference of time-reversed closed-loop scattering trajectories. A negative magnetoresistance at low magnetic fields is a hallmark of weak-localization, whereas a positive magnetoresistance is a hallmark of antilocalization.²⁰ An initial decrease in resistance with increasing magnetic field (negative magnetoresistance, weak-localization at low fields) is indeed observed in Figure 9b,c. The existence of weak-localization, and not antilocalization, points

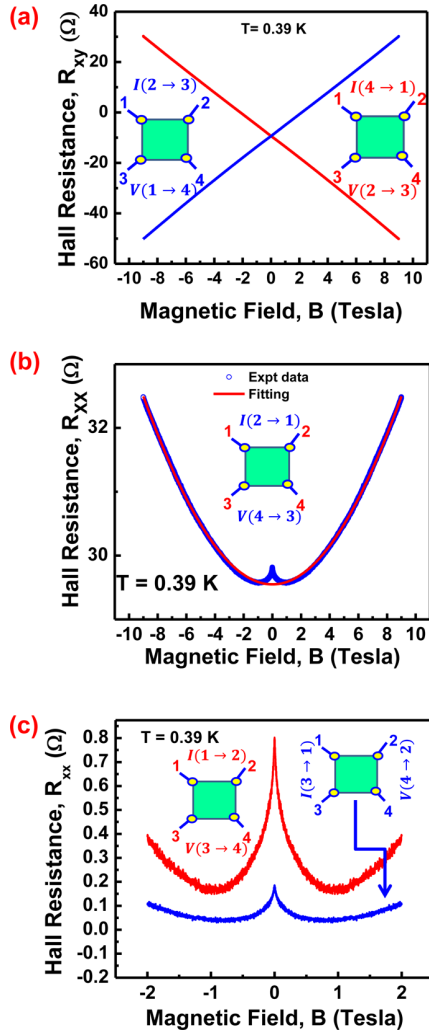


Figure 9. (a) Antisymmetric component of the Hall resistance, R_{XY} as a function of magnetic field over $\pm 9T$, with the very linear dependence on magnetic field demonstrating single carrier behavior. (b) Symmetric component of the Hall resistance, R_{XX} as a function of magnetic field over $\pm 9T$. (c) High-resolution traces, with different resistance offsets subtracted, emphasizing the weak-localization behavior at low magnetic fields.

to the fact that the carriers responsible for transport experience a near absence of spin-orbit interaction. As explained below, in the Ge/ALAs heterostructure this observation indicates that the carriers responsible for transport are electrons confined to the Ge layer, and excludes transport contributions due to carriers in the ALAs layer. Figure 9b,c show the symmetric component of the Hall resistance (diagonal component R_{xx}) up to ± 9 T magnetic field with the different configurations of current and voltage contacts as depicted schematically in the insets for the van der Pauw geometry. Figure 9b shows the weak-localization negative magnetoresistance at low field (below $\sim 1T$). Figure 9c shows high-resolution traces at low fields (resistance offsets were subtracted during the measurement to obtain higher measurement resolutions). Figure 9c clearly shows the existence of the negative magnetoresistance characteristic of weak-localization. As mentioned above, the carriers responsible for transport thus must experience negligible spin-orbit interaction. Spin-orbit interaction occurs due to a broken

spatial inversion symmetry,²³ either in the bulk crystal (Dresselhaus effect^{24,25}) or due to heterostructural asymmetry (Rashba effect^{26,27}). The ALAs, as a III-V compound semiconductor, has a lack of inversion symmetry in the bulk crystal and thus carriers in ALAs necessarily experience spin-orbit interaction, while in contrast, specifically electrons in Ge experience only negligible spin-orbit interaction.²³⁻²⁵ Thus, the transport in the Ge/ALAs heterostructure must occur by electrons only in the Ge layer. This confirms the single carrier conduction and pinpoints the Ge layer as the electronically active layer. The single carrier conduction and the detailed magnetotransport properties of the epitaxial Ge demonstrated above illustrate the strong potential for low-power transistors as well as optoelectronic devices.

CONCLUSIONS

The growth, structural, and magnetotransport properties of epitaxial Ge/ALAs heterostructures with different growth conditions and substrate architectures have been studied under ± 9 T magnetic field and at 390 mK temperature. Systematic mobility measurements of Ge epilayer on GaAs substrates with growth temperatures from 350 to 450 °C demonstrated the highest electron mobility at 400 °C without long growth pause prior to Ge deposition, which is corroborated by structural and morphological studies. Our results on Si substrate using a composite ALAs/GaAs buffer architecture at 400 °C Ge growth temperature demonstrates that the Ge/ALAs shows single carrier transport with the charge solely confined to the Ge layer. The prominent negative magnetoresistance at 390 mK temperature is indicative of the weak-localization effect in this Ge/ALAs heterostructure and points to the near absence spin-orbit interaction, a first demonstration in this heterostructure indicating that carriers responsible for transport must be electrons confined to the Ge layer. Hence, epitaxial Ge grown on Si using an ALAs/GaAs buffer architecture shows a great promise for next-generation low-power and high-performance field effect transistor applications.

MATERIALS AND METHODS

Material Synthesis. The undoped epitaxial 80 nm-240 nm thick Ge layers were grown using an in situ growth process on epi-ready semi-insulating (100)/2° GaAs and (100)/6° offcut Si substrates using separate solid source molecular beam epitaxy growth chambers for the Ge and III-V materials, connected via an ultrahigh vacuum transfer chamber. The growth temperature and growth rate of epitaxial Ge were in the range of 350–450 °C and 0.1 Å/s, respectively. The details of the growth procedure are reported elsewhere.^{8,15}

Materials Characterization. To determine the structural quality and the relaxation state of epitaxial Ge layers, we recorded high-resolution triple axis X-ray rocking curves. Cross-sectional high-resolution transmission electron microscopy (HR-TEM) was used to characterize the interface between the Ge and ALAs and GaAs substrate. The HR-TEM imaging was performed on a JEOL 2100 transmission electron microscope. For this purpose, the electron transparent foil of thin film cross-section of Ge/ALAs/GaAs was prepared by a standard polishing technique, that is, mechanical grinding, dimpling, and Ar⁺ ion beam milling.

Carrier Transport Measurement. Au/Ti (600 Å/200 Å) ohmic contacts required for the Hall mobility measurements were made on Ge/ALAs/GaAs and Ge/ALAs/GaAs/Si in a Kurt J. Lesker PVD 250 physical vapor deposition system. The four corner contacts were defined using positive photoresist and prebaked at ~ 85 °C prior to the deposition of Au and Ti metals. The deposited contacts were annealed at 350 °C for 5, 15, and 25 min under a mixture of N₂/H₂ (95:5 v/v).

The carrier density and Hall mobility were measured as a function of temperature from 90 to 315 K with a fixed magnetic field of 0.5T using an Ecopia HMSS000 Hall measurement system. The magnetotransport measurements at 390 mK, and high magnetic fields were performed in a ^3He cryostat, with the sample submerged in liquid ^3He . The ^3He system is equipped with a superconducting magnet allowing the magnetic field to be varied over 9 T in both polarities normal to the sample surface. The weak localization data was obtained in the same system using a magnet power supply capable of slow sweeps with subgauss resolution.

AUTHOR INFORMATION

Corresponding Author

*Tel: (540) 231-6663. Fax: (540) 231-3362. E-mail: mantu.hudait@vt.edu.

Notes

The authors declare no competing financial interest.

ACKNOWLEDGMENTS

This work was supported in part by Intel Corporation. M.C. acknowledges the financial support from NSF under grant number ECCS-1348653. P.G. acknowledges support from an NSF Graduate Research Fellowship. J.J.H. and Y.X. acknowledge support by the U.S. Department of Energy, Office of Basic Energy Sciences, Division of Materials Sciences and Engineering under award DOE DE-FG02-08ER46532. Authors also acknowledge NCFI-Institute for Critical Technology and Applied Science and Virginia Tech Nanofabrication facilities for materials characterization and contact formation, respectively.

REFERENCES

- (1) Krishnamohan, T.; Krivokapic, Z.; Uchida, K.; Nishi, Y.; Saraswat, K. C. High-Mobility Ultrathin Strained Ge MOSFETs on Bulk and SOI With Low Band-to-Band Tunneling Leakage: Experiments. *IEEE Trans. Electron Devices* **2006**, *53*, 990–999.
- (2) Krishnamohan, T.; Kim, D.; Nguyen, C. D.; Jungemann, C.; Nishi, Y.; Saraswat, K. C. High-Mobility Low Band-to-Band Tunneling Strained-Germanium Double-gate Heterostructure FETs: Simulations. *IEEE Trans. Electron Devices* **2006**, *53*, 1000–1009.
- (3) Ho, B.; Nuo, X.; Tsu-Jae King, L. pMOSFET Performance Enhancement With Strained $\text{Si}_{1-x}\text{Ge}_x$ Channels. *IEEE Trans. Electron Devices* **2012**, *59*, 1468–1474.
- (4) Chleirigh, C. N.; Theodore, N. D.; Fukuyama, H.; Mure, S.; Ehrke, H.-U.; Domenicucci, A.; Hoyt, J. L. Thickness Dependence of Hole Mobility in Ultrathin SiGe-channel p-MOSFETs. *IEEE Trans. Electron Devices* **2008**, *55*, 2687–2694.
- (5) Hutin, L.; Le Royer, C.; Damlencourt, J.-F.; Hartmann, J.-M.; Grampeix, H.; Mazzocchi, V.; Tabone, C.; Previtali, B.; Pouydebasque, A.; Vinet, M. GeOI pMOSFETs Scaled Down to 30-nm Gate Length With Record Off-state Current. *IEEE Electron Device Lett.* **2010**, *31*, 234–236.
- (6) Pillarisetty, R.; Chu-Kung, B.; Corcoran, S.; Dewey, G.; Kavalieros, J.; Kennel, H.; Kotlyar, R.; Le, V.; Lionberger, D.; Metz, M.; et al. High Mobility Strained Germanium Quantum Well Field Effect Transistor as the p-Channel Device Option for Low Power ($V_{cc} = 0.5\text{V}$) III-V CMOS Architecture. *Technical Digest International Electron Devices Meeting-IEDM* **2010**, 6.7.1–6.7. 4.
- (7) Zhang, R.; Yu, X.; Takenaka, M.; Takagi, S. Impact of Channel Orientation on Electrical Properties of Ge p- and n-MOSFETs With 1-nm EOT $\text{Al}_2\text{O}_3/\text{GeO}_2/\text{Ge}$ Gate-Stacks Fabricated by Plasma Post oxidation. *IEEE Trans. Electron Devices* **2014**, *61*, 3668–3675.
- (8) Hudait, M. K.; Clavel, M.; Goley, P.; Jain, N.; Zhu, Y. Heterogeneous Integration of Epitaxial Ge on Si using ALAs/GaAs Buffer Architecture: Suitability for Low-power Fin Field-Effect Transistors. *Sci. Rep.* **2014**, *4*, 6964–6969.

- (9) Nguyen, P. D.; Clavel, M.; Goley, P.; Liu, J.-S.; Allen, N.; Guido, L. J.; Hudait, M. K. Heteroepitaxial Ge MOS Devices on Si Using Composite ALAs/GaAs Buffer. *IEEE J. Electron Devices Soc.* **2015**, *3*, 341–348.

- (10) Hudait, M. K. Heterogeneously Integrated III-V on Silicon for Future Nanoelectronics. *ECS Trans.* **2012**, *45*, 581–594.

- (11) Hudait, M. K.; Dewey, G.; Datta, S.; Fastenau, J. M.; Kavalieros, J.; Liu, W. K.; Lubyshev, D.; Pillarisetty, R.; Rachmady, W.; Radosavljevic, M.; Rakshit, T.; Chau, R. Heterogeneous Integration of Enhancement Mode $\text{In}_{0.7}\text{Ga}_{0.3}\text{As}$ Quantum Well Transistor on Silicon Substrate Using Thin ($2\mu\text{m}$) Composite Buffer Architecture for High-speed and Low-voltage (0.5V) Logic Applications. *IEEE International Electron Devices Meeting (IEDM) Technical Digest* **2007**, 625–628.

- (12) Lubyshev, D.; Fastenau, J. M.; Wu, Y.; Liu, W. K.; Bulsara, M. T.; Fitzgerald, E. A.; Hoke, W. E. Molecular Beam Epitaxy Growth of Metamorphic High Electron Mobility Transistors and Metamorphic Heterojunction Bipolar Transistors on Ge and Ge-on-Insulator/Si Substrates. *J. Vac. Sci. Technol. B* **2008**, *26*, 1115–1119.

- (13) Hudait, M. K.; Lin, Y.; Sinha, P. M.; Lindemuth, J. R.; Ringel, S. A. Carrier Compensation and Scattering Mechanisms in Si-doped $\text{InAs}_x\text{P}_{1-y}$ Layers Grown on InP Substrates Using Intermediate $\text{InAs}_x\text{P}_{1-y}$ step-Graded buffers. *J. Appl. Phys.* **2006**, *100*, 063705–1–9.

- (14) Lindemuth, J. R. Parallel Conduction in Semiconductors. *III-Vs Review* **2006**, *19*, 28–32.

- (15) Hudait, M. K.; Zhu, Y.; Jain, N.; Hunter, J. L., Jr. Structural, Morphological, and Band Alignment Properties of GaAs/Ge/GaAs Heterostructures on (100), (110) and (111)A GaAs Substrates. *J. Vac. Sci. Technol. B* **2013**, *31*, 011206–1–14.

- (16) Bergmann, G. Weak Localization and its Applications as an Experimental Tool. *Int. J. Mod. Phys. B* **2010**, *24*, 2015–2052.

- (17) Bergmann, G. Weak Localization in Thin Films, a Time-of-flight Experiment With Conduction Electrons. *Phys. Rep.* **1984**, *107*, 1–58.

- (18) Kallagher, R. L.; Heremans, J. J. Spin and Phase Coherence Measured by Antilocalization in n-InSb Thin Films. *Phys. Rev. B: Condens. Matter Mater. Phys.* **2009**, *79*, 075322.

- (19) Kallagher, R. L.; Heremans, J. J.; Goel, N.; Chung, S. J.; Santos, M. B. Spin-orbit Interaction Determined by Antilocalization in an InSb Quantum Well. *Phys. Rev. B: Condens. Matter Mater. Phys.* **2010**, *81*, 075303.

- (20) Bergmann, G. Weak Anti-localization - An Experimental Proof for the Destructive Interference of Rotated Spin 1/2. *Solid State Commun.* **1982**, *42*, 815–817.

- (21) Iordanskii, S. V.; Lyanda-Geller, Y. B.; Pikus, G. E. Weak Localization in Quantum Wells With Spin-orbit Interaction. *JETP Lett.* **1994**, *60*, 206–211.

- (22) McPhail, S.; Yasin, C. E.; Hamilton, A. R.; Simmons, M. Y.; Linfield, E. H.; Pepper, M.; Ritchie, D. A. Weak Localization in High-quality Two-dimensional Systems. *Phys. Rev. B: Condens. Matter Mater. Phys.* **2004**, *70*, 245311.

- (23) Winkler, R. Spin-orbit Coupling Effects in Two-dimensional Electron and Hole Systems. *Springer Tracts in Modern Physics*; Springer-Verlag: Berlin, Heidelberg, 2003.

- (24) Dresselhaus, G. F. Spin-orbit Coupling Effects in Zinc Blende Structures. *Phys. Rev.* **1955**, *100*, 580–586.

- (25) Faniel, S.; Matsuura, T.; Mineshige, S.; Sekine, Y.; Koga, T. Determination of Spin-Orbit Coefficients in Semiconductor Quantum Wells. *Phys. Rev. B: Condens. Matter Mater. Phys.* **2011**, *83*, 115309.

- (26) Bychkov, Y. A.; Rashba, E. I. Oscillatory Effects and the Magnetic Susceptibility of Carriers in Inversion Layers. *J. Phys. C: Solid State Phys.* **1984**, *17*, 6039–6045.

- (27) Pfeiffer, P.; Zawadzki, W. Spin Splitting of Conduction Subbands in III-V Heterostructures Due to Inversion Asymmetry. *Phys. Rev. B: Condens. Matter Mater. Phys.* **1999**, *59*, R5312–R5315.

This paper was previously published as: M. K. Hudait, M. Clavel, P. S. Goley, Yuantao Xie and J. J. Heremans, “Magnetotransport properties of epitaxial Ge/AlAs heterostructures integrated on GaAs and silicon”, ACS Applied Materials & Interfaces 7, 22315 (2015).

Chapter 9

Conclusions

Quantum interference effects in mesoscopic structures are experimentally studied. The results obtained are interpreted in the context of existing theories, supported by numerical models which are modified or augmented to better reflect the observations. The pursuit of quantum phenomena in mesoscopic structures stems from the desire to understand the mechanisms that influence the phase coherence length of electrons in materials system of interest to current and future quantum technologies and electronic devices.

Mesoscopic structures, quantum stadia, quantum wires and side-gated rings, were fabricated on InGaAs/InAlAs heterostructures by photolithography and electron-beam lithography. Quantum transport was investigated at low temperatures to access the quantum interference phenomena of interest. In quantum stadia, the circular arenas were connected to their classical environment through side wires, and the coupling probed through the quantum interference effect of universal conductance fluctuations. The universal conductance fluctuations were used to extract electron phase coherence lengths, and were found to be dependent on both the temperature of the measurement and the geometry of the mesoscopic stadia. The geometrical dependence was related to side-wire width-to-length ratio, and explained by the competing effects of decoherence induced by coupling to the classical environment and Nyquist decoherence mechanism in ergodic wires. Phase coherence lengths decreased with increase of temperature, consistent with expectations.

In quantum wires, phase coherence lengths were measured by the quantum interference phenomenon of weak antilocalization. The temperature dependence of the phase coherence length was dominated by Nyquist scattering; phase coherence lengths decreased with increasing temperature. Phase coherence lengths increased as wire lengths increased, attributed to the reduced influence of environmental coupling decoherence dominant at wires' ends. In longer wires, the environmental coupling decoherence were essentially averaged out, and long phase coherence lengths were observed as a function of wire length at a given temperature.

Quantum interference in side-gated rings was probed by the quantum-mechanical Aharonov-

Bohm oscillations of the magnetic flux through the ring. The amplitude of the oscillations depends sensitively on decoherence effects. The different paths, right left, taken by electrons traversing the ring result in interference. This interference is further influenced by the application of an in-plane electric field via the side gates of the ring, which results in breaking the two-dimensional parity symmetry of the ring interferometer, leading to a decrease in the amplitude of the Aharonov-Bohm oscillations.

Magnetotransport measurements at low temperatures were performed to investigate quantum phenomena in the following materials: bismuth iridate thin films, and Ge/AlAs heterostructures on GaAs or Si substrates. In the bismuth iridate system, logarithmic temperature dependence of the resistivity was observed, as well as the presence of multiple carriers. The presence of spin-orbit coupling in these films was investigated by antilocalization measurements. In the Ge/AlAs heterostructures system, linear Hall resistivity indicated single carrier transport in Ge/AlAs heterostructures, while weak localization measurements around zero magnetic field revealed almost no spin-orbit interaction for the carriers in the Ge heterostructures, which implied the single carrier was essentially located at Ge layer only. The interesting magnetotransport properties of these two materials show potential promise for applications in quantum technologies and devices.

In summary, decoherence effects and mechanisms were studied in different mesoscopic structures, as such investigations address fundamental aspects future quantum devices designs.